Non-Cartesian Parallel Image Reconstruction for Functional MRI

by

Yoon Chung Kim

A dissertation submitted in partial fulfillment
of the requirements for the degree of
Doctor of Philosophy
(Biomedical Engineering)
in The University of Michigan
2011

Doctoral Committee:

Professor Douglas C. Noll, Chair
Professor Thomas L. Chenevert
Professor Jeffrey A. Fessler
Research Associate Professor Luis Hernandez
Research Investigator Jon-Fredrik Nielsen

To my parents

ACKNOWLEDGEMENTS

First and foremost, I would like to thank God for allowing me to experience life in Ann Arbor at University of Michigan, and to meet wonderful people. Especially, I would like to thank Dr. Douglas C. Noll, my research advisor, who has guided me with patience, and who has greatly influenced my life. He is a great scholar who has great passion for research, and also a wonderful person who really takes care of his students. Dr. Jeffrey A. Fessler, whom I also would like to give my thanks to, has been a great research advisor. I really thank him for providing me with great tools and lots of insights for image reconstruction algorithms that have vastly been used in my research. I also would like to thank other committee members, Dr. Thomas L. Chenevert, Dr. Luis Hernandez and Dr. Jon-Fredrik Nielsen, who has been very supportive and has been guiding me throughout the process with kindness and patience.

I also would like to thank Mimi Adams, Pastor Tom and Debi Humphreys who has been my mentors in my journey here in Ann Arbor. Mimi has tutored my writing skill for many years. After years of work and learning from Mimi, my writing skill in English has improved a lot and I now feel much more comforts and confidence in writing. I owe so much to her and I can never thank her enough for that. She is not only a great expertise in her area of tutoring writing skill but also a wonderful mentor and encourager and I also thank her for that. Pastor Tom and Debi Humphreys, I cannot thank them enough and I really owe a lot to them. They were always there for me in the midst of difficult times.

They guided me with great love, wisdom and patience. I could not have survived difficult times without their help.

I have enjoyed my life at the fMRI lab thanks to Sangwoo Lee, Chun-yu Yip, Gregory Lee, Kiran Pandey, Alberto Vazquez, and Valur Olafsson, who are my former lab mates, and Daehyun Yoon, Hesam Jahanian, Yash Shah, Vivek Bhatia, Alan Chu, Angela Harrivel, as well as Scott Peltier, Keith Newnham, Chuck Nicholas, and Ruth Halsey whom I have enjoyed being around and given me great insights for research and life.

I also thank Ann Arbor Hope Church members as well as K-BME members. Studying abroad didn't seem to be an easy task for me but I was able to get through it because of them. I especially thank my close friends, Miyeon, Donghee, Taegyun, Eunkyung, Jina, and Byungwook. Just being around them has been a great pleasure and encouragement for me. They are not just friends but also like a family to me.

I thank my parents and my sister in Korea, whom I love so much. Even though they are not here, they have been praying for me and have been a great support for me.

It was quite a long journey but the lessons that I learned from this journey is priceless which I would like to carry on throughout my life.

TABLE OF CONTENTS

LIST OF FIGURES

LIST OF TABLES

CHAPTER 1. Introduction

1.1 Functional MRI

Functional MRI (fMRI) is a widely preferred imaging modality that highly depends on the ability to detect the regional changes in the brain according to a task activation. Among fMRI techniques proposed to date, blood oxygenation level dependent (BOLD) technique is primarily used, because it is easy to implement and has high functional activation contrast. The BOLD fMRI was first described in 1990 by Ogawa et al. [1]. It is an indirect measurement of brain activity where the imaging contrast in local draining venules and veins is caused by changes in the ratio of oxygenated (diamagnetic) to deoxygenated (paramagnetic) hemoglobin (Hb), which accompanies neuronal activity [2]. This change in blood oxygenation affects the MR decay parameter, T2*, which, in turn, affects T2*-weighted BOLD signal, as shown in Figure 1-1.

However, even though BOLD fMRI has been widely used, there are various factors limiting the current fMRI approach such as, noise from measurement or systematic errors. Its spatial or temporal resolution is also limited by relatively long TE, to have optimal sensitivity for BOLD signal change, and it also suffers severely from susceptibility artifacts, which come from the difference between magnetic susceptibilities of tissue and of air [3]. The susceptibility effect becomes even more pronounced at higher static

magnetic (B0) field, significantly degrading the performance of current fMRI.

Thus, the major limitations of the current fMRI technique, which restrict the role in brain imaging are limited spatial resolution, limited temporal resolution, and image distortions and artifacts.

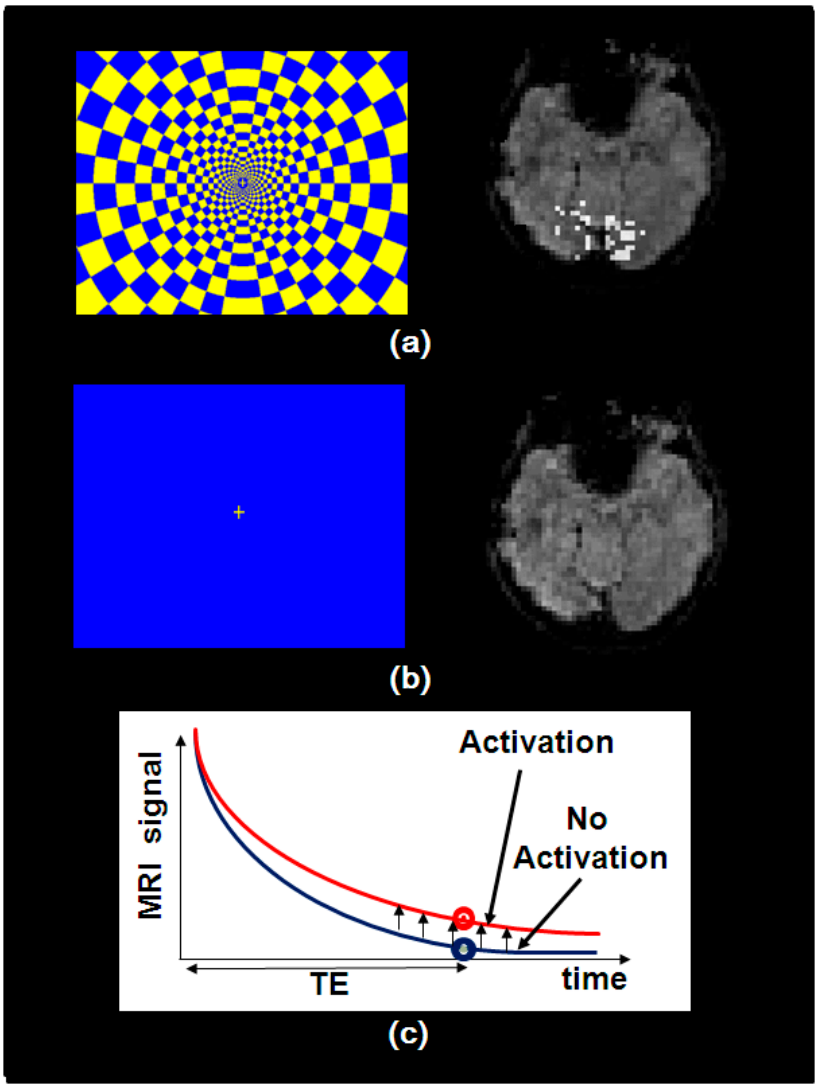

Figure 1-1 Example of BOLD fMRI. (a-b) Left column shows an example of visual activation (a) ON and (b) OFF mode and right column shows its related brain activation at visual cortex area. Activated areas in the brain (above threshold level) are marked as white dots in (a). During the task activation, the increase of HbO_2 concentration results in the increase of T2* parameter which then increases MRI signal intensity which is shown in (c).

These limitations make it difficult to specify the brain activation region accurately, and make it difficult to study the details of the dynamic behavior and interactions of each brain region, which could eventually lead to inaccurate or inadvertent misinterpretation of the brain activity. These problems can be at least partially solved by parallel imaging methods that use multiple receiver coil arrays and undersampling of k-space data.

1.2 Parallel Imaging

Our overall research goal, ideally, is to find techniques to improve fMRI performance by providing better spatial and temporal resolution and image quality. We can achieve those goals in fMRI techniques by applying parallel imaging techniques.

Parallel imaging (PI), which uses an array of multiple coils, was originally developed to improve the scan speed by reducing the number of phase encode (PE) lines. The effect of magnetic susceptibility artifact, which is one of the main factors causing distortions and signal loss in the resulting images, can be significantly suppressed by the use of parallel imaging techniques. [4-6]

Parallel imaging also improves spatial and temporal resolutions by reducing a time-consuming spatial encoding step by undersampling, and uses additional information, such as spatial sensitivity profiles, to reconstruct unaliased images. In addition to reducing scan time, researchers also discovered that parallel imaging can overcome the limitation of gradient performance and reduces the acoustic noise [5,6].

The main drawback of PI technique is low SNR due to undersampling of k-space data which will be addressed in detail in later section. However, using an array coil

instead of head coil can improve SNR. Moreover, the image distortion due to the susceptibility artifact is often more problematic than the SNR penalty, especially when using a small reduction factor, i.e., acceleration factor which is the rate of skipped k-space samples. Although PI technique was originally designed for cardiac imaging, it is suitable for functional brain imaging, since fMRI also acquires time series data and suffers from susceptibility artifacts.

Various PI methods have been proposed, and they can be basically divided into three categories: image-based, k-space based and hybrid techniques. The most well known image domain based methods are SENSE [7] and PILS [8], whereas k-space based methods are SMASH [9], Auto-SMASH [10], VD-AUTO-SMASH [11] and GRAPPA [12]. On the other hand, SPACE-RIP [13] is a representative hybrid technique in which the reconstruction process is done partly in image and partly in k-space domain. SENSE [7] and GRAPPA [12] are the main focus of our study, because they are most widely used and are commercially available for Cartesian sampled acquisitions.

1.2.1 SENSE

SENSitivity Encoding (SENSE) was first introduced by Pruessmann et al. in 1999 [7]. It is an image-domain approach in which reduced-FOV data are acquired and sensitivity maps are employed to reconstruct a full-FOV image through a process of ‘unfolding’ the ‘folded’ image. In other words, the reduced Fourier encoding results in folded image as shown in Figure 1-2 and the aliasing artifacts are produced. Then, ‘unfolding’ of this folded image produces an unaliased image. This is done by using an unfolding matrix (U) that is calculated from the noise covariance matrix (Ψ) and

sensitivity map matrix (S):

$$U = (S^H \Psi^{-1} S)^{-1} S^H \Psi^{-1} \tag{1.1}$$

Multiplying the unfolding matrix by a vector containing 'folded' samples from all coils at a single spatial location in an aliased image produces a vector of 'unfolded' samples from several spatial locations. By performing this multiplication for all voxels in the aliased image, an 'unfolded' image can be obtained. In SENSE, the unaliasing process and the multi-coil image combination are combined in this one unfolding process.

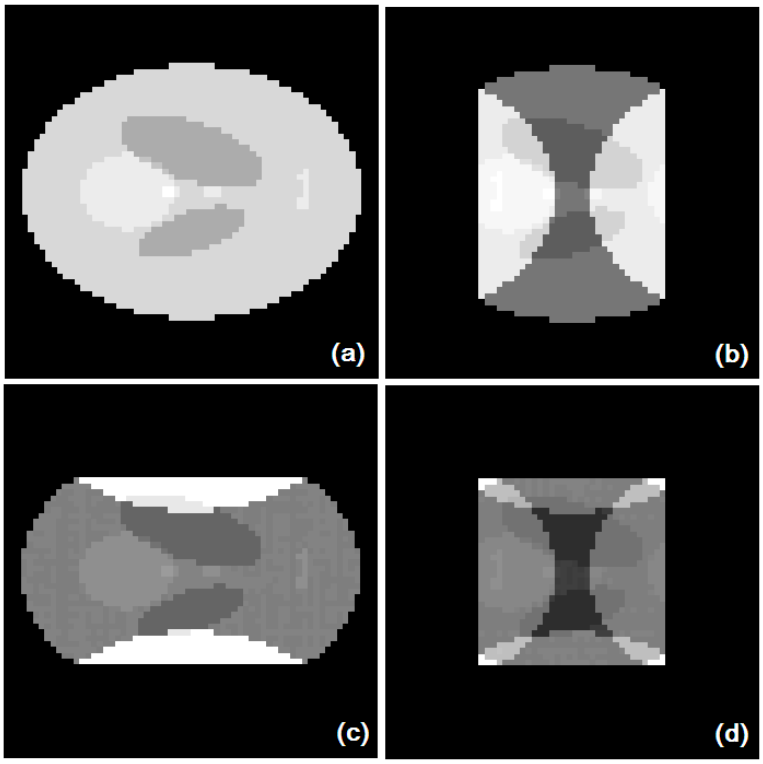

Figure 1-2 (a) The original image and (b-d) 'folded' images for Cartesian sampling. (a) A full FOV image is reduced to (b-d) reduced FOV images and aliasing patterns were produced. The reduced sampling rate is 2 at (b) FE, (c) PE and (d) both FE and PE directions. For (d), the actual resulting reduction factor is 4 (=2 ×2), that is, four pixels were 'folded'.

Determining the sensitivity maps is an important issue for the SENSE method, since it is used in the "unfolding" process in SENSE. The sensitivity maps are estimated either by prescanning or by self-calibration [7,14,15]. One prescanning approach for determining the sensitivity maps is to divide each fully sampled coil image by the body coil image, followed by a denoising process[7]. This approach produces accurate image reconstructions when there is no patient motion. However, in fMRI, patient motion is common due to long scan times, and self-calibrated methods are preferable. Furthermore, to skip the acquisition of a body coil image in a prescanning step, a self-calibrating approach can be used. The self-calibrating approach divides each coil image by the reference image generated by using low resolution map from center k-space data or some combination of each coil image, such as sum of squares and geometric mean approaches when fully-sampled surface coil images are attainable. The resulting sensitivity maps are usually smoothed to extend them beyond the boundaries of the object.

1.2.2 GRAPPA

GeneRalized Autocalibrating Partially Parallel Acquisitions (GRAPPA) [12] is a k-space based approach in which unsampled data is estimated using information from additionally acquired samples in the center k-space, the so-called Auto-Calibration Signal (ACS) lines. GRAPPA evolved from two different techniques, variable density (VD-) AUTO-SMASH [9-11] and parallel imaging with localized sensitivities (PILS) [8]. VD-AUTO-SMASH is a generalized version of SMASH where, rather than using a single k-space line, it uses blocks of k-space lines for calculating missing k-space lines that

improves accuracy in modeling coil sensitivity pattern with sharper edges. GRAPPA also adopts this estimation approach from block k-space line. However, it is also considered an "extended" implementation of a VD-AUTO-SMASH technique in that, instead of fitting acquired data into one composite signal, GRAPPA acquires coefficients by fitting each component coil signal to the composite signals that are composed of ACS lines from each coil as shown in Figure 1-3, thus yielding multiple composite signals. This concept was adopted from the PILS technique of separating the unaliasing from the image combination process. After producing composite signals, the combination process is being done either by nonlinear process such as simple sum-of-squares approach [16] or other carefully designed adaptive approaches [17,18].

In GRAPPA, the fitting process of the jth coil data at (k_y-$m\Delta k_y$)-th line from the acquired data is represented by:

$$S_j(k_y - m\Delta k_y) = \sum_{l=1}^{L} \sum_{b=0}^{n_b-1} n(j,b,l,m) S_l(k_y - bR\Delta k_y) \tag{1.2}$$

where L is the number of receive coils in the array, R is the reduction factor, and n(j,b,l,m) are the GRAPPA coefficients from l-th coil, b-th neighbor in phase-encoding direction of k-space. We use the sum of squares to combine composite images from each coil, but other optimal combination techniques can also be used [18].

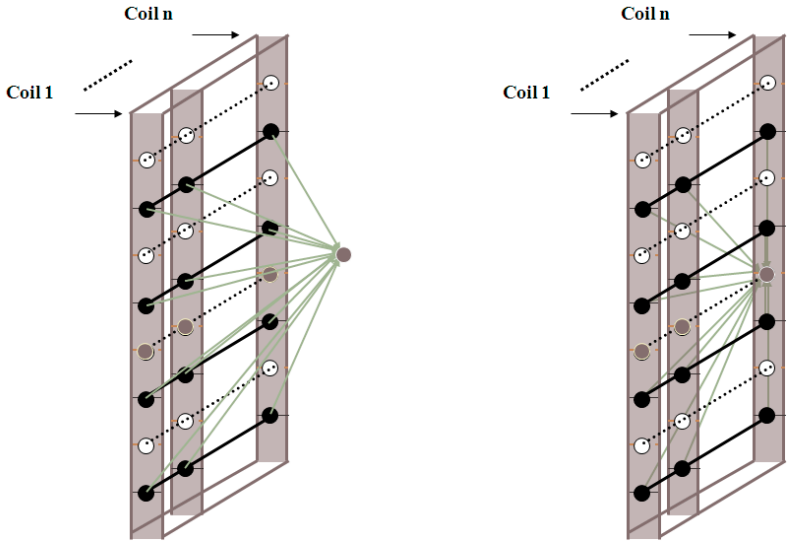

Figure 1-3 The schematic view of basic (a) VD-AUTO-SMASH and (b) GRAPPA methods. For VD-AUTO-SMASH or SMASH techniques, acquired lines from each coil are used to fit a single composite line whereas for GRAPPA, those are used to fit an ACS line in coil 4 to estimate GRAPPA coefficient. In this manner, SMASH produces one unaliased composite image whereas GRAPPA produces unaliased images for each number of coils. For GRAPPA, we then combine each unaliased image by sum of squares to make one final composite image.

1.3 Non-Cartesian Parallel Imaging in fMRI

Even though both SENSE and GRAPPA were first introduced in Cartesian domain [7,12], we mainly focused on reconstructing spiral k-space data, since spiral scan is often desirable for functional studies due to its robustness to motion and flow artifact, and the efficient use of gradient strength. However, spiral parallel imaging schemes have enjoyed only limited use, due to their computational complexity in parallel image reconstruction in general. Nonetheless, there have been several attempts to overcome this difficulty in

implementing spiral parallel imaging methods.

Recently, GRAPPA and SENSE have been extended to accommodate spiral trajectories [19-22]. Unlike the Cartesian case shown in Figure 1-2, spiral k-space acquisition trajectories possess complicated point spread functions (PSF), leading to more complex aliasing artifact, as shown in Figure 1-4, when reduced data is acquired. Thus, more careful examination is required for spiral trajectories.

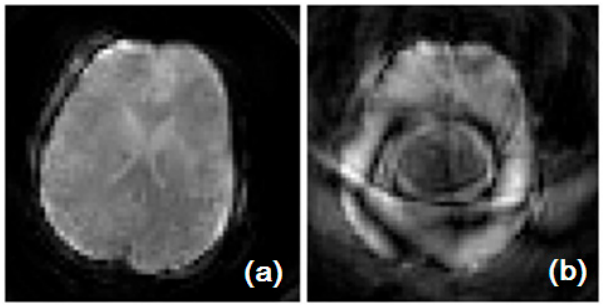

Figure 1-4 (a) *In-vivo* human image from fully sampled data, and (b) aliasing patterns of from reduced (half Fourier) data for spiral trajectory

1.3.1 Spiral SENSE

We cannot use a simple direct unfolding process in spiral SENSE, such as that used in Cartesian SENSE, because undersampled spiral k-space trajectories have complicated point spread functions (PSF). Thus, we need to consider other reconstruction methods of higher computational complexity. Pruessmann et al. showed that we can apply SENSE to arbitrary k-space trajectories via gridding and conjugate-gradient iterative reconstruction [22].

Sutton et al. [19] introduced a method that is an iterative time-segmented Non-Uniform Fast Fourier Transform (NUFFT) approach that allows for compensation of field

inhomogeneity effects during the readout. We focus on Sutton's method, since this allows compensation of the field inhomogeneity effects during the readout. In this method, the received signal from *l*th coil is modeled as

$$y_l(t) = \int s_l(r) f(r) e^{-i2\pi(k_r(t)r + \omega_0(r)t)} dr + n_l(t) \tag{1.3}$$

where $s_l(r)$ is the sensitivity map of *l*th coil, $f(r)$ is the proton density, $\omega_0(r)$ is the off resonance frequency and $n_l(t)$ is the noise. In a discretized format, this becomes,

$$y_l = \tilde{A} S_l f + n_l \tag{1.4}$$

where $a_{jl} = e^{-i2\pi(k_r(t_j)r_l + \omega_0(r_l)t_j)}$ is the entries of $\tilde{A}$ and S_l is a diagonal matrix of sensitivity map matrix. When we stack the equations (1.4) for each coil, the result is

$$y = Af \tag{1.5}$$

which is the system matrix for reconstructing the image from undersampled data using the sensitivity maps. We then estimate the image, *f*, by solving this system equation with a regularized least squares cost function,

$$\begin{aligned} &\Psi(f) = \frac{1}{2}\|y - Af\|^2 + \beta R(f) \text{ so that,} \\ &\hat{f} = \arg \min_{f} \Psi(f) \end{aligned} \tag{1.6}$$

where y is the k-space data, A is the system matrix, f is the image to reconstruct, $R(f)$ is the regularization function and β is its smoothness parameter. In this method, a temporal interpolation [23] was used that was optimal in terms of minimizing worst-case interpolation error.

1.3.2 Spiral GRAPPA

Gridding is a common approach to reconstruction from spiral data, as with other non-Cartesian trajectories. This involves interpolation of spiral data onto a Cartesian grid prior to Fourier transformation. As an example of such a reconstruction technique compatible with PI method, Heberlein et al. proposed an auto-calibrated spiral GRAPPA method [20] in which they assumed that a missing k-space data and its nearest neighbors from other shots are approximately aligned along the radial direction as shown in Figure 1-5(a-b). They applied piecewise GRAPPA to individual sectors, divided in angular direction.

As an alternative, Heidemann et al. proposed a direct spiral GRAPPA method [21], in which the original constant-linear-velocity spiral data is regridded onto a trajectory with constant-angular-velocity. The trajectory was also divided into a number of groups in an angular direction in order to consider each group as a Cartesian domain as shown in Figure 1-5(c-d). Cartesian GRAPPA was then applied to each group. This is similar to the auto-calibrated approach [20] in that the trajectory is divided into a number of groups and each group is considered a Cartesian GRAPPA. However, direct GRAPPA differs from auto-calibrated GRAPPA in that it uses interpolation of k-space data by regridding the original spiral trajectory onto a different spiral trajectory, which is aligned in angular direction. On the other hand, the auto-calibrated approach assumes the alignment to be approximately angular in direction for missing k-space data and its neighbors in each sector. This approximation becomes cruder when we increase the size of the sector. Thus, we focused on the direct GRAPPA approach, since it seemed to be more accurate in estimation and more flexible in implementation than the auto-calibrated method, even

though the performances of the two methods have not yet been compared.

When implementing direct GRAPPA [21], we first remapped the original spiral data onto a constant-angular-velocity spiral trajectory. The numbers of neighbors in the angular (n_a) and radial (n_r) directions are chosen to minimize root mean square (RMS) estimation errors compared to fully-sampled data. The parameter n_a determines the number of groups that divide the new trajectory in the angular direction. Each group contains the same number of k-space samples and can be remapped to a Cartesian grid. As a Cartesian GRAPPA estimation of missing data, the GRAPPA coefficients can be obtained from the j-th coil at the m-th missing k-space line from unacquired shots.

The most central part of k-space is omitted from the above interpolation scheme because unacquired samples do not have uniformly spaced neighbors on both sides. These points are estimated separately from their neighbors using interpolation, with coefficients determined from an ACS acquisition, i.e., a neighboring shot. Once the GRAPPA coefficients and missing data are estimated, image reconstruction can proceed. Fieldmap correction is also applied at this stage using a time-segmented CP approach [23]. This reconstruction process is repeated for each coil in the array. The final image is produced from the square root of the sum of squares of the coil images.

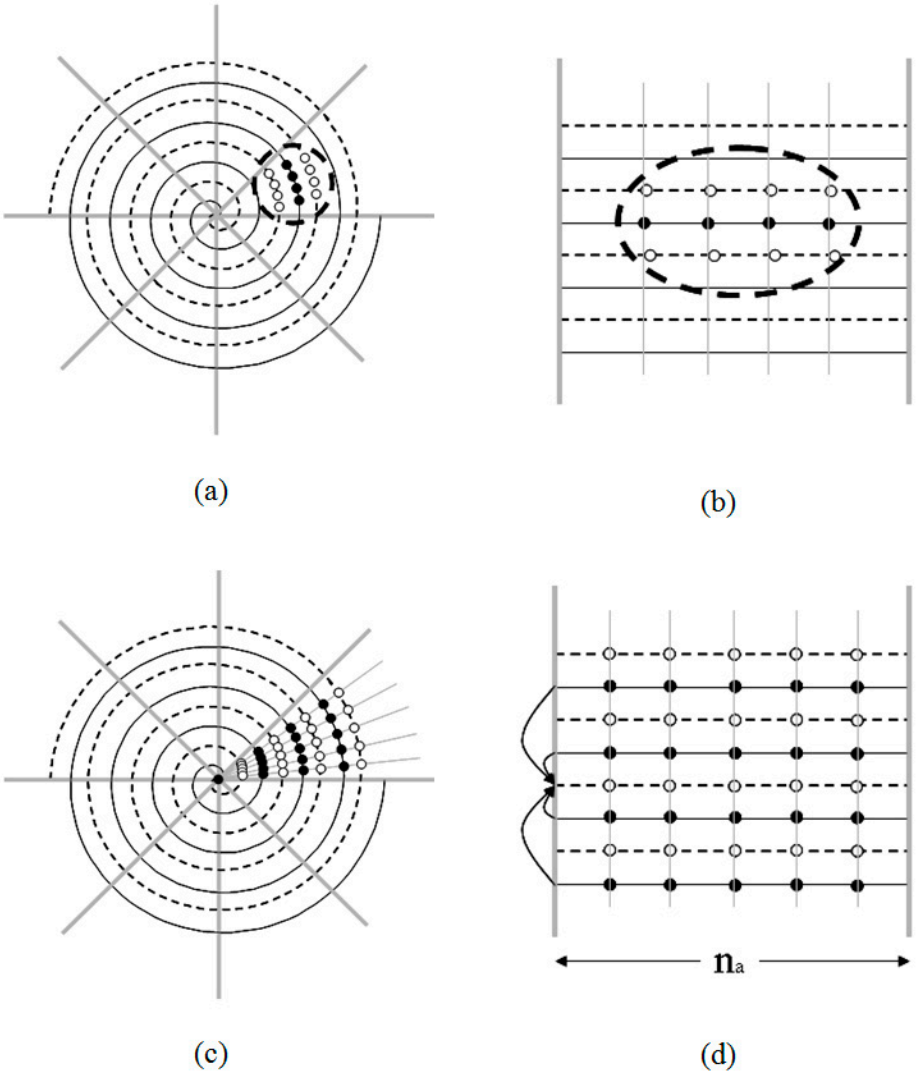

Figure 1-5 Spiral GRAPPA methods. (a-b) Auto-calibrated spiral GRAPPA (by Heberlein et al.). (a) Data within a small angular sector are approximately aligned in radial direction. (b) In each group, data is considered to be aligned in angular direction. (c-d) Direct spiral GRAPPA (by Heidemann et al.). c) The original trajectory is remapped onto constant-angular-velocity spiral trajectory and divided into a number of groups, (d) Each angular sector forms one group and each group is considered as rectilinear grid, to which we can apply Cartesian GRAPPA.

1.4 Spiral TGRAPPA and spiral TSENSE for dynamic fMRI

Functional MRI usually has time series data in which the signal intensity change in time, due to brain activity, is incorporated. When processing this dynamic, time series fMRI data, it is necessary to consider whether to update the calibration data, such as GRAPPA coefficients and sensitivity maps, and, if so, how it should be done considering the fMRI application and computational efficiency.

Both TGRAPPA [24] and TSENSE [25] are dynamic parallel imaging techniques that acquire phase encoding lines (for Cartesian trajectory) or interleaves (for spiral trajectory) alternatively at each time point, allowing for the simultaneous acquisition of calibration data in a time-interleaved manner with higher effective speed-up factors. The data from adjacent time frames are combined and can be taken as fully sampled reference data sets. Calibration data, such as coil sensitivity maps or GRAPPA coefficients, are then determined from the reference sets and updated at every time point. In this way, separate acquisition of reference data can be avoided. Thus, using a multi-shot spiral trajectory offers simple implementation of alternating acquisition schemes, such as TSENSE and TGRAPPA, which reduce readout length by undersampling the k-space while maintaining temporal resolution. For example, for a reduced acquisition method of time-interleaved techniques, such as TGRAPPA and TSENSE, with a reduction factor of R=2, the data from 2 adjacent time points are combined to determine GRAPPA coefficients or sensitivity maps. Using these calibration data, the unaliased image is reconstructed for each time point.

The time-interleaved scheme, however, produces additional temporal variations that result from imperfect reconstruction of the alternating shots. These fluctuating artifacts

are in essence, high temporal frequency components that are frequency-shifted to the edge of the band [26].

To remove the high frequency components of the fluctuating artifacts in TSENSE, temporal low-pass filtering is accomplished by the UNaliasing by Fourier-encoding the Overlaps using the temporaL Dimension (UNFOLD) method [26,27]. This temporal filtering was not applied in the original TGRAPPA method. However, since temporally frequency-shifted aliasing artifacts also occur in TGRAPPA images, low-pass temporal filtering can also be applied to TGRAPPA to suppress the fluctuating artifacts. In this study, we use the UNFOLD terminology to denote the low-pass temporal filtering in TSENSE and TGRAPPA.

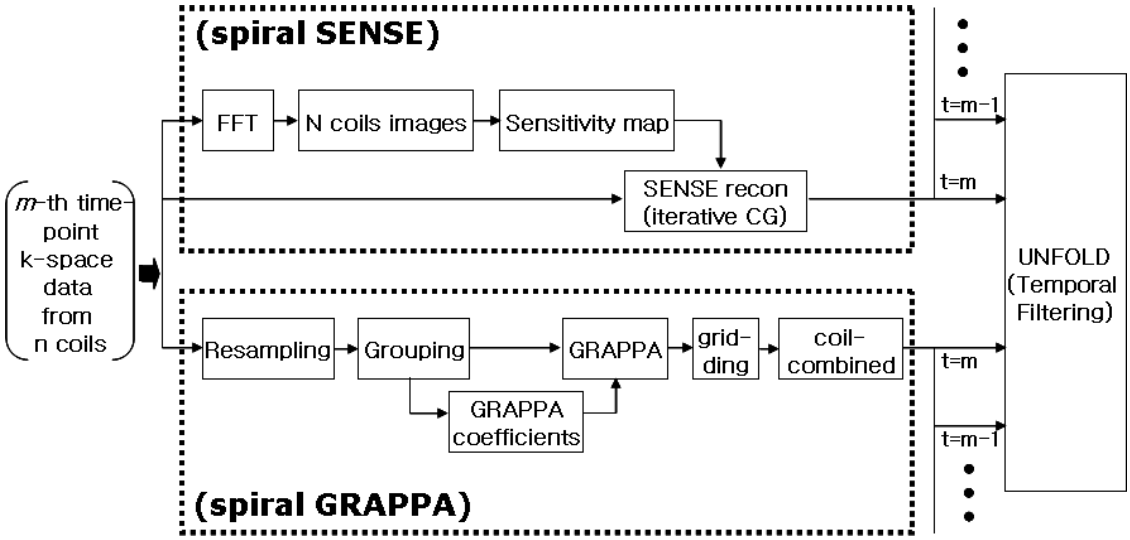

Figure 1-6 Representation of (bottom) spiral TGRAPPA and (top) spiral TSENSE with UNFOLD (temporal filtering). For spiral GRAPPA, the resampling process changes the constant-linear velocity spiral trajectory into a constant-angular velocity spiral trajectory. For spiral SENSE, iterative CG algorithm is used for unaliasing. For GRAPPA, calibration data is GRAPPA coefficient and for SENSE, senstivitiy map. Note also that coil combination process using sum of squares is required for TGRAPPA whereas it is not the case with TSENSE. Aliasing artifact that are still not perfectly removed from either SENSE or GRAPPA will be further suppressed through UNFOLD temporal filtering.

The implementations of TGRAPPA and TSENSE with UNFOLD technique are represented in Figure 1-6. As previously described, in spiral TSENSE, we used an iterative conjugate gradient (CG) method to reconstruct the final image, whereas in spiral TGRAPPA, we used the more computationally efficient conjugate phase (CP) method, followed by a sum-of-squares image combination.

1.5 Performance Criteria for Parallel fMRI

Three major criteria for assessing the performance of parallel image reconstruction techniques are the activation map, temporal SNR and image domain error. The activation map is a widely used measure for localizing brain activated by correlating stimulation task with the brain signals. Temporal SNR is required for evaluating the temporal stability. On the other hand, the image domain error itself is determined by the difference in quality between the reconstructed image, and the reference image reconstructed from fully sampled k-space data.

1.5.1 Activation map

A common approach for acquiring an activation map is through a correlation process with a certain reference waveform that can be modeled as a sinusoidal function or a "boxcar" function, which is designed according to a task paradigm [28,29]. After acquiring an activation map, the map is thresholded to determine the activated region in the brain.

The simple way to find such a threshold for activation is by transforming a correlation coefficient into a *t*-value via

$$\sqrt{n-2}\,\frac{r}{\sqrt{1-r^2}} \tag{1.7}$$

where (*n*-2) is the degree of freedom. For functional series data, *n* is equal to the number of entire time points and *r* is the correlation coefficient. The number of activated pixels, which is crude but also widely used in fMRI, is calculated by choosing the pixels above the threshold.

1.5.2 Temporal SNR

Unlike the image domain performance criteria, temporal SNR (TSNR) includes temporal fluctuation in a signal that comes from drifts, instrument instabilities, and motions, such as those induced by respiratory and cardiac activities [30,31]. TSNR is a useful measure of time course stability that has been widely used in fMRI data analysis. It is calculated by dividing the temporal mean of time series of image by its standard deviation and is defined as

$$\mathrm{TSNR} = \frac{\mu}{\sigma} = \frac{\mu}{\sqrt{\frac{1}{n}\sum_{i=1}^{n}(x_i-\mu)^2}} \tag{1.8}$$

where n is the number of time point, x_i is the time series, μ is the mean signal intensity and σ is the temporal standard deviation.

1.5.3 Image domain error

The image domain performance of fMRI is affected by various factors, such as head movement, physiological noise and instrument drift. It is mostly evaluated through image error between the reconstructed image and the reference image. For partially acquired k-space data, which are used in parallel imaging, we can set the reference image with the fully sampled k-space data. Thus, image domain error is defined as follows.

$$\text{image domain error [\%]} = \frac{\left\| \text{fully sampled image - reconstructed image} \right\|}{\left\| \text{fully sampled image} \right\|} \times 100 \qquad (1.9)$$

where $\|\cdot\|$ denotes the Frobenius norm.

1.5.4 Geometry factor (g-factor) map

A geometry factor (g-factor) map can be another image domain performance criterion for fMRI when applying parallel imaging. It was firstly presented by Pruessman [7] for SENSE, and describes the spatial variations in noise pattern based on coil configuration. In mathematical form, it is defined as

$$g_\rho = \sqrt{\left[\left(S^H \Psi^{-1} S\right)^{-1}\right]_{\rho,\rho} \left(S^H \Psi^{-1} S\right)_{\rho,\rho}} \geq 1 \qquad (1.10)$$

where ρ denotes the index of the voxel, S is the sensitivity map matrix and Ψ is the receiver noise matrix. The value is always at least equal to one, one being the best performance. It is called a 'geometry factor map' since it is strongly dominated by coil geometry and describes the ability to separate aliased pixels by coil configuration. Thus, g-factor map is also used to provide an important criterion for the geometric design of coil arrays. In addition, this g-factor map also allows for an estimate of image SNR via:

$$SNR_{\rho}^{red} = \frac{SNR_{\rho}^{full}}{g_{\rho}\sqrt{R}} \leq \frac{SNR_{\rho}^{full}}{\sqrt{R}} \tag{1.11}$$

for each image voxel, ρ. This relation gives an upper limit for image SNR from reduced sampled data by the square root of the reduction factor, R, and image SNR from full Fourier encoded data.

Even though g-factor map has firstly been introduced for SENSE, there also have recently been several attempts to define g-factor map for GRAPPA [32,33]. The pseudo multiple replica approach by Robson et al. [32] requires time-consuming image reconstruction steps, practically using at least 100 images, in order to have accurate results, whereas Breuer's approach [33] provides faster approach by direct calculation from GRAPPA coefficients.

1.6 Current applications of Parallel Imaging in fMRI

Despite the SNR reduction due to g-factor or reduced number of samples, the main benefit of applying parallel imaging in fMRI is a reduction of susceptibility artifacts as demonstrated in Figure 1-7. In addition, parallel imaging has a number of other critical benefits for fMRI in improving spatial and temporal resolutions as well as reducing acoustic noise as summarized by Golay [6] and de Zwart [5]. Reduction of acoustic noise will be effective especially when using EPI, by reducing the sampling bandwidth which, in turn, reduces the gradient slew rate, the major source of acoustic noise [5,6,34].

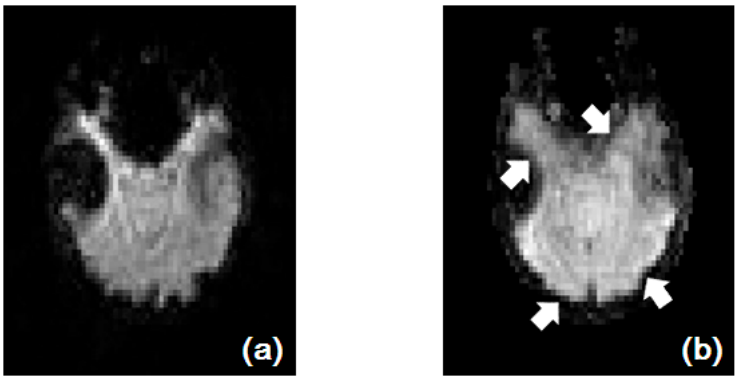

Figure 1-7 The major benefit of using parallel imaging in suppressing the susceptibility artifact by reducing the readout length from (a) 18ms to (b) 9ms (SENSE: parallel imaging)

The various attempts of researchers to apply parallel imaging to fMRI have been largely successful. Weiger [4] demonstrated the advantages of single-shot spiral SENSE with an iterative image reconstruction, especially in signal recovery of activation in regions affected by field inhomogeneity as well as improved image resolution. Despite the SNR reduction due to the shortened readouts as well as difficulties in reproduction of stimulation response, he showed there was sufficient evidence that SENSE has the potential to improve detection of BOLD fMRI activation in brain regions affected by those susceptibility artifacts.

De Zewart [34] showed that "the SNR penalty incurred with SENSE does not necessarily lead to an equal loss in fMRI sensitivity". FMRI sensitivity is a far more critical factor than image SNR in fMRI. In fact, Moeller has shown that SENSE at 7T using 32 channels with a fourfold reduction factor leads to a larger number of activations due to reduced temporal fluctuation [35]. He has also shown that using more channels is more beneficial compared to their previous study using 8 channels [36].

On the other hand, researchers such as Lutcke [37] and Preibisch [38] reached quite different conclusions using parallel imaging in fMRI at 2.9T and 1.5T, respectively, where they reported that the number of activated pixels are actually reduced using the parallel imaging.

Regardless of reported disadvantages, there have been various attempts by many researchers who tried to apply parallel imaging methods to their functional studies and have proven parallel imaging method to be successful in analyzing their fMRI data [4,39-45]. Furthermore, parallel imaging in fMRI has the potential at higher fields to overcome drawbacks from susceptibility artifacts and RF energy absorption as well as reduced acoustic noise [46]. Since signal intensity increases directly proportional to the field strength, higher field strength can also perform as an increased baseline of signal-to-noise ratio (SNR), countering the main drawback of parallel imaging, as well as enhanced BOLD sensitivity, which in turn, can improve image quality and spatial resolution or acquisition speed compared to the lower field strength [47,48]. Thus, parallel imaging and high field technique can complement each other. In other words, the main strengths of parallel imaging complement the weaknesses of high fields. For example, parallel imaging reduces the length of readout, which in turn, results in reduced susceptibility artifact. We believe that fMRI community has a strong trend to use higher field due to the potential in improving spatial resolution as well as higher sensitivity for functional activation [43,47,49]. Since the susceptibility artifact will also become more problematic at higher field, the potential benefits that parallel imaging technique in fMRI at higher field is compelling.

Thus, it becomes obvious from the particular issues described in previous studies, parallel imaging can become a powerful tool to provide more useful of activities in the brain regions that until now have been hidden by the signal loss or limited resolutions.

However, for parallel imaging to be more applicable to fMRI, there are several issues to be solved, since it still suffers from various kinds of noise, leading to low SNR. Other than errors of a systematic nature such as inhomogeneous field, eddy currents, or gradient non-linearity, other possible sources of noise in parallel imaging are noise in sample values. The sources of noise comes from reduction of number of data, which result in SNR reduction or increase in g-factor. Furthermore, noise in calibration data, such as the sensitivity maps or GRAPPA coefficients, as well as coil configuration could also affect SNR. Although increased SNR at higher field can effectively outweigh the SNR penalty inherited with parallel imaging, SNR reduction can still be an issue, especially with a high reduction factor.

SNR for parallel imaging can be improved not only by using higher field but also by increasing number of coils [50] or well designing of better array coils. Various attempts on designing coil array have been made to further improve parallel imaging, since MR community has discovered that parallel imaging can be optimized by reducing coupling between surface coils. Coil coupling, even if well characterized and carefully incorporated in the reconstruction process, can still give lower baseline for SNR than uncoupled coil array system. Thus, researchers have tried to design optimal coil arrays that achieve more orthogonal sensitivity profiles, eliminating noise correlation, thus producing higher SNR [51-54].

However, additional approaches could be made by signal processing approach by mitigating possible source of noise during the image reconstruction. For example, noise in calibration data, such as sensitivity map or GRAPPA coefficient, is another major source which could be improved by applying unbiased coil combination technique [17] or by improving estimation of sensitivity map [55-57].

1.7 Research Goal

The overall goal of my research was to improve the performance of parallel image reconstruction for fMRI by mitigating possible noise sources in parallel imaging. This was achieved mainly by developing image reconstruction algorithms or improving estimation of calibration data as well as by analyzing currently existing methods. We envisioned that these approaches will further improve applicability of parallel imaging technique for time series fMRI data and in other applications. We focused on spiral trajectory since it has desirable characteristics for fMRI: robust to motion and flow artifact as well as efficient use of gradient [58-60].

1.8 Description of studies

First, we optimized the reconstruction algorithm of non-Cartesian SENSE for time series functional data. To optimize the reconstruction process, we focused on improving sensitivity map estimation by investigating various self-calibrating sensitivity map estimation methods as well as analyzing the effect of smoothing of sensitivity map

through regularization. Applying regularization to the sensitivity map estimation process also makes it feasible to control smoothness and noise of the sensitivity map in spatial and temporal domain, thus reducing image domain error and improving temporal SNR (TSNR). We also focused on details of the iterative conjugate gradient (CG) algorithm with the proper selection of image support region with quadratic regularization which controls noise and artifact.

Second, we examined optimal methods of parallel imaging in fMRI, to take advantage of parallel imaging with undersampled data. We examined the different approaches for methods of updating calibration data for parallel imaging, for example, the sensitivity map or GRAPPA coefficients. We also compared TSENSE with interleaved spiral, and SENSE with single-shot spiral, and examined initialization methods in reconstruction process which could further speed up the reconstruction process of times series fMRI data.

Lastly, we present a joint estimation approach for simultaneous estimation of the image and the sensitivity map, which was developed using an iterative conjugate gradient (CG) algorithm. The main rationale behind the technique is that the performance of SENSE is highly dependent upon the accuracy of sensitivity map estimation, and the inaccuracy of sensitivity estimation can severely degrade reconstructed images. We hypothesized that using an iterative algorithm, as in non-Cartesian SENSE could increase the degradation even further. Our joint estimation method might improve the reconstruction of both image and sensitivity map under circumstances where the initial sensitivity map cannot be estimated accurately. The second rationale is the possible convenience of not having to estimate the sensitivity map for each study. We

hypothesized there is a "global" low resolution, non-object dependent sensitivity pattern for each coil configuration that can be used as an initializer for the joint estimation method, which can robustly estimate the final sensitivity map as part of the reconstruction process.

CHAPTER 2. Improving Non-Cartesian SENSE by investigating estimation of sensitivity maps and developing improved image reconstruction algorithms

In this chapter, we focus on improving the reconstruction algorithm of non-Cartesian SENSE. To improve the reconstruction algorithm, we focused on the sensitivity map, since it forms the system matrix in (1.5), which directly influences the performance of the reconstruction. Specifically, we analyze several estimation methods for sensitivity map. We then investigated the effects of the spatial and temporal smoothing of sensitivity map on fMRI data. A quadratic regularization of image reconstruction algorithm controls noise and artifact, and applying regularization to sensitivity map estimation also makes it feasible to control smoothness and noise of the sensitivity map in spatial and temporal domain. We also sought to improve the reconstruction algorithm by developing an improved regularization method that "softens" the edges of the image support regions.

2.1 Sensitivity map estimation using a self-calibrated approach

The performance of SENSitivity Encoding (SENSE) [7,22] highly depends on the accuracy of the estimation of the sensitivity map, which is part of the system matrix used in reconstruction process. The inaccuracy of sensitivity estimation can severely degrade reconstructed images [50], especially when using an iterative algorithm, such as in non-Cartesian SENSE [22]. In this section, we investigated and compared different self-calibrated approaches for sensitivity map estimation in non-Cartesian SENSE.

Our results show that the sensitivity profile estimated from a homogeneous reference object, when using the geometric mean or harmonic mean method, usually has robust performance for both simulation and human data.

2.1.1 Methods

The conventional approach to estimate the sensitivity map is to divide each individual full-FOV coil image by body coil image which is usually homogeneous [7]. Division by the body coil image provides reliable performance when the body coil and the array coil images are accurately co-registered. However, this technique may require additional scanning, and is sensitive to motion between the acquisition of the body coil and array coil images when they are not accurately registered. Thus, to avoid such problems, self-calibration approaches have been considered, including low resolution [14,61] and sum of squares [7] or geometric mean approach [57].

The low resolution approach makes use of the center k-space region. Though this low-resolution approach turned out to be viable for spiral trajectories [14,61], if we use only the fully sampled region, we get overly smoothed sensitivity maps, and if we use outer part of undersampled k-space region, we get aliasing artifact [14]. Furthermore, for Cartesian trajectories, where k-space center regions are usually not fully-sampled, this approach could not be applied unless we use additional calibration lines, which in turn, can reduce acceleration for parallel imaging. These approaches can also suffer from contamination of image contrast in the sensitivity maps, particularly when higher resolution data are used. Furthermore, since we are dealing with dynamic imaging, such as using TSENSE-like interleaved acquisitions, we investigated other self-calibrated approaches, which seem to be more general in terms of using more k-space data.

Perhaps one of the most widely used self-calibrated sensitivity map estimation methods is dividing surface coil by sum-of-squares of all coil magnitude [7]. However, to the best of our knowledge, there has been no literature on the optimality of the sum-of-squares approach. We hypothesized that there could be other coil combination approach for reference map that would work better than sum-of-squares approach.

In this section, we investigated four different self-calibrated sensitivity map approaches: sum of squares [7,16], geometric mean [57], generalized mean and harmonic mean. The first two methods are already proposed in the literature but the latter two are new combining methods.

In TSENSE, the assumption that the sensitivity map between the neighboring time points does not change, we can also combine the undersampled data from the several neighboring time points to use them as one set of fully sampled data from which we

estimate the sensitivity map. The self-calibrated sensitivity map estimation approaches are feasible when using this combined fully-sampled data from neighboring time points. The sensitivity map of each coil is derived by dividing each coil image by the reference images via

$$S_i = \frac{c_i}{\left(c_{ref} + \varepsilon\right)} \tag{2.1}$$

where c_i is the acquired image from *i*-th coil and c_{ref} is the nonnegative reference map, followed by smoothing process. The parameter ε is added to the denominator to prevent division by zero. This can be further divided by the phase of the one of the coils to avoid the underlying object phase term from being added to the sensitivity map. The reference images can be calculated from sum of squares, geometric mean, generalized mean and harmonic mean, respectively of the individual coil image, as shown in the Table 2-1.

We implemented four self-calibrated sensitivity map estimation methods and applied each to single-shot spiral SENSE with a reduction factor of 2. Data were acquired using a TSENSE-like interleaved acquisition manner. Thus, each fully-sampled coil image was obtained from combining two neighboring shots, forming full Fourier encoded data. Using simulation data, we tested the performance of each method to see the effect of (i) sensitivity map of large coil element, (ii) drop-off of coil sensitivity using small coil element, and (iii) intensity variations in object with non-uniform pattern.

Table 2-1 Calculation of the reference image for the self-calibrating sensitivity map estimation methods

Geometric mean	$c_{ref} = \sqrt[n_c]{\prod_{i=1}^{n_c} \lvert c_i \rvert}$
Sum of squares	$c_{ref} = \sqrt{\sum_{i=1}^{n_c} \lvert c_i \rvert^2}$
Generalized mean (p=1, Arithmetic mean)	$c_{ref} = \sqrt[p]{\frac{1}{n_c} \sum_{j=1}^{n_c} \lvert c_j \rvert^p}$
Harmonic mean	$c_{ref} = n_c \Big/ \sum_{j=1}^{n_c} \frac{1}{\lvert c_i \rvert}$

2.1.2 Results

Figure 2-1 contains simulation results of using sensitivity maps from each of the four self-calibrating estimation methods: (1st column) geometric mean, (2nd column) sum of squares, (3rd column) generalized mean with p=1 which corresponds to arithmetic mean, and (4th column) harmonic mean approach. 1st row shows estimated sensitivity patterns of one of the four coils in the array, 2nd row shows reconstructed SENSE images, 3rd row shows error maps calculated by taking difference between the estimated image and the original image, and 4th row shows original (red) and estimated (blue) image profiles along the central line. The error maps are all scaled same for fair comparison among the estimation methods. Figure 2-1 contains the simulation result for large coil elements (slowly varying sensitivity), Figure 2-2 for small coil elements (steep sensitivity pattern) and Figure 2-3 for small coil elements with object with non-uniform pattern.

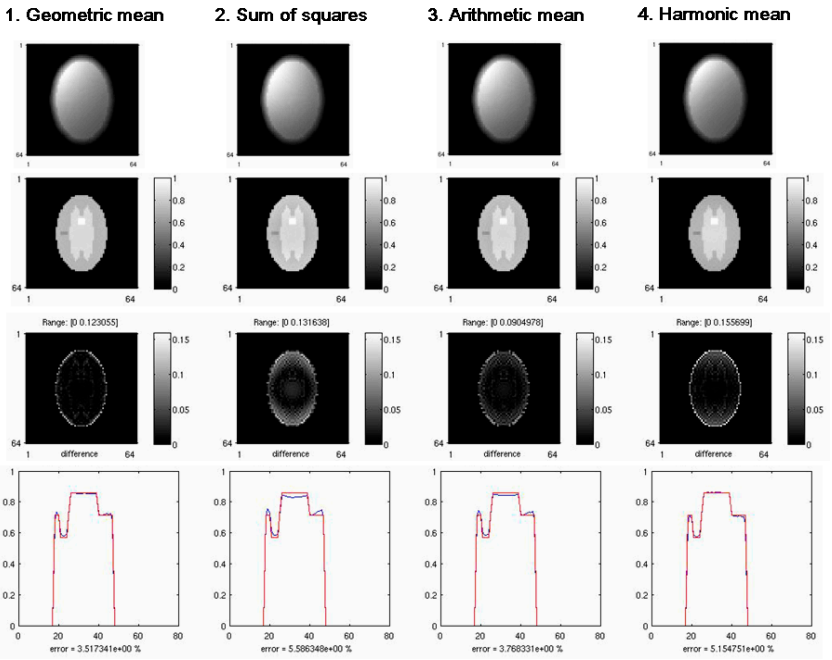

Figure 2-1 Simulation result with large coil element. (1st row) Estimated sensitivity map of 1st coil, (2nd row) estimated image, (3rd row) error map, and (4th row) the original and estimated image profile in red and blue, respectively.

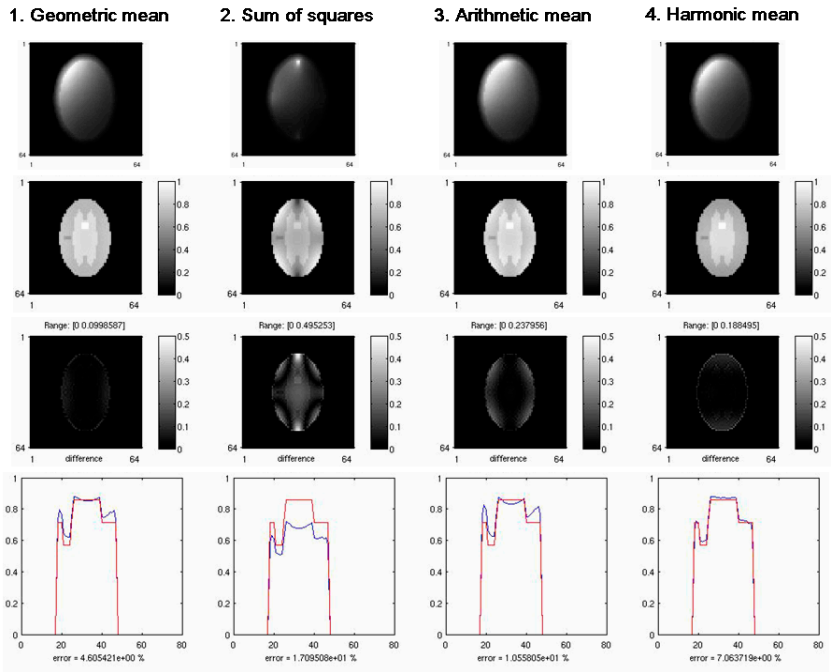

Figure 2-2 Simulation result with small coil element where the sensitivity pattern drops steeply as it moves away from the coil. (1st row) Estimated sensitivity map of 1st coil, (2nd row) estimated image, (3rd row) error map, and (4th row) the original and estimated image profile in red and blue, respectively.

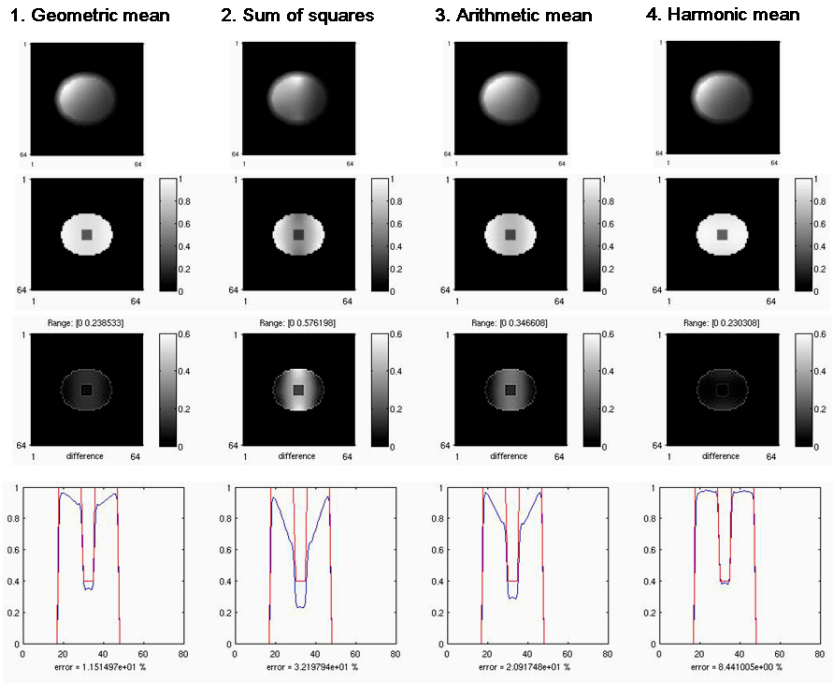

Figure 2-3 Simulation result with small coil element with an object with low SNR in the center. (1st row) Estimated sensitivity map of 1st coil, (2nd row) estimated image, (3rd row) error map, and (4th row) the original and estimated image profile in red and blue, respectively.

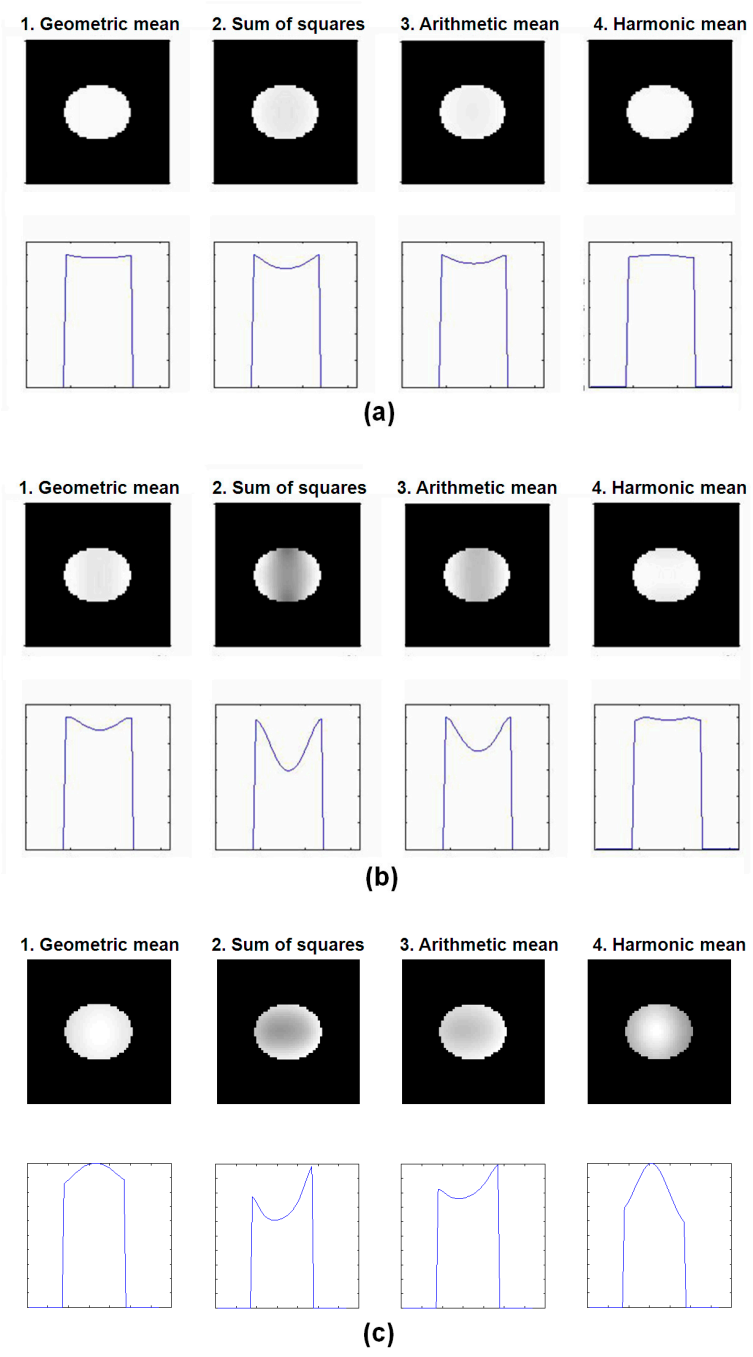

Figure 2-4 (top) Reference maps and (bottom) their profiles of uniform circular object using four different sensitivity map estimation approaches from (a) large coil element, (b) small coil element used in previous simulation, and (c) smaller coil elements with 32 channels.

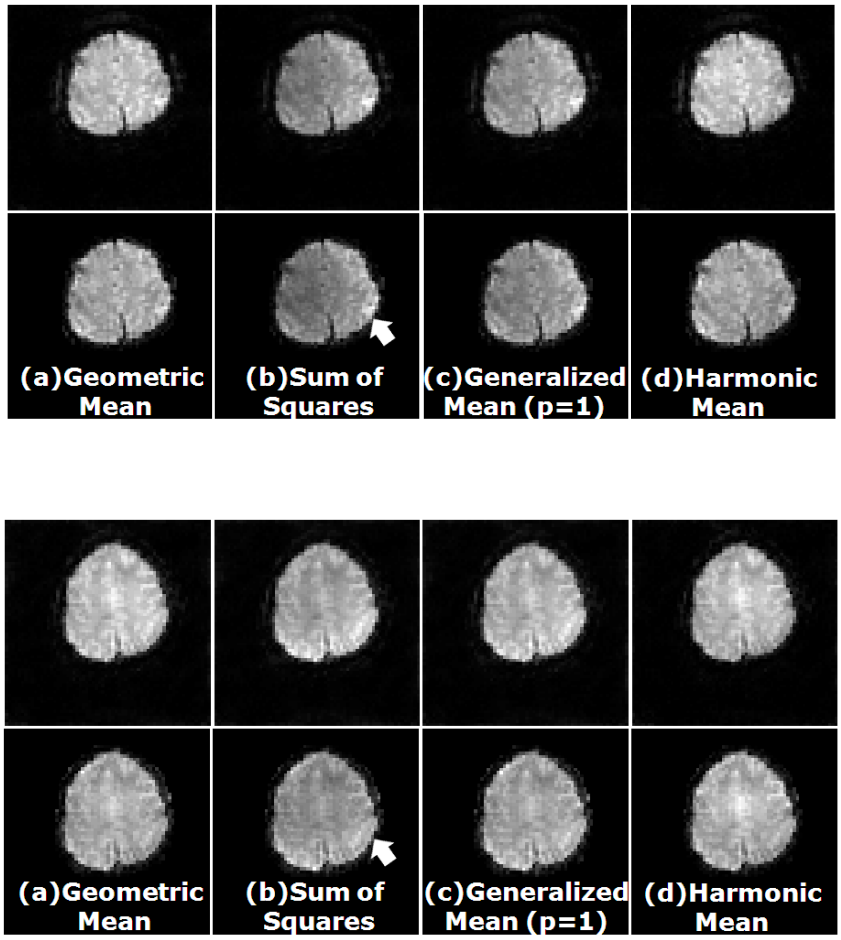

Figure 2-5 ***In-vivo*** **human results from 2 different subjects. For each subject, (top) reference map for sensitivity map estimation and (bottom) corresponding SENSE images (R=2) using each self-calibrated approach, (a) geometric mean, (b) sum of squares, (c)generalized mean (p=1), and (d) harmonic mean. (top, b) Sum of squares has non-homogeneous profile compared to other approaches which produced (bottom, b) SENSE image with brighter spot around the edges, whereas geometric mean and harmonic mean have relatively homogeneous profile for reference map for both cases, consistent with simulation results.**

From these results, image domain error from the reference object were compared and we see that the geometric mean approach led to the best image quality, producing a reconstructed object that was closest to the true reference object for the first two experiments, and the harmonic mean approach produced the best result for the last experiment. The estimated image profiles from the experiments with small coil elements show the geometric mean and harmonic mean approach leads to most flat profile among all the other sensitivity map estimation methods, which could be explained by comparing the profile of reference sensitivity estimated by different approaches. In Figure 2-4, the reference images and their profiles from (a) large coil element, and (b) small coil element, from 4 channels that was used in simulation experiment shown in Figure 2-1 through Figure 2-3 for uniform elliptical object estimated from four different estimation approaches are shown. From this figure, we observe that the reference sensitivity map from harmonic mean and geometric mean approach, is generally more flat than any other approaches with small coil elements and large coil elements, which most closely mimics homogeneous body coil image, which most closely mimic homogeneous body coil image. Figure 2-4 (c) shows reference maps and their profiles from asymmetric small coil element with 32 channels. Comparing harmonic mean and geometric mean, harmonic mean approach overestimates the central part of image much more than geometric mean approach.

Figure 2-5 shows *in-vivo* results using four sensitivity map estimation methods. Images from two representative subjects are shown. For each subject, top row demonstrates reference map for sensitivity map estimation and bottom row demonstrates corresponding SENSE images (Reduction factor, R=2) using each self-calibrated

approach, (a) geometric mean, (b) sum of squares, (c) generalized mean (p=1, arithmetic mean), and (d) harmonic mean. Sum of squares has non-homogeneous reference map compared to other approaches which produced SENSE image (b-bottom) with brighter region around the edges, whereas geometric mean and harmonic mean have relatively homogeneous reference map for both cases, consistent with simulation results.

2.1.3 Discussion and Conclusions

From our experiment, geometric mean approach and harmonic mean approach produced the best results among the four tested self-calibrated sensitivity map estimation methods for both simulation and *in-vivo* human experiments. Reference profiles, shown in Figure 2-4, demonstrate the reason why those two approaches were better than other two approaches: the more flat the reference profile, the better the sensitivity map estimation. While it is still possible that different coil configuration or different object could lead to different conclusions, using our data, we have found that geometric mean or harmonic mean approach generally outperformed sum-of-squares approach, which has been widely accepted by MR community. In comparing harmonic mean and geometric mean, we found that while the harmonic mean approach showed slightly better performances in some simulations, the geometric mean approach was generally more robust and seemed to perform well in varied conditions.

We also note that the flatness of profile of the reference map could be a good indicator for selecting the best approach to self-calibrated sensitivity map estimation, as the flattest reference maps leads to the better reconstructed images.

2.2 Effect of Smoothing of the Sensitivity Map[1]

In dealing with time series fMRI data, TSENSE [25] can be used to make efficient use of time and k-space. Like other image-domain based parallel imaging techniques, the performance of TSENSE heavily relies on the accuracy of the sensitivity maps that are necessary for the unaliasing process. Thus, accurate estimation of sensitivity maps is particularly important. In TSENSE, dynamic updating of sensitivity map is feasible by computing sensitivity map from "fully-sampled" image using neighboring data. However, due to motion or system instability, sensitivity maps could change during the scan and can affect overall quality of reconstructed images. Like the spatial smoothing of sensitivity map that suggested in original SENSE paper [7], both spatial smoothing and temporal smoothing could be applied to the sensitivity maps to improve robustness to those kinds of noise.

However, the effect of smoothing has not been thoroughly investigated to date. Thus, we investigate the effects of sensitivity map smoothing on motion corrupted fMRI data, proposing a novel self-calibrated sensitivity map estimation technique that controls noise and smoothness via regularization.

2.2.1 Methods

Since TSENSE is a dynamic parallel imaging technique with a time-interleaved acquisition scheme, we can combine undersampled neighboring time point data to

[1] This section is an extension of our work found in [62].

produce a fully-sampled k-space data set. In our experiment, we acquired spiral data with a reduction factor of 2. Thus, two neighboring time points were combined to form one fully sampled k-space data. Denoting the fully sampled image for each coil l as z_l and the reference image as z_{ref} , we can estimate l-th coil sensitivity map, s_l using CG algorithm as follows :

$$\hat{s}_l = \arg\min_{s_l} \frac{1}{2}\left\| z_l - diag\{z_{ref}\}s_l \right\|^2 + \beta R(s_l) \tag{2.2}$$

where β is a regularization parameter and $R(s)$ is a 1st order spatial roughness penalty function which penalizes the roughness of the estimated sensitivity map, s_l. Smoothness of the estimated sensitivity map is easily controlled by varying β. The reference image, z_{ref}, can be obtained by taking the sum-of-squares [7], or geometric mean [57] of the individual coil images as suggested in Section 2.1. As suggested in previous section, the phase of one coil's image can further be incorporated into this term to prevent inclusion of the underlying object's phase in the sensitivity map. Compared to conventional sensitivity map estimation approach which uses division of surface coil image by a reference map, our approach can further improve robustness to noise in regions with low signal intensity and near edges, since the direct division is avoided.

To see the effects of spatial smoothing using our proposed approach, sensitivity maps were estimated with different smoothness factors by varying β. To determine the effects of temporal averaging of sensitivity maps, we changed the number of neighboring time points used for moving averages.

We hypothesized that this spatial smoothing could mitigate problems with noise around the edges of the sensitivity maps and that the temporal smoothing could potentially deal with inconsistencies in the estimated sensitivity maps due to motion.

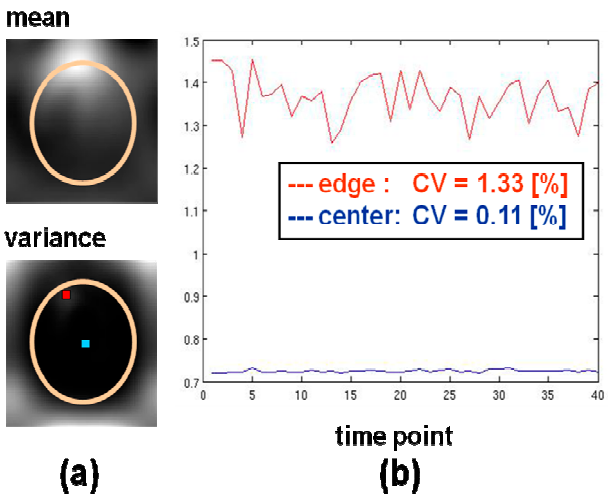

Figure 2-6 (a) Mean (top) and variance (bottom) of complex sensitivity profile over all time points. (b) time course of sensitivity map estimate at the center (blue) and at around the edges (red) of the head

2.2.2 Experimental Methods

We collected functional data on a 3T GE scanner with an 8-channel head array coil. Imaging parameters were TR = 2s, TE = 25ms, 64×64 matrix size, FOV = 22cm, 5-mm thick axial slices, and two-shot gradient echo spiral-out acquisition, each shot being undersampled by a reduction factor of 2. During the scan, a visual cue, smaller than entire screen, moved and the subject was instructed to move his head right or left in response to the position of a visual cue on the screen so that the motion can be generated. We acquired a total of 40 time points.

We estimated sensitivity maps using the above described approach and varied the spatial or temporal smoothness by controlling smoothness factors by varying β or by choosing different number of temporal averages of sensitivity maps, respectively.

Estimated sensitivity maps were then applied to iterative SENSE reconstruction with

CG algorithm with 17 iterations. As proposed in the original TSENSE method, UNFOLD [26] was also used to remove the high frequency artifacts created by alternating interleaves. Temporal SNR (TSNR) and image domain error were used as metrics for comparing the results.

2.2.3 Results

Our observations of the temporal variation of the sensitivity maps provides evidence that the estimated sensitivity map values in the periphery vary over time more than central regions in the object. Figure 2-6(a) shows the magnitude of the mean (top) and variance (bottom) of a complex sensitivity map over time. The time course of two voxels of the sensitivity map, one at the center (blue) and the other one close to the edge (red), are plotted in Figure 2-6(b). The coefficient of variation ($=\sigma/\mu$) as known as CV, were also calculated for each voxel and are also shown. Higher CV values in the edges indicate increased temporal fluctuation over that of the center of the object.

We analyzed the effect of spatial and temporal smoothing in terms of image domain error [%] and TSNR [dB]. Figure 2-7 is an example from one subject demonstrating that spatial smoothing of sensitivity maps reduces image domain error and improves TSNR, (circle) before and (star) after motion correction by MCFLIRT [63]. However, over-smoothing ($\log_2(\beta)>7$) degrades both performance metrics. Figure 2-8 shows (a) sensitivity maps and (b) corresponding SENSE images with respect to the smoothness parameter, $\log_2(\beta)$, which is shown as the numbers shown at lower right corner. This suggests that a good sensitivity map can be obtained by appropriately selecting the smoothness of the sensitivity maps. Figure 2-9 shows the mean and standard deviation of

error and TSNR from 7 subjects with respect to the smoothness parameter, confirming the generality of this finding.

Furthermore, our results in Figure 2-10 and Figure 2-11 demonstrate that temporal smoothing of sensitivity maps also reduces image domain error and improves TSNR, with the number of neighboring time points used for the moving average. Further investigations of up to 80 moving averages from four subjects are shown in Figure 2-11 where the average of (blue circle) image domain error [%] and (red star) TSNR [dB] over all four subjects are shown. Due to the intersubject variability, the trend is not as clear as the result from this single subject, but the overall image domain error decreases and TSNR tends to increase as the number of moving average increases, consistent with the result shown in Figure 2-10.

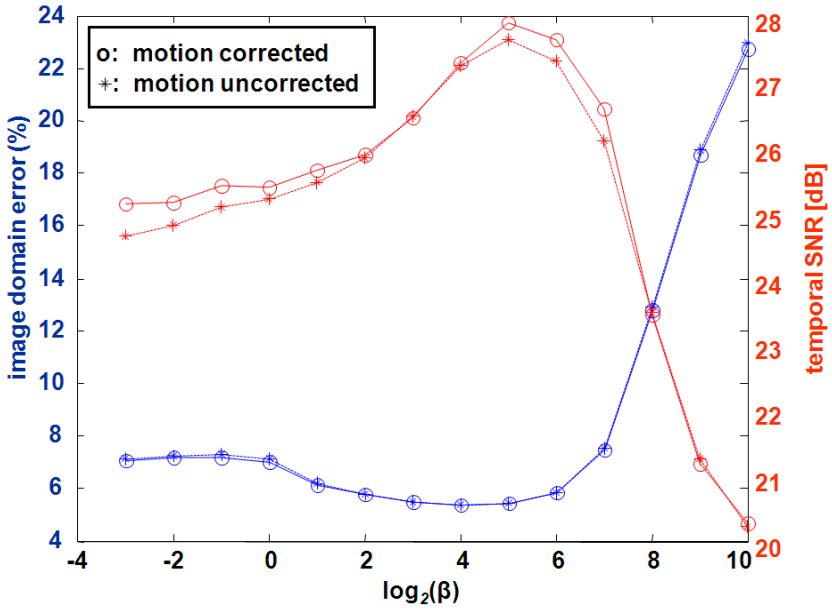

Figure 2-7 Effect of spatial smoothing of sensitivity maps measured as image domain error [%] and TSNR [dB]

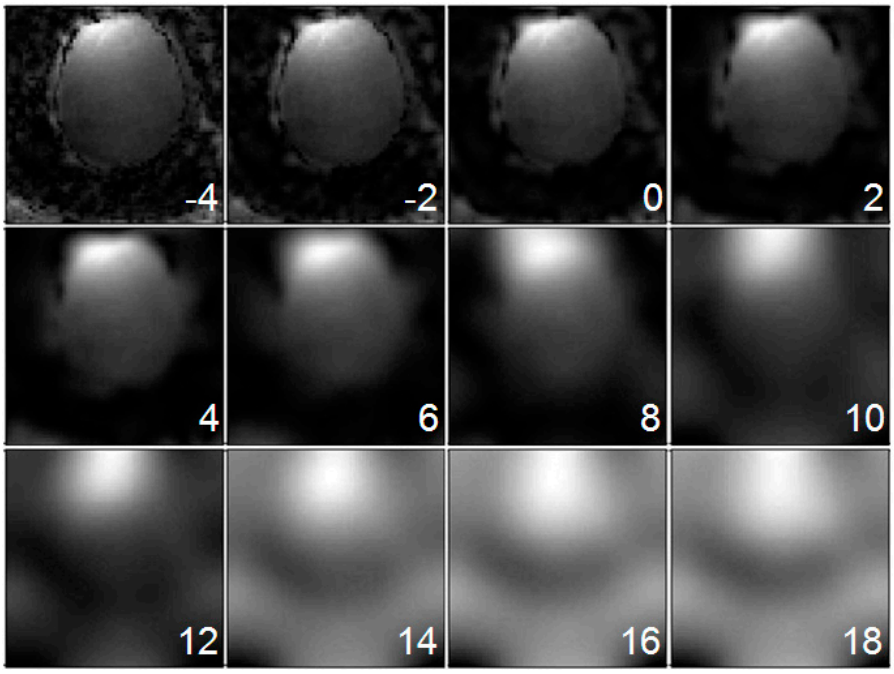

(a)

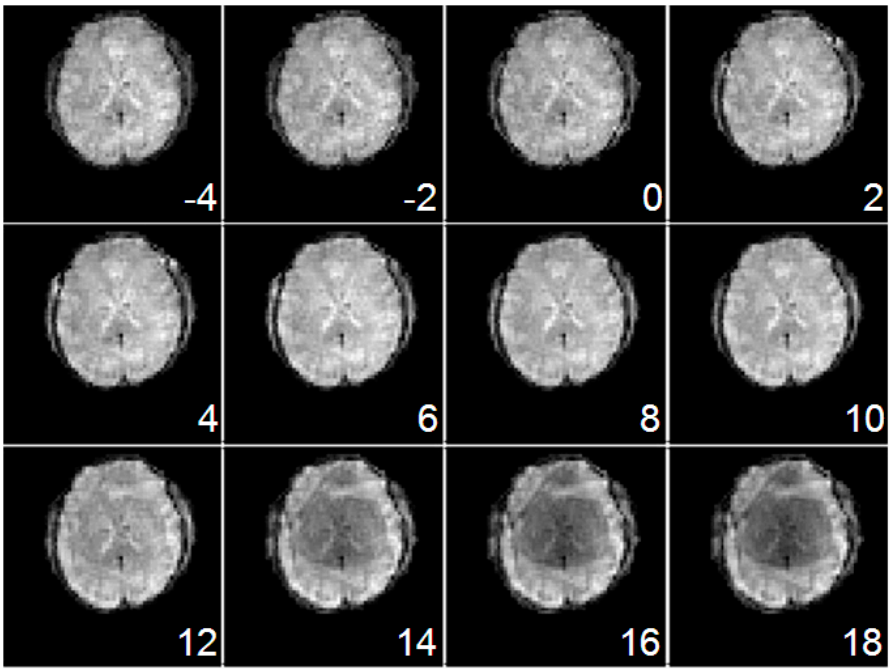

(b)

Figure 2-8 (a) Sensitivity map and (b) corresponding SENSE images with respect to the smoothness parameter, $\log_2(\beta)$

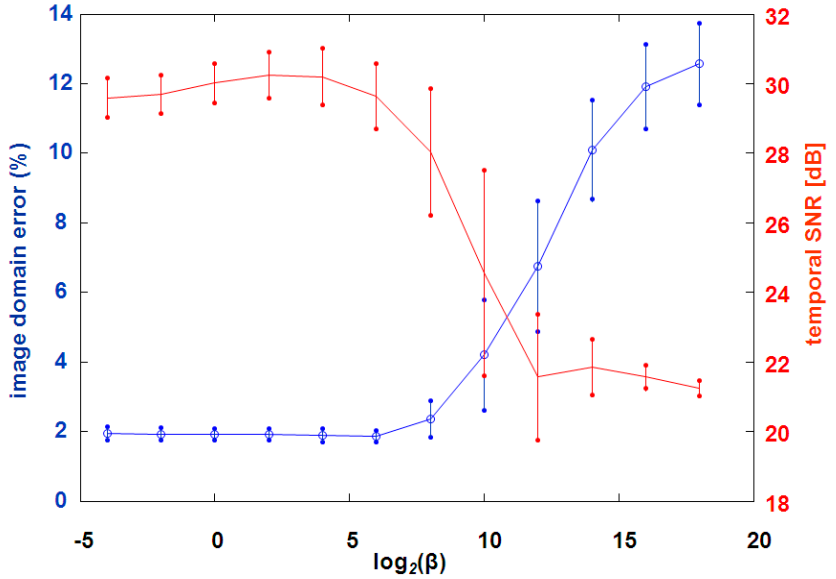

Figure 2-9 Effect of spatial smoothing (regularization) of sensitivity map estimate shown as mean and standard deviation of (blue) image domain error and (red) TSNR from 7 subjects.

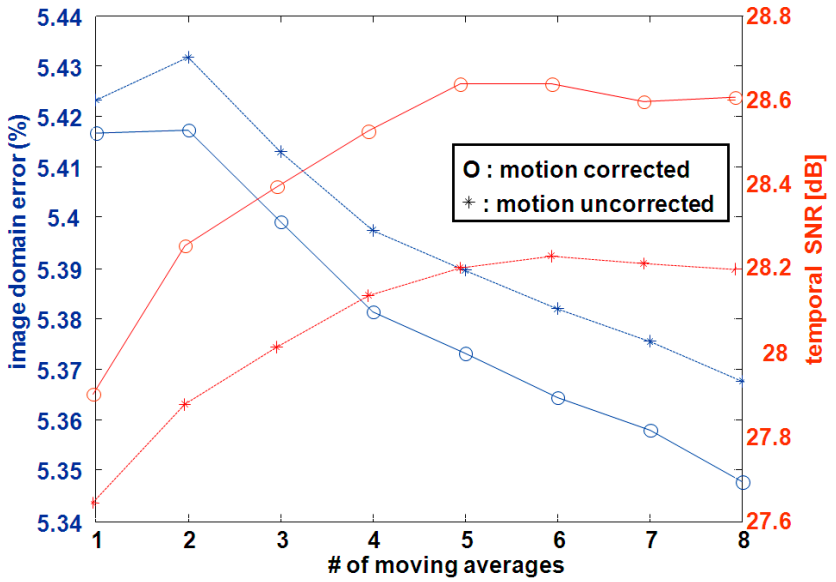

Figure 2-10 Effect of temporal smoothing of sensitivity map measure as (blue) image domain error [%] and (red) TSNR [dB]

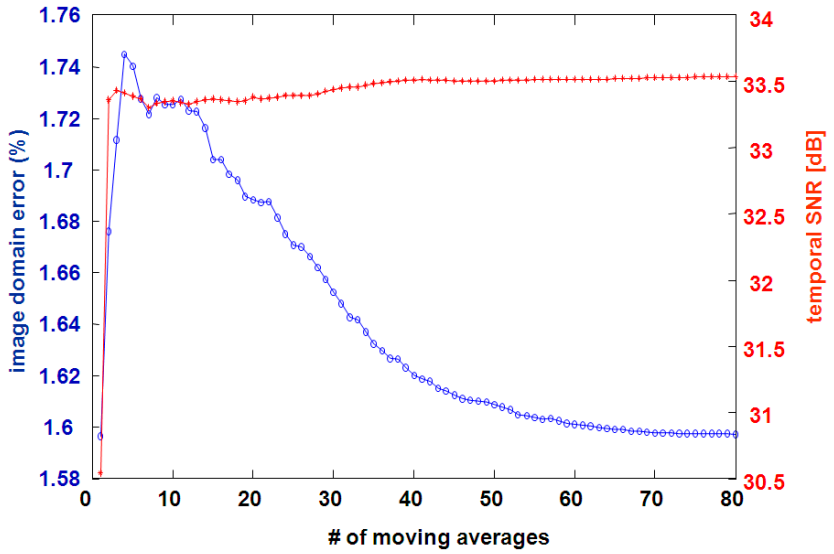

Figure 2-11 Effect of temporal smoothing of sensitivity map measure as the average of (blue circle) image domain error [%] and (red star) TSNR [dB] from four subjects

2.2.4 Conclusions

Effect of spatial and temporal smoothing on the sensitivity map has been demonstrated with image error and TSNR. Appropriate spatial smoothing reduces image domain error and increases the TSNR whereas, for temporal smoothing, the more temporal average we take, the more improvement on both performance criteria.

2.3 Selection of image support region using spatially variant regularized approaches[1]

Selection of image support region (masking region) with advanced regularization for non-Cartesian SENSE is presented [64]. Non-Cartesian SENSE involves solving a very large system of equations and further, has a complex aliasing pattern, so typically an iterative algorithm is used to reconstruct these images. For this case, proper masking can improve the conditioning of the reconstruction by excluding the regions that are not of interest. We have investigated how the selection of image support region affects the performance of non-Cartesian SENSE reconstruction applied to undersampled, single-shot spiral k-space data. We also applied an additional regularized term to control the smoothness of mask region around the edges. We tested our hypotheses on masking effects with both simulation and *in-vivo* human data and our results show that using a moderate size mask can improve the image quality. We also found that smoothing the mask using the additional regularized term is effective in suppressing aliasing artifact.

2.3.1 Introduction

Compared to the well-behaved, highly localized and equi-spaced aliasing pattern that result from undersampling with Cartesian k-space trajectories, undersampling in non-Cartesian k-space results in a more complex and widespread aliasing pattern, in which all pixels in the reduced sampling image interact with the point spread function of all other

[1] This section based primarily on our work found in [64]

pixels in the image. Typically, iterative conjugate gradient algorithms are required to "unfold" the aliasing across the image [19,22]. Thus, the role of the image support region, referred herein as a 'mask' which specifies the reconstruction region of interest, can have a global effect and thus becomes a more important factor in non-Cartesian SENSE.

The image support region has been used as prior knowledge in image reconstruction and has already proven to be effective in achieving better performance in many areas to improve image quality [65-67]. Sedarat used prior knowledge on the support region of the image to solve the reconstruction problem from incomplete data via gridding where they assumed that object is confined within a circle [65]. Information of finite support was also applied to tuning a kernel in gridding approach and has shown to produce better results for their reconstruction performance [66]. The effect of choosing the finite support region has been further investigated by Plevritis [67] and has shown to be effective in low SNR case.

Thus, image reconstruction of incomplete non-Cartesian data sets, such as parallel imaging with a reduced number of acquisitions, where the poor conditioning is a major concern and where noise in the measurement can be amplified, the use of prior knowledge may be essential in achieving better image quality. We envision that this will be especially true when using an iterative algorithm where small error in the model can possibly lead to a large degradation of resulting images. However, to the best of our knowledge, there has not yet published any work on the effect of selecting the image support region for reconstructing non-Cartesian SENSE using an iterative process.

We investigated how different choices of image support regions affects the performance of non-Cartesian SENSE reconstruction with undersampled, single-shot

spiral k-space data. To examine the effect of sharp changes around the mask edges as a possible source of image artifact, we also propose using an added spatially variant regularization term, a so-called 'soft mask', to smooth the edges. We expect potential improvement on performance of the reconstruction by constraining regions that are known to be zero and suppressing edge artifacts. We tested the effect of selecting the size of image support region or a soft mask on simulation data and also on time series functional data. The time series functional experiment was to see if we should also consider the effect of possible motion when selecting the image support region.

2.3.2 Theory

Size of the Mask:

Non-Cartesian SENSE, as described in Section 1.3.1, uses an iterative conjugate gradient (CG) algorithm rather than a direct unfolding process due to the complex aliasing pattern. With a reduced acquisition, the image reconstruction process solves an ill-conditioned problem. Our goal was to improve the system condition by using a priori knowledge of image support region. Thus, we applied a mask with a properly selected image support region, so we can exclude background points from x, making the system matrix, A, 'thinner' which in turn, can result in a better conditioned reconstruction with fewer unknown variables.

Smoothness of the Mask:

Our preliminary experiments point to limited aliasing artifact when using a tight mask, but this often led to edge artifacts, which were revealed as brightening of the image

around the edges as shown in Figure 2-12(a) (black arrow). This comes from small inaccuracies in the mask size when it does not fully cover the image, which was also observed in [68] for an 1-dimensional case. At any mask size, we also found that the sharp edges of a conventional mask seem to contribute to aliasing artifact. Thus, we applied an additional term to the regularization function, $||D(b)x||$, which gradually increases Tikonov regularization of the image outside a tight mask, which, by progressively suppressing image intensity outside the object, leads to an effective smoothing of the mask around the edges, producing a 'soft mask'. This yields the cost function,

$$\Psi(x) = \frac{1}{2}\|y - Ax\|^2 + \beta R(x) + \gamma \|D(b)x\|^2 . \qquad (2.4)$$

Here, $D(b)$ is a diagonal matrix where b is a 'softening function' that dictates the smoothness around the mask edge. We used two types of softening functions, step and Butterworth function, were used in our experiment and are shown in Figure 2-14(top).

2.3.3 Methods

To determine the effect of mask size and smoothness on SENSE reconstruction, we conducted a simulation using a modified Shepp-Logan phantom image. We further conducted human experiment using a 3T GE scanner with an 8-channel head array coil. Imaging parameters were TR = 2s, TE = 25ms, 64×64 matrix size, FOV = 22 and 5-mm thick axial slices. A two-shot gradient echo spiral-out acquisition was used with a reduction factor of 2. For simulation, white Gaussian noise was added when generating data, so as to mimic measurement error. The sensitivity map used for generating the simulated k-space data was used in the reconstruction process to avoid any possible

artifact caused by inaccuracies in sensitivity map estimation.

On the other hand, for the human experiment, the sensitivity map was estimated using self-calibrated approach with geometric mean reference as described in Section 2.2 [57]. To see the impact on a time series of data, we conducted a functional study with a visual and motor task with flickering checkerboard and a finger tapping, 4 cycles of 20s OFF / 20s ON. Then for reconstruction, we applied a same image supported region with and without softening function to all time point data. We implemented SENSE similar to Sutton et al. [19] for the unaliasing process. This implementation uses the time-segmented NUFFT algorithm which allows for compensation of field inhomogeneity effects and an iterative CG algorithm with the regularization terms as described above. The algorithm was automatically stopped after 15 iterations. Data from two shots acquired at two adjacent time points were combined and considered a fully-sampled data from which the image was reconstructed and used as a reference. An error map, which is the difference between a SENSE reconstructed image from reduced acquisition and the reference image, is shown in the results.

2.3.4 Results

Images and corresponding error maps with different mask sizes without softening function are presented in Figure 2-12. Mask size with (a) 0, (b) 1, (c) 4 and (d) 12 pixels beyond the object are shown. Mask size 0 represents the tightest mask. The error maps are rescaled to the same value. To further investigate the effect of mask size on image quality, we increased the size of the mask by one pixel at a time starting from the tightest mask which is represented as increased mask size of 0 in**Error! Reference source not**

found. Figure 2-13. The resulting image domain errors were calculated by taking the difference from and also by normalizing by the fully-sampled data set. The effect of mask size on the reconstructed image with a softening function (Butterworth) is also presented. Blue line shows the results without softening function and red line, with the softening function.

Figure 2-14(top) shows two different softening functions: (a) Step and (b) Butterworth used in our experiment, and Figure 2-14(bottom) shows corresponding error maps within the object. The arrows indicate where the differences using two softening functions are significant.

The effect of using a soft mask on human data is also presented in Figure 2-15. Figure 2-15(a,c) shows the result without Butterworth softening function and Figure 2-15(b,d) with the softening function, on the reconstructed image (top) from the slice containing motor cortices, and the corresponding error maps (bottom). The results are consistent with simulation results. For human functional experiment result, the average of normalized image domain percent error from images at 80 time points was 5.1% with the softening function with the moderate mask size of 5, and 6.6% without the softening function with the largest mask size 12. Temporal SNR (TSNR) and number of activated pixels were also calculated for each case. Using the softening function, TSNR was 32dB and the number of activated pixels was 58. However, without using the softening function, TSNR and the number of activated pixels was only 29dB and 33, respectively.

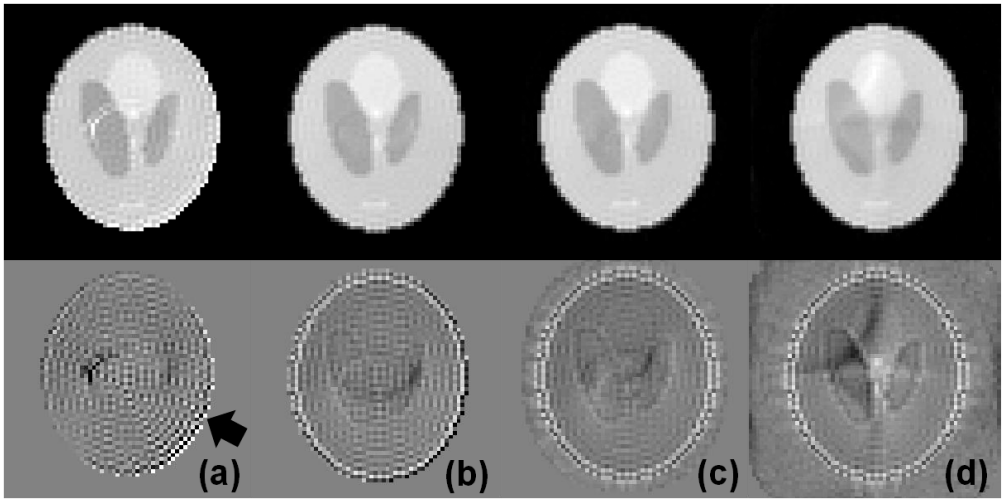

Figure 2-12 Effect of mask size without smoothing. (top) SENSE images when mask size increased by (a) 0, (b) 1, (c) 4 and (d) 12 pixels, respectively, beyond the object. (bottom) corresponding error maps

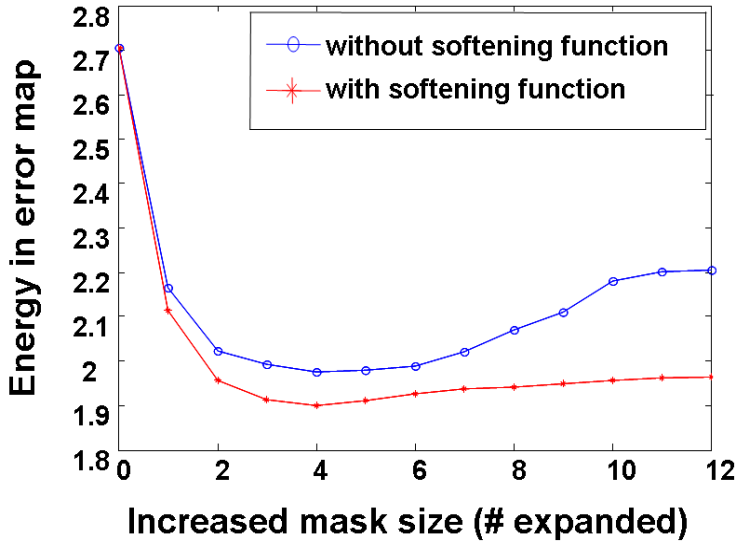

Figure 2-13 Error map energy within the ROI with respect to increased pixels of mask size. (blue) without and (red) with softening function. Butterworth function was used for softening function.

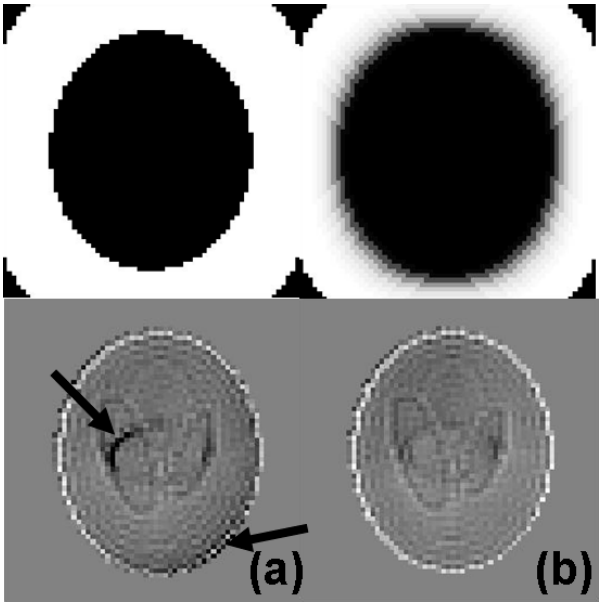

Figure 2-14 Effect of softening function. (top)Two types of softening functions; (a) Step and (b) Butterworth. (bottom) Error map within the ROI, mask size of 12

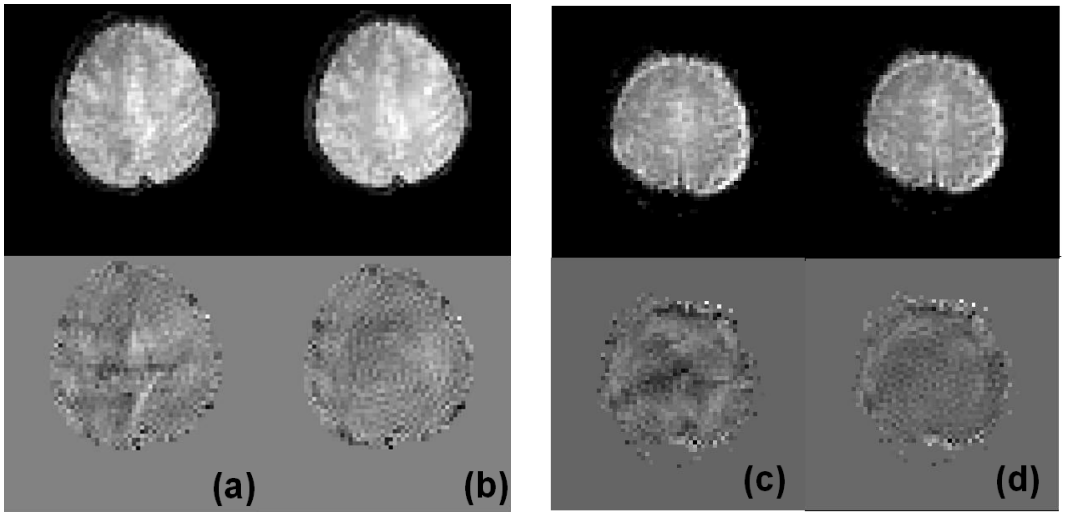

Figure 2-15 Human experiments from two different subjects. (top) SENSE images (a,c) without and (b,d) with softening function and (bottom) its corresponding error maps

2.3.5 Discussion and Conclusions

Our results show that choosing a moderate size of mask can improve the image quality and that smooth masks are effective in suppressing aliasing artifact. In our simulation, the tightest mask resulted in an edge effect caused by the overfitting of images around the edge which might be due to the roughness penalty in reconstruction process itself. This tightest mask also suffers from practical considerations related to difficulty in determining the exact edge with smooth sensitivity maps or with motion. The error map pattern also changes with respect to mask size: the bigger the mask size, the more aliasing artifact in the center of the object. As demonstrated in **Error! Reference source not found.**, the energy of the error map is the lowest at the mask size of 4 and is shown in Figure 2-12(c). Even though, as suggested in our theory, the smaller mask, the better, we would increase the mask size by several pixels to avoid any edge effect while still suppressing the aliasing artifact. This could also be a safer approach when dealing with human data with dynamic functional experiment where specified region of interest could be altered by subject's motion during the scan.

As we compare the Figure 2-12(d) and Figure 2-14, without and with using a softening function, respectively and also the image error plot shown in **Error! Reference source not found.**, smoothing the mask succeeds in reducing the aliasing artifacts at any mask size. We also found that among the softening functions, the Butterworth function is more desirable than any other functions, for a variety of mask sizes, possibly due to the rounded edges of this function.

CHAPTER 3. Optimizing parallel imaging for fMRI

Parallel imaging can be applied to fMRI to improve spatial resolution or to reduce image distortions by reducing the length of readouts. With higher field strength, the benefit of parallel imaging can be greatly increased, because parallel imaging enables us to reduce the length of readout, which suppresses image distortions accumulated from the field inhomogeneity, one of the biggest problems in high field imaging.

However, main drawback of applying parallel imaging is reduced SNR or aliasing artifact coming from undersampling. Properly selected parallel imaging method could lead us to better SNR or suppressed aliasing artifact, which in turn, enhances the use of parallel imaging in fMRI.

In this section, we attempt to optimize parallel imaging in fMRI. This includes finding an optimal updating method for calibration data, an optimal acquisition scheme, and an optimal initialization method in reconstruction process. For each section, several methods will be compared in terms of a number of activations, image domain error, temporal SNR, and reconstruction speed for some case.

3.1 Updating method for calibration data[1]

Our working hypothesis was that changes in the calibration data caused by subject motion and other temporal variations will lead to a preference for dynamic updating methods for calibration data in parallel imaging reconstruction. Our approach was to perform a quantitative comparison of several updating methods to determine the optimal updating methods for the two most widely used parallel imaging techniques, GRAPPA [12] and SENSE [7].

Since the calibration data are acquired during the actual scan for GRAPPA and SENSE, patient motion or system instability can produce temporal variation in the calibration data, i.e., GRAPPA coefficients and sensitivity maps. These temporal variations in calibration data over time suggested the need for updating the data, effectively adjusting those changes through the reconstruction process. Since the calibration data for GRAPPA and SENSE affect the images differently, it was necessary to investigate and distinguish the respective updating methods that would provide optimal result. GRAPPA coefficients are obtained by fitting each single component coil signal from composite signals that are composed of ACS's from all the coils. On the other hand, sensitivity map, which forms an unfolding matrix to reconstruct an unaliased image, are estimated either by prescanning or by self-calibration [7,14,57].

Although a variety of updating methods for the calibration data have been proposed for time series parallel imaging [24,25,69], there is, as of yet, no literature comparing the performance of these methods. Hence, we conducted quantitative comparisons of the

[1] This section is an extension of our work found in [70,71].

three most widely used updating methods, static (no updating), dynamic and dynamic sliding window techniques. The static (no updating) method should work best if the calibration data does not change over time, or if the estimated calibration data that are updated at each time point are too variable. On the other hand, the dynamic method should work better if the calibration data change over time or the updated estimation of each time point is very stable. The sliding window should work better than the single dynamic update method if the calibration data estimated from a single time point are not robust.

In our study, we applied the three updating methods to time series functional data using two dynamic parallel imaging techniques: TGRAPPA [24] and TSENSE [25], which were initially introduced for time-series cardiac MRI data. These methods allow for the simultaneous acquisition of the calibration data by alternating shots at each time point. These alternating acquisition techniques produce intensity variations that can be viewed as high temporal frequency components. In TSENSE, the UNFOLD method (UNaliasing by Fourier-encoding the Overlaps using the temporaL Dimension) [26] was used to remove the high temporal frequency components by temporal low-pass filtering. This temporal filtering was not applied in the original TGRAPPA method, but here, we did apply it to obtain a similar effect.

We used spiral trajectories, since they are more robust to motion and flow artifacts as well as very efficient in utilizing the gradient hardware and in rephasing signal loss due to magnetic susceptibility effects in fMRI [58-60], though they have some disadvantages in that the reconstruction process is more complex and suffers from image blur due to off-resonance effects, if left uncorrected. We have extended the GRAPPA and

SENSE methods to accommodate the spiral trajectories. Specifically, for spiral GRAPPA, we used a direct spiral GRAPPA method [21] proposed by Heidemann et al. in which the original spiral data are resampled onto a trajectory with constant angular velocity. For spiral SENSE, we used a method proposed by Sutton et al. [19] which uses an iterative time-segmented Non-Uniform Fast Fourier Transform (NUFFT) approach that compensates for field inhomogeneity effects.

3.1.1 Methods

We implemented spiral GRAPPA and spiral SENSE methods using existing techniques: a direct spiral GRAPPA [21] and iterative SENSE [19] with time-segmented field inhomogeneity correction [23]. In spiral GRAPPA, we used a computationally efficient conjugate phase (CP) method to correct for off-resonance, followed by a sum-of-squares image combination, whereas in spiral SENSE, we used an iterative conjugate gradient (CG) method, again with off-resonance corrections, to reconstruct the final image.

For our implementations, we optimized a variety of parameters. For example, for GRAPPA, we selected the number of angular groups and the number of neighbors for interpolation that lead to the smallest squared errors, and for SENSE, we selected a self-calibrated approach [57] and degrees of smoothing to estimate the sensitivity maps. For the iterative CG method for SENSE, the number of iterations was set to 17, based on our experience that for most images in our study, the normalized errors between previous iterations and current iterations were below 0.1% after 16th or 17th iterations. We also applied field map corrections using the time segmented approach [23].

To apply GRAPPA and SENSE to time series data, we implemented TGRAPPA and TSENSE. To reduce the high frequency variations from alternation of interleaves, we applied UNFOLD [26], temporal low-pass filtering, to both TGRAPPA and TSENSE. A low latency Butterworth filter, proposed by Kellman et el. [27] was used, of which the passband cut-off of 0.4, corresponding to 80% availability of the full frequency band, with a passband flatness of Rp = 1.5dB. The stopband edge frequency ranged over 24% of the frequency domain with rejection of Rs = 50dB.

We applied and compared three different schemes for updating calibration data: a static method that uses the calibration data from the first two time points for reconstruction of all time points, a dynamic method which uses the current time point and its nearest neighboring time point, and a sliding window technique which takes moving average of calibration data over a number of time points:

Method 1: *static - uses coefficients/maps from the first two shots only*

Method 2: *dynamic - updates coefficients/maps at each time point*

Method 3: *dynamic - updates coefficients/maps with a sliding window*

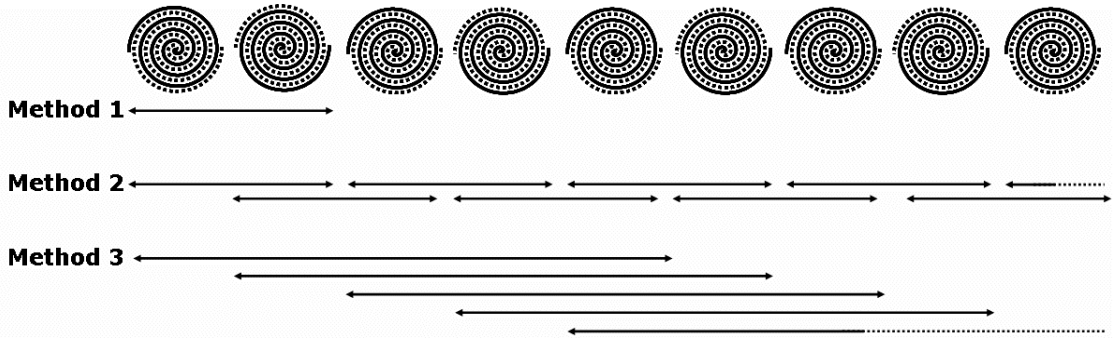

Figure 3-1 Three updating methods for calibration data and their respective time intervals for reduction factor R=2 with 2-shot spiral data. The arrow indicates where the calibration data are calculated.

These three methods are schematically described in Figure 3-1. Each arrow indicates a period of time from which the calibration data are acquired. Since we used 2-shot spirals with a reduction factor of R=2, the calibration data were calculated from 2 adjacent time frames. In Method 1, which is a static method, the calibration data were acquired from the first 2 time frames, and were used for all subsequent time points. In Method 2, the calibration data were acquired and updated every time frame. In Method 3, the calibration data were acquired at every time frame, as in Method 2, but a moving average of five sets of calibration data was used during the reconstruction process. Method 1 requires the least computational time, whereas Method 3 requires the most.

In-vivo human experiment and phantom experiment were conducted, without and with induced motion to see the effect of motion and physiological noise.

The results of the three updating techniques were compared in terms of the number of activated pixels, normalized RMS error in the image domain and TSNR. To calculate the number of activated pixels, we calculated the activation maps through the correlation coefficient with a sinusoidal reference waveform delayed by 4 seconds and thresholded at an uncorrected p value < 0.0002 (two-tailed). Normalized RMS error was calculated by taking the difference between reconstructed images from undersampled and fully-sampled k-space data in the image domain. In our analysis, two-shot k-space data from neighboring time points were used as fully-sampled data. The TSNR is a very important metric for fMRI studies because signal detection usually relies on detection of specific changes in the voxel time course, and is defined by a time course mean signal divided by the time course standard deviation [16]. Linear trends were removed prior to processing.

3.1.2 Experiments

We conducted an experiment to compare the performance of three methods for updating the calibration data. We collected functional data on a 3T GE scanner with an 8-channel array coil. Imaging parameters were TR = 2s for a single spiral, TE = 25ms, 64×64 matrix size, FOV = 22cm, 4-mm thick axial slices, total number of slices = 32, and two-shot gradient echo spiral-out acquisition. Seven healthy volunteers, each of whom gave informed consent under institutional review board (IRB) approval, were scanned. We used a simultaneous finger tapping task and reversing checker board visual stimulation, with a task cycle of (20s OFF / 20s ON) repeated 4 times. Thus, the paradigm produced a total of 40 time points for the fully sampled (2-shot) data, or 80 time points for the undersampled parallel imaging data with a reduction factor of 2.

We first compared the performance of the three updating methods in the absence of induced head motion. The subjects were asked not to move their heads during the acquisition. We reconstructed the undersampled data using GRAPPA and SENSE with the calibration data that were updated with each of the three schemes described before. We also conducted another experiment to evaluate the performance of the three updating schemes in the presence of randomly induced head movement during the acquisition. Using a motion apparatus, we generated the same series of random motions for all subjects, which produced 1~4 mm of translational motion and 0.5~1 degree of rotational motion. This apparatus consisted of a small air bladder that was filled and drained according to a prescribed schedule. The generated motion was uncorrelated with the task. Four variations of induced motion experiments were conducted at each functional run where we used the same paradigm and applied the same reconstruction methods as in the

previous experiment.

To correct for motion, we used MCFLIRT (Motion Correction using FMRIB's Linear Image Registration Tool) to the reconstructed images for both the non-motion and induced motion experiments [63].

For the non-motion experiment, we used a three-way ANOVA (analysis of variance) test to evaluate statistical significance among the three updating methods. The ANOVA test used updating methods, subjects and slices as group variables. The null hypothesis for our testing was that there was no such effect of using different updating methods on each metric. For the induced motion experiment, we used a four-way ANOVA, with four different kinds of motion being added as group variables. We set the significance level to be 0.01 and the test result with p-value below that level indicated rejecting the null hypothesis.

To account for temporal stability occurring with each subject, we also conducted a phantom experiment with an activation phantom to reinforce our conclusion. We implemented a phantom with a thin wire to which we applied electric current which distorts the magnetic field, thus mimicking the brain activation. The current was controlled by an ON/OFF switch during the activation phase with a cycle of (20s OFF / 20s ON) repeated 4 times as was used in the human experiment. We repeated our phantom experiment four times and imaging parameters were same as the human experiment.

3.1.3 Results

Figure 3-2 compares performance criteria for the three updating methods: static (Method 1), dynamic (Method 2) and sliding window (Method 3), shown for TGRAPPA (top) and TSENSE (bottom) when there is no induced motion with human subjects. For TGRAPPA, the dynamic updating method (Method 2) produced the best image quality, i.e., lowest image domain error, and the sliding window (Method 3) produced the largest number of activated pixel and the best TSNR performance. However, for TSENSE, the static updating method (Method 1) resulted in the largest number of activated pixels, the best TSNR and image quality. We have examined three adjacent slices containing motor cortex area and calculated three metrics from each slice for each subject. The numbers shown in the

Figure 3-2 are the averages of the numbers from each slice, since the metrics from three adjacent slices were highly correlated.

In the non-motion experiment, the different updating methods produced statistically different results in image domain error for TGRAPPA, and in all three metrics, i.e., the number of activated pixels, image domain error and TSNR, for TSENSE. These statistical results were obtained from a three-way ANOVA test. We marked the cases where statistically different results were produced with a star in the upper right hand corner of the respective figures.

Figure 3-3, on the other hand, shows results for experiment conducted with induced head motion and the three updating methods show similar trends as in the case without induced head motion, except for the number of activated pixels metric for TGRAPPA. Though the functional runs were independent of one another, each updating method had similar impact on each functional run. Thus, the numbers from four experiments and three slices were averaged altogether for each subject. Motion appears to degrade both image domain error and TSNR and also increases the variation across subjects.

For TGRAPPA, the smallest image domain error was obtained using the dynamic updating method (Method 2), and the best TSNR using the sliding window technique (Method 3). However, for TSENSE, the static updating method (Method 1) produced the largest number of activated pixels, the best image quality and the best TSNR, as was the case without induced motion.

In the motion experiment, for TGRAPPA, statistically different results for image domain error were produced by using different updating method. For TSENSE, statistically different results for the number of activated pixels and TSNR were produced by using different updating methods. These statistical analyses were conducted using a four-way ANOVA test. Again, we used a star mark on the upper right corner of the result figure where there is statistical impact in using different updating methods.

In both non-motion and motion experiments with human subjects, the results and the statistical analyses showed that the dynamic updating method resulted in the lowest image domain error for TGRAPPA, and the static updating method resulted in the largest number of activated pixels and the best TSNR for TSENSE.

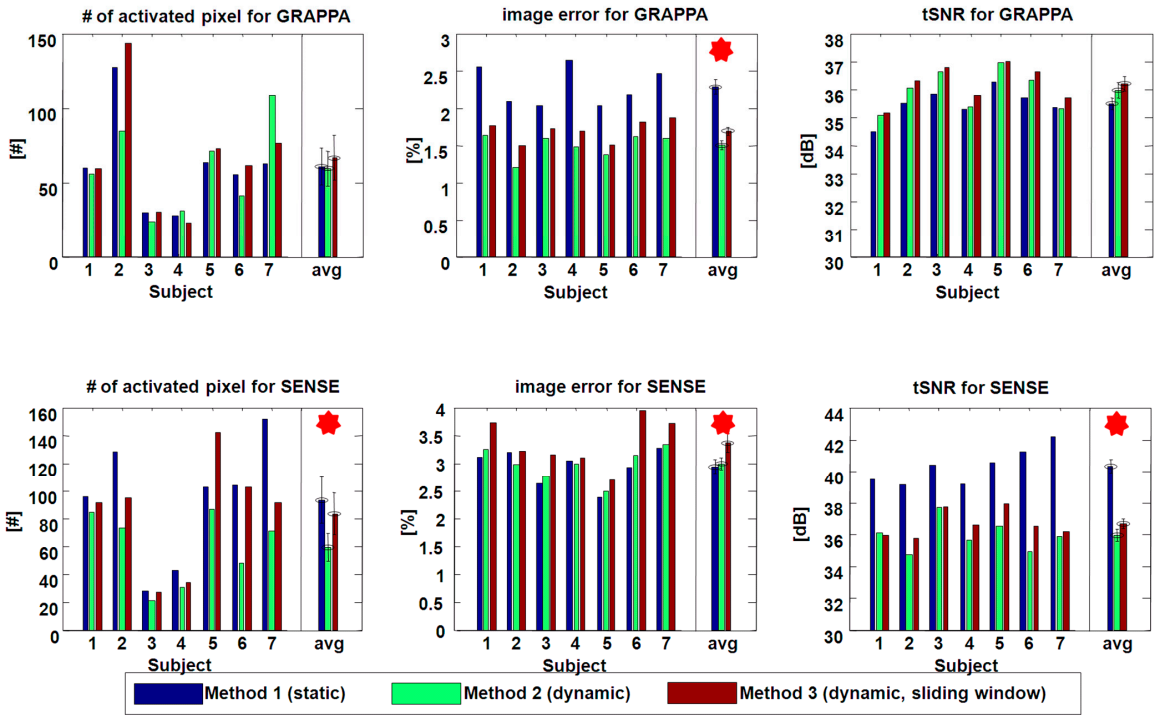

Figure 3-2 Comparison of the three updating methods (blue: Method 1, green: Method 2, red: Method 3) for the number of activated pixels, image domain error and TSNR in motor cortex slices for (top) TGRAPPA and (bottom) TSENSE reconstructions for data without intentional head motion. Stars indicate the case when p<0.01 (ANOVA test) for main effect of update methods.

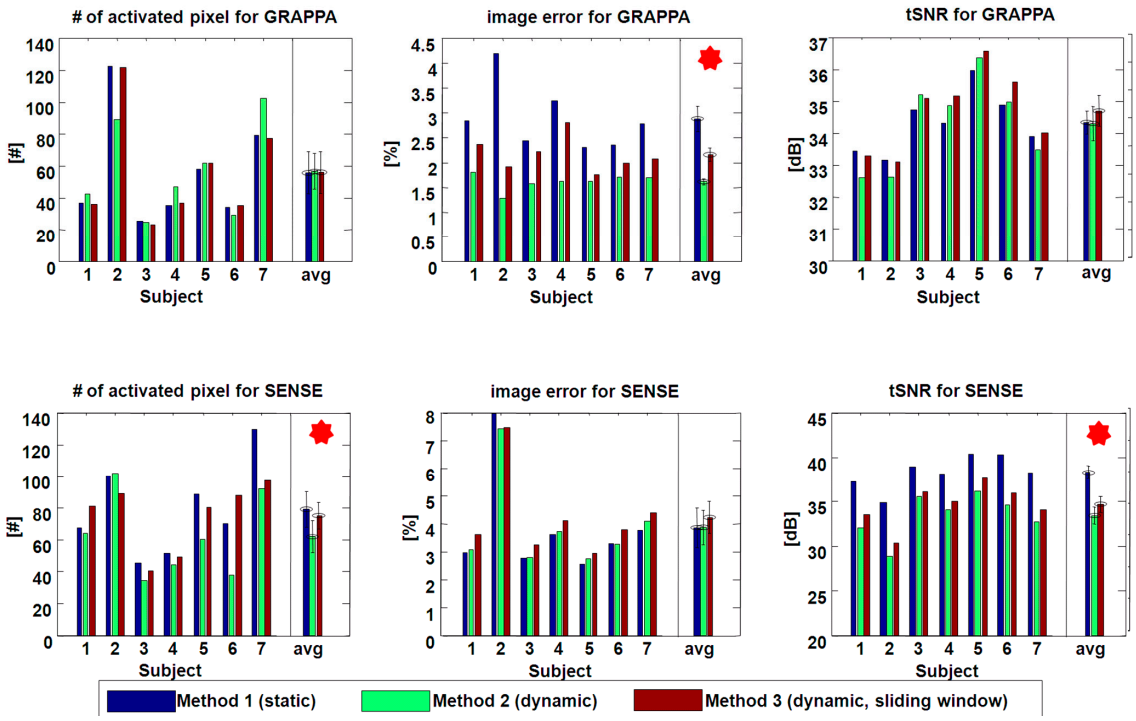

Figure 3-3 Comparison of image domain error and TSNR for the three updating methods in motor cortex slices for (top) TGRAPPA and (bottom) TSENSE reconstructions for data corrupted by motion. The trends of the three updating methods, in the case of motion, are comparable to those without intentional motion. Stars indicate the case when $p<0.01$ (ANOVA test) for main effect of update methods.

Figure 3-4 (a) shows the reconstructed image from the undersampled data (R=2) using TGRAPPA (top) and TSENSE (bottom), (b) the error maps after UNFOLD and (c-d) the TSNR map (c) before and (d) after UNFOLD. The error maps were calculated by taking the difference between images from the fully-sampled data and the undersampled data and they have been rescaled by a factor of 10 relative to the original images for better visualization. To see the effect of UNFOLD more clearly, we used the same image scale for TSNR map, before and after the UNFOLD filtering. The effect of UNFOLD filtering on voxel time course is also shown in Figure 3-5 where we can see some smoothing effect on time course.

Figure 3-6 shows voxel time-series data from the phantom experiments, after UNFOLD filtering.for the three updating methods for (a) TGRAPPA and (b) TSENSE. The time course using a sliding window reconstruction for fully-sampled two-shot data [72] are also shown. While not provided in detail here, the number of activated pixels, image domain error, and TSNR were also calculated for the phantom experiment. The phantom results corroborate significant findings from the human experiment, i.e., for TGRAPPA, the dynamic updating method (Method 2) and the sliding window approach (Method 3) have lower image domain error, and for TSENSE, the dynamic updating have the lowest number of activated pixels and TSNR whereas the static updating method produced best results for those metrics.

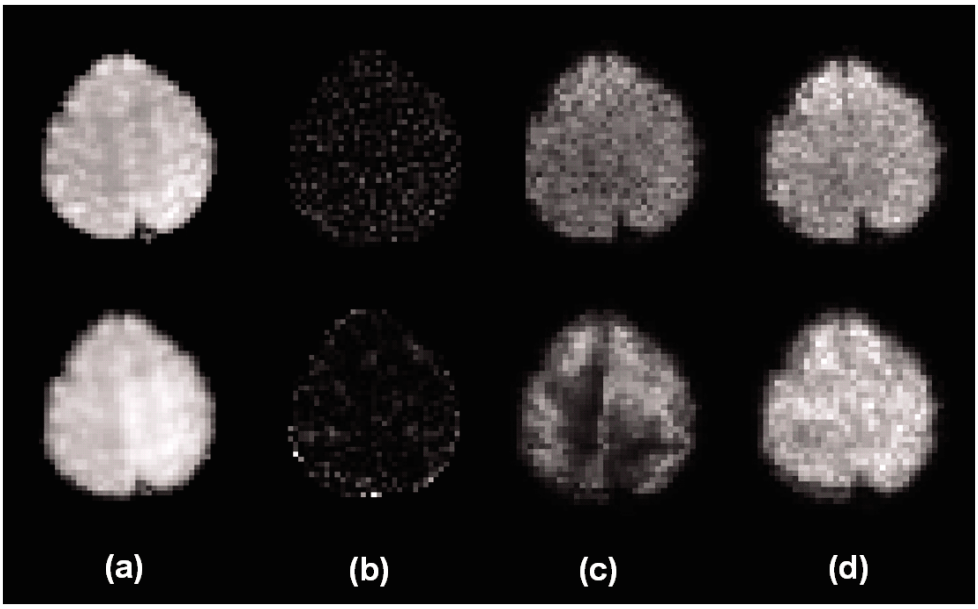

Figure 3-4 (top) TGRAPPA and (bottom) TSENSE (a) images reconstructed from undersampled data (R=2), (b) the error map (x 10) for a slice through the primary motor cortex, (c) TSNR map before UNFOLD and (d) after UNFOLD filtering.

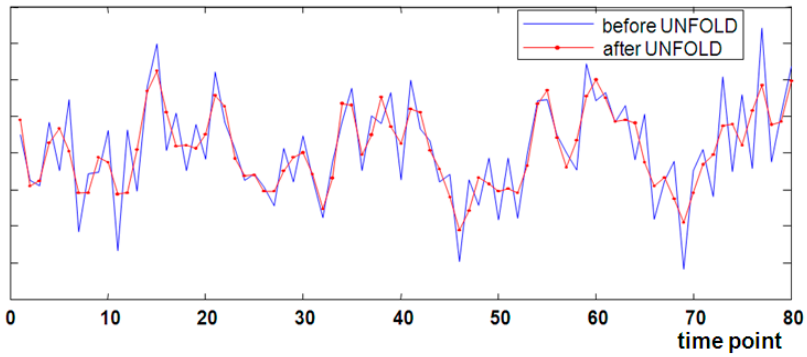

Figure 3-5 Voxel time course of one activated pixel acquired from the experiment from the previous section, before (solid) and after (solid with dots) UNFOLD. UNFOLD smoothes the time course. The pixel was selected from the image from the motor cortex slice where we conducted a finger tapping task 20sec (10 time points) OFF/ON, repeated 4 times

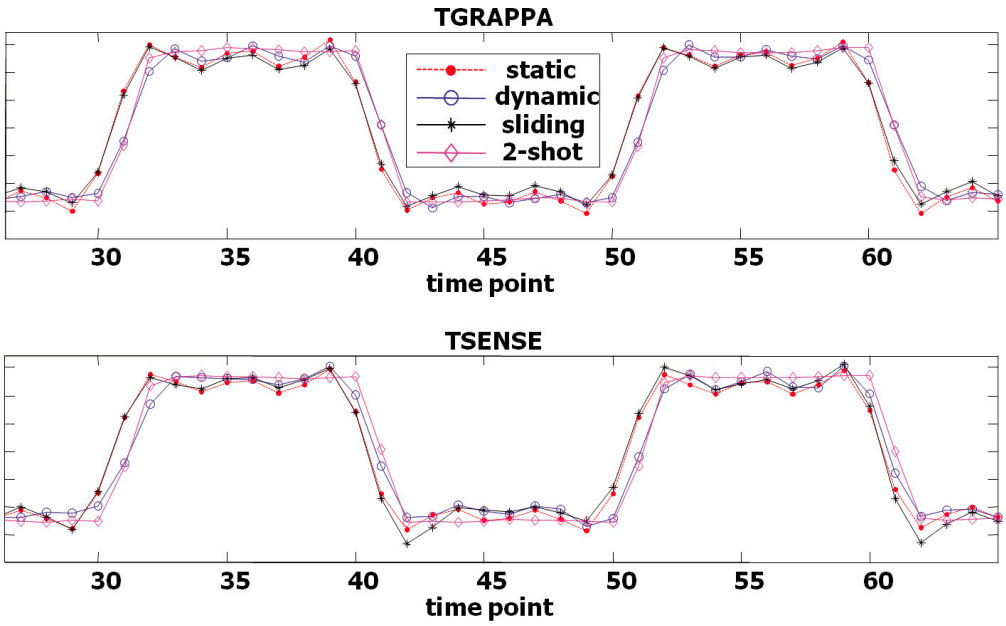

Figure 3-6 Voxel time course from phantom experiment using the three updating methods, and one reference from fully sampled data (2-shot). Blue: Method 1 (static), Black star: Method 2 (dynamic), Magenta diamond: Method 3 (sliding window), Red circle: 2-shot (reference).

3.1.4 Discussion

Our results suggest that applying different updating methods affects the performance of both TGRAPPA and TSENSE, possibly due to changes in the calibration data over time as is described in [62] where the temporal variability of sensitivity map is shown. We speculate that temporal variation of system instability or physiological noise as well as motion is the main source of temporal variation in calibration data that has affected the reconstruction even though estimation method was the same over the time course.

The human studies showed that, for TGRAPPA, the best image quality was produced by the dynamic updating method whereas the best TSNR was produced by the

sliding window technique, though this latter finding was not statistically significant. On the other hand, for TSENSE, the largest number of activated pixels, the lowest image domain error and the highest TSNR were produced by the static updating method. More interestingly, the induced motion study results showed trends similar to those above, despite the fact that motion degrades both image domain error and TSNR and increases the variance among the subjects for both performance criteria. Except as noted above, statistical analysis using ANOVA indicated that there were statistically significant differences for the human experiments, for both induced motion and non-motion cases. These results also confirm the findings of a preference for static sensitivity maps in echo-planar fMRI [35].

Our phantom experiment also examined the temporal behavior of each updating method in detail, which largely confirmed significant findings from the human data. One intriguing observation is that the voxel time course from the activation phantom, shown in Figure 3-6, demonstrated an increased lag of the response for the dynamic updating method compared to the other two updating methods. In particular, the dynamic updating method demonstrates temporal behavior very similar to a two-shot sliding window reconstruction. We suggest that this temporal behavior in both TGRAPPA and TSENSE is due to correlation between the calibration data and the imaging data (e.g., the missing shot) in the dynamic updating method (Method 2), which leads to the parallel imaging reconstruction to produce data very similar to two-shot fully sampled data.

It is reasonable to presume that the sensitivity map has to be updated to track changes of the sensitivity pattern over time. However, the dynamic updating method did not necessarily produce the best performance in image domain error, especially for

TSENSE. This unexpected finding may result from spatially dependent variation in the sensitivity maps over time [62], which then leads to variations in the reconstructed images. Another underlying cause for the increased variation is that when we form a full FOV unaliased image by combining the data from two shots to estimate sensitivity maps, there can be imaging artifact due to subject motion between the shots. Furthermore, there can be respiration-related phase variations which could also produce artifacts in the image domain and large variations between images [73] which, in turn, can further degrade the temporal stability of the sensitivity maps. Lastly, it is possible that the actual sensitivity map, which we have smoothed, may also be less object-dependent than we originally thought, which suggests that for TSENSE, the no updating (static method) is preferred. Use of the static updating method also requires the least processing time.

For TGRAPPA, on the other hand, it is better to update GRAPPA coefficients at each time point for better image quality with low image domain error. This may be because these coefficients are not spatially dependent parameter and are more insensitive to phase variations between the coils and shots. Moreover, the GRAPPA coefficients may also be more object dependent and thus, sensitive to bulk motion. Like TSENSE, the use of the dynamic update method (e.g. Method 2) can result in reduced temporal resolution as shown in Figure 3-6.

It was somewhat unexpected that different updating methods would be preferred for TGRAPPA and TSENSE. Though sensitivity maps and GRAPPA coefficients are considered to have roughly a Fourier Transform relationship to each other, that relationship is indirect. In particular, in other work, we found that there is spatial dependent variability in the sensitivity maps [62] whereas one expects GRAPPA

coefficients to have a spatially invariant behavior. Other differences in the temporal behavior of calibration data relate to differences in the process for estimation and applying this information. For example, for TGRAPPA, GRAPPA coefficients are different for the even and the odd shots, whereas for TSENSE, the sensitivity map can be exactly the same. This also affects how the moving average approach is implemented since only every other time point creates new information for TGRAPPA. Thus, even though sensitivity maps and GRAPPA coefficients are estimated at each time point, the details of how they are estimated and used are somewhat different. We believe that differences account for the differences in the desirability of particular updating approaches.

In Figure 3-4, TGRAPPA (top row) has a uniform error map over the image, which may be due to the k-space based reconstruction process. For TSENSE (bottom row), the TSNR map shows more spatial variation before the UNFOLD filtering. Applying UNFOLD improves the TSNR map and makes it more uniform. The result which shows the effect of UNFOLD, which removes only the highest temporal frequency components including the secondary artifacts induced by alternating shots from unsuppressed aliasing, conforms the findings of Madore [74,75]. For TSENSE, the use of static sensitivity map makes alternating shots unnecessary, except for calculation of the initial sensitivity maps. This would allow elimination of the UNFOLD filtering. Even though a further investigation is beyond the scope of this paper, we might predict that an undersampled single-shot SENSE approach might be a better solution for SENSE in fMRI, which is consistent with the findings in [35].

We made no attempt to compare TGRAPPA and TSENSE. While we tried to find

and apply optimal parameters for each reconstruction method, there are many variations and parameters which can lead to different conclusion of the comparison, such as selection method and SNR of ACS lines and implementation of GRAPPA coefficient, or regularization parameter for SENSE that governs the overall noise and resolution. However, propagation of errors in the image error map as well as intersubject variability seems to be consistent with other findings presented in the literatures [76,77].

In preparing our study, when optimizing the parameters involved in image reconstruction algorithms, we have made attempts to find optimal method for each case. We also examined effects of different implementations, such as different resolution and number of iterations or smoothness of sensitivity map, and have found the result to be generally consistent with our current findings. While it certainly is possible that a particular approach we did not try may lead to different conclusions, the approaches we have examined so far are consistent in both phantom and human studies.

We confine our conclusions primarily to spiral fMRI case, since in our application domain of fMRI focuses more on temporal stability than image clarity and reduced parallel imaging artifact, which might be more common concerns in cardiac imaging, and aliasing artifact that results from spiral parallel imaging is very different than that in Cartesian acquisitions.

3.1.5 Conclusions

In this study, our objective was to determine the optimal updating method for calibration data for time series fMRI data acquired with a reduced spiral acquisition using TGRAPPA and TSENSE. For TGRAPPA, the best image quality is achieved by applying

the dynamic update method of GRAPPA coefficients whereas for TSENSE, the largest number of activated pixels and best TSNR are achieved by applying the static sensitivity maps (no updating). This conclusion was confirmed by the statistical analysis. The findings in this study may be useful for those who are planning to apply dynamic parallel imaging methods to fMRI using spiral imaging.

3.2 Acquisition scheme for parallel imaging for fMRI: Comparison between undersampled single shot vs. multi-shot spiral-out sequences

Our study on TSENSE and of updating methods in the previous section has pointed us to use a static sensitivity map over dynamically updated approach. Since we discovered that static sensitivity map outperforms the dynamic updated sensitivity map which requires an interleaved acquisition, we reasoned that we can also apply a non-interleaving technique with static sensitivity map. Furthermore, UNFOLD temporal filtering is not necessary for non-interleaving acquisition scheme. In this section, we review some characteristics of TSENSE and of UNFOLD temporal filtering, and investigate whether a single-shot spiral sequence, which is a non-interleaving technique, could be a better solution for fMRI.

3.2.1. Introduction

TSENSE [25] was introduced to make efficient use of k-t space and avoid the extra scan required for estimating sensitivity map by using an interleaved acquisition scheme. In addition, sensitivity map can be estimated in self-calibrating manner and update dynamically to track changes during the scan due to object motion or other factors. This interleaved acquisition has shown to be favored for BOLD fMRI as much as single shot spiral for fully Fourier encoded data if motion correction and linear shim are properly conducted [78]. However, there has been concern about inconsistencies between each shot during the acquisition, which can result in increased artifacts due to phase or

amplitude errors, if not treated carefully. This inter-shot inconsistency problem still arises in parallel imaging when using an interleaved scheme such as TSENSE and TGRAPPA. UNFOLD temporal filtering, designed to remove residual aliasing artifact that are modulated to the temporal Nyquist frequency as shown in Figure 3-7, has also shown to mitigate this inter-shot variability problem.

When implementing UNFOLD low-pass temporal filter, we need to carefully design the filter in order to effectively filter out artifact from physiological noise and system instability as well as motion also at around high frequency region, yet not to lose valuable information at those higher temporal frequency regions [27]. More bandwidth can be used if the aliased component is relatively static and confined in narrow temporal frequency region and further, different filtering choices will likely affect ultimate performance.

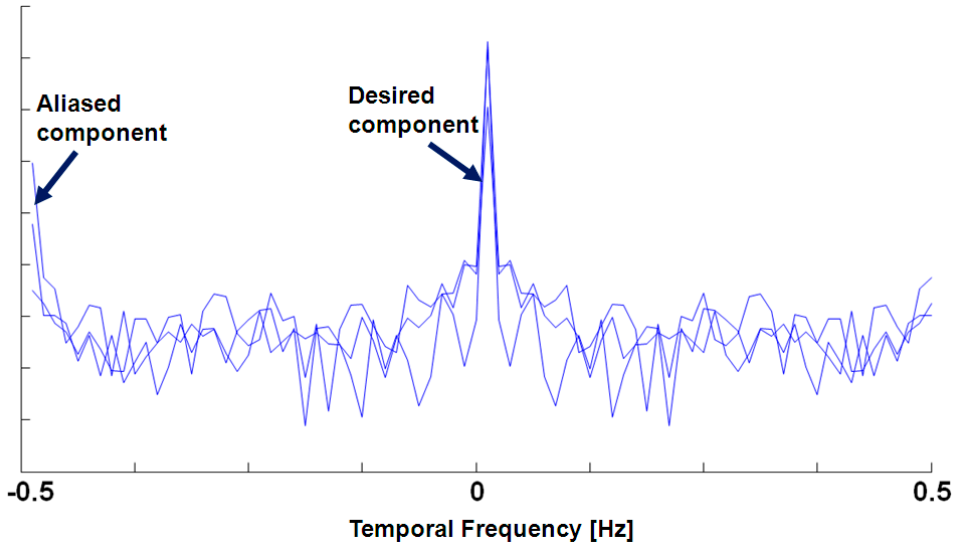

Figure 3-7 Temporal frequency spectrum of three representative voxels showing both desired and aliasing component. Temporal low pass filter was designed to cut off the aliasing component around the Nyquist (±0.5Hz) region.

Even though the use of UNFOLD temporal filtering on our TSENSE study has also shown to be effective in improving image quality as well as increasing number of activated pixels and TSNR, we also found out that UNFOLD temporal smoothing has a major drawback of an altered temporal impulse response. Depending on filter parameters, this can lead to smoothing, ringing [27] or both. Smoothing of the voxel time course, as shown in Figure 3-5, can lead to reduced temporal resolution or other artifacts.

Thus, given the potential issues with UNFOLD filtering and the desirability of using a static sensitivity map, we hypothesized that current interleaving acquisition such as TSENSE may not be optimal for a spiral functional MRI experiment, and that use of a single undersampled interleave might offer better performance. In the following, we investigate the performance for functional MRI of single-shot SENSE relative to TSENSE with the effect of UNFOLD temporal filtering.

3.2.2 Methods

In this experiment, we used the same functional experiment with TSENSE and single-shot SENSE, with spiral-out trajectory with a reduction factor of R=2. The same visual and motor tasks as well as non-motion and motion experiments were used as in Section 3.1. Imaging parameters were also the same as in Section 3.1 and the sequences for the experiments are shown in Figure 3-8. For single-shot SENSE, we also interleaved two shots at the beginning of the acquisition for sensitivity map calibration. For both TSENSE and SENSE, static sensitivity maps from the first two time points were used to reconstruct all time point images.

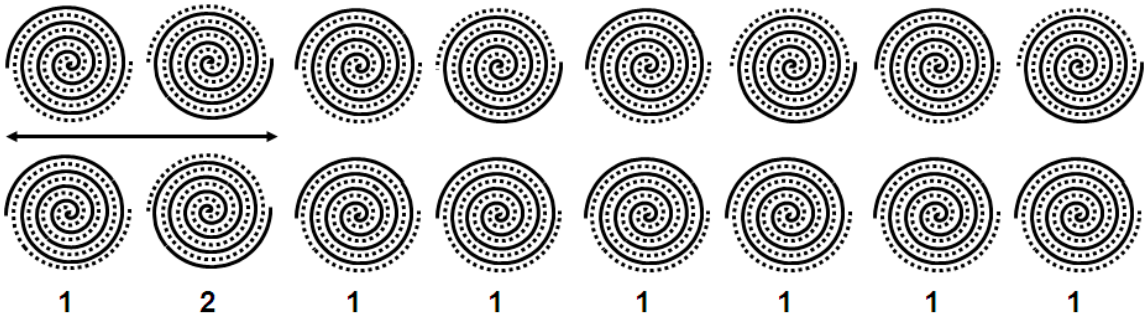

Figure 3-8 (Top) Two-shot (interleaved), and (bottom) single-shot spiral out sequence used in the experiment. For the single-shot, the first two time points are also interleaved for sensitivity map calibration. The arrow shows where static sensitivity map are calibrated for both cases. The number below shows the shot number used for acquisition, i.e., 1: first interleaf, 2: 2nd interleaf of 2-shot spiral.

3.2.3 Experimental Methods

The functional data were collected on a 3T GE scanner with an 8-channel array coil with imaging parameter: TR = 2s, TE = 25ms, 64×64 matrix size, FOV = 22cm, 5-mm thick axial slices, total number of slices = 30, and the reduction factor = 2. Total six healthy volunteers were given informed consent under institutional review board (IRB) approval and scanned. For functional experiment, we used a simultaneous finger tapping task and reversing checker board visual stimulation, with a task cycle of (20s OFF / 20s ON) repeated 4 times, which produced a total of 80 time points. We ran same functional study six times on each subject: three times with a two-shot sequence, three times with a single-shot sequence, one of three being without any induced motion, and two of three being with two different kinds of randomly induced head motion using a motion apparatus. Randomly induced motion was also uncorrelated with the task but reproducible among the subject and between each sequence.

The data were processed using a non-Cartesian SENSE with an iterative CG reconstruction algorithm using a static sensitivity map estimated from the first two time points. We then conducted motion correction using MCFLIRT (Motion Correction using FMRIB's Linear Image Registration Tool) [63] on both non-induced motion and induced motion experiments. UNFOLD low-pass temporal filtering was conducted on both two-shot and single-shot data order to examine the effect of UNFOLD temporal filtering on both cases to control for the effects of temporal smoothing, though it is not necessary for single-shot data. For TSNR, which is the time course mean signal divided by the time course standard deviation, linear trends were removed prior to processing.

For comparison between two different sequences, we used a two-way ANOVA (analysis of variance) test to evaluate statistical significance. The ANOVA test used type of sequence used and subjects as group variables. We set the significance level to be 0.01 and the test result with p-value below that level indicated rejecting the null hypothesis, indicating that there was no considerable difference.

3.2.4 Results

Comparisons between interleaved two-shot (TSENSE) and single-shot (SENSE) spiral sequences and also the effects of UNFOLD temporal filtering on both cases are shown in Figure 3-9 as (*left*) the number of activated pixels, (*middle*) image domain error and (*right*) TSNR, averaged from the data from six subjects. The 1,2,3 numbers in x-label denote the type of experiment we conducted: 1 for non motion experiment, and 2 and 3 for two different kinds of induced motion experiments, and n_l means the number of interleaves: n_l=2 for two-shot, n_l=1 for single shot.

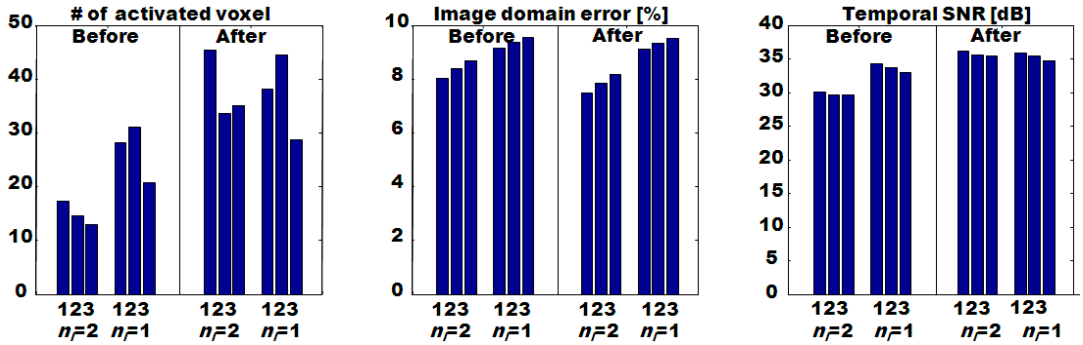

Figure 3-9 Average number of activated voxels (*left*), image domain error (*middle*) and TSNR (*right*) from 6 subjects for two-shot (n_I=2) and single-shot (n_I=1) undersampled spiral sequences, before and after UNFOLD from 1: No motion, 2: Motion 1, 3: Motion 2 experiment.

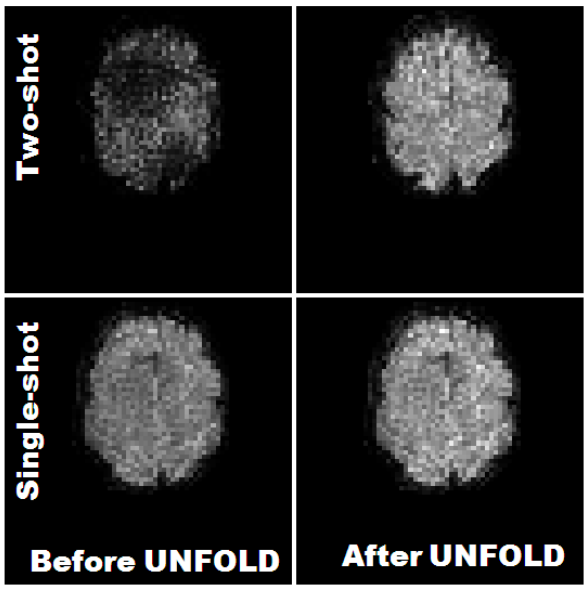

Figure 3-10 TSNR maps from one representative subject, (top) before and (bottom) after UNFOLD filtering with (a) two-shot and (b) single-shot data. For fair comparison, the values are shown on the same scale.

Table 3-1 P-values from the ANOVA test. P-value that are <0.01 are shaded. After UNFOLD filtering, difference between using two-shot and single-shot becomes negligible.

Before UNFOLD

		No Motion	Motion 1	Motion 2
# act pixel	sub	0.0260	0.0838	0.1543
	1vs2	0.0053	0.0052	0.0827
Image error	sub	0.5962	0.5984	0.2024
	1vs2	0.1073	0.1378	0.1384
TSNR	sub	0.2079	0.1030	0.0571
	1vs2	0.0002	0.0001	0.0006

After UNFOLD

		No Motion	Motion 1	Motion 2
# act pixel	sub	0.2556	0.0554	0.0947
	1vs2	0.4368	0.0979	0.3539
Image error	sub	0.5459	0.4708	0.1468
	1vs2	0.0356	0.0424	0.0414
TSNR	sub	0.1069	0.0391	0.0290
	1vs2	0.3091	0.6893	0.0846

Figure 3-10 demonstrates TSNR maps from one representative subject, (*top*) before and (*bottom*) after UNFOLD filtering with (a) two-shot and (b) single-shot data. For fair comparison, the values are shown on the same scale.

Two-way ANOVA tests were conducted with group variables, subject and different sequences (1 shot vs. 2 shots), before and after UNFOLD, to see the difference between two-shot and single-shot sequence. The resulting p-values are shown in Table 3-1. The shaded regions indicate when two-shot and single shot are significantly different in statistical sense.

3.2.5 Discussion

For the two-shot sequence (TSENSE), the effect of UNFOLD filtering is much greater than that of single-shot sequence, since aliasing components were shifted to the temporal edges and removed by temporal filtering.

As we have hypothesized before, UNFOLD was not very effective for single-shot SENSE in reducing image domain error or TSNR for single-shot, when compared to that of two-shot sequence. Before UNFOLD, single-shot sequence is superior to two-shot for the number of activated pixels and TSNR. However, after UNFOLD filtering, they become comparable to each other.

3.2.6 Conclusions

We demonstrated that in terms of overall fMRI performance, single-shot spiral SENSE and two-shot spiral TSENSE, both with UNFOLD filtering, are comparable to each other. However, for fMRI, where the temporal resolution is an important factor, temporal low pass filtering that smoothes the voxel time course should be avoided, or at least should be carefully designed. Furthermore, before processing UNFOLD temporal filtering, the performance of single-shot SENSE exceeds that of TSENSE. Therefore, we propose to use single-shot spiral, which does not necessary require UNFOLD temporal filtering, over TSENSE when applying parallel imaging in fMRI.

3.3 Advanced initialization method for accelerating image reconstruction of fMRI data

Iterative algorithms for reconstructing non-Cartesian SENSE suffer from long computation time, which is a major reason that hinders people from using non-Cartesian trajectories over Cartesian trajectories despite its desirable characteristics such as motion and flow robustness as well as efficient gradient hardware utilization. This prolonged computation time becomes even more problematic when dealing with multiple time series fMRI data. For example, when reconstructing 64×64 images of 80 time points from 8-channel array coil and R=2 acceleration, using 17 of iterations, the computation times is about 24 minutes for iterative SENSE with Matlab on a 2GHz Pentium workstation, even using fast NUFFT algorithm [79]. Without further optimization or faster computational hardware, this compute would preclude it use for real time processing.

We hypothesize that for time series fMRI data, computation time could be reduced by applying proper initialization that exploits a priori information from previous time points. Thus, in this section, we describe a simple, yet powerful method for initializing the iterative reconstruction algorithm for non-Cartesian SENSE to achieve faster convergence.

3.3.1 Introduction

In solving the non-Cartesian SENSE image reconstruction problem in MRI, our purpose is to find an image, f, from the sampled k-space data, y, from the equation,

$$y = Af + \varepsilon \tag{3.1}$$

where A is the system matrix which contains information on k-space trajectory, fieldmap, and sensitivity map for SENSE. Since the dominant noise of MRI signal is known to be additive white Gaussian, this system equation is being solved by minimizing a cost function,

$$\Psi(f) = \frac{1}{2}\|y - Af\|^2 + \beta R(f) \tag{3.2}$$

where $R(f)$ is a regularization function.

One of the most efficient and widely used methods to solve this minimization problem for non-Cartesian SENSE is the conjugate gradient approach, which is applied in our studies of iterative SENSE. The Conjugate Gradient (CG) method is a powerful minimization tool and the basic idea of this CG method is to ensure the step to be taken into the non-interfering direction. In other words, CG method ensures the step which was previously taken in a certain way is never taken again. This is done by constructing the search directions by conjugation of the residuals, which is orthogonal to the previous search direction [80].

The number of iterations can be reduced by choosing a good initialization point, i.e., starting at the point which is closer to the solution, or by preconditioning which improves the condition number of a problem.

Preconditioning accelerates the algorithm by approximating the system equation into

a more suitable form with smaller condition number. A density compensation function has been proposed as a preconditioner [22], but has shown to have SNR penalty in the reconstructed images [81]. Circulant preconditioner has been proposed and shown to be successful for accelerating iterative reconstruction process of tomographic imaging [82,83], but no conclusive result has been reported to be successful for MRI [84].

Besides preconditioning, setting a starting image with a good approximation can reduce the number of iterations. For our iterative SENSE reconstruction, an initialization with a zero image, followed by a density-compensated conjugate phase image was previously used [79]. Other initialization approaches such as using a localized sensitivity map with a reduced aliasing pattern [85] or using a low resolution [86] have been proposed, especially for iterative SENSE reconstruction. However, for dynamic parallel imaging, we can assume that the images reconstructed at each time point are similar to each other and share similar convergence point, especially for fMRI where there usually is less object movement than in cardiac imaging. We hypothesized that using the final converged value of the image from the previous time point as an initial point for reconstructing the image at next time point can reduce the number of iterations needed

3.3.2 Methods

We conducted a simulation experiment with an undersampling factor of 2. We also simulated an activation, 10 time points OFF/ON repeated 4 times, which causes %2 change of maximum intensity at the middle of the image. Image was reconstructed using an initial estimate from the reconstructed image of the previous time point. To see the effect and robustness to motion which might occur during the scan, we generated a

motion to the simulation object; when at 6th time point, the object was shifted 5 pixels to the right from the previous time point and moved back to the original location at 7th time point. Images were initialized with previous time point image except for the image at first time point which was initialized with zeros.

To evaluate the method with human data, we also conducted a functional imaging study using 4 subjects. Data were acquired with single-shot spiral out sequence at the reduction factor of 2 and the total number of time points was 80.

3.3.3 Results

The convergence of image reconstruction for simulation is shown in Figure 3-11, as a normalized RMS error, calculated as the difference from previous iteration. The corresponding activation map at 3rd, 4th, and 5th iterations, overlaid onto the anatomical image are also shown. The red square denotes where the true activation was simulated and is expected to occur. The algorithm converges between 5th and 6th iterations, and produces a reasonable amount of activation.

Error convergence plot for each time point, before, during and after the motion is generated, is shown in Figure 3-12. Convergence plot of images at 5th through 9th time point, when at 6th time point, the object was shifted 5 pixels to the right from the previous time point and moved back to the original location at 7th time point. Each image was initialized with the image from the previous time point. The algorithm converges even with motion, but object motion still has a large impact on the convergence of reconstruction especially at the time point where the motion occurs and also at the following time point. Compared to non-motion case, 5 more iterations, i.e., total 10

iterations, were required for the object that moved 5-pixels from the previous iteration to converge, and 10 more iterations, i.e., total 15 iterations, were required for the object that came back at the original location at the following time point to converge.

The in-vivo human functional experiment were also conducted on 4 subjects and the reconstructed images at (a) 5th time point, (b) 40th time point, and (c) 80th time points using the image from the previous time point as an initial estimate are shown in Figure 3-13 with 5 number of iterations. However, the error appears to grow as for later time points. To test whether the increasing error is from not enough number of iterations, we also increased the number of iterations up to 17 while still initializing the image from the previous time point and the result is shown in Figure 3-14. Reference images were initialized with zeros and error maps from images initialized with the previous time point images are also shown. When we increased the number of iterations, the error appears to grow even more as for later time points.

TSNR were calculated from the data from all 4 subjects and are plotted in Figure 3-15. X-label, 0 denotes the case when we reconstructed images using zeros as an initial estimate, whereas 1~15 denotes the case when we started image reconstruction with previous time point as an initial estimate and algorithm stopped at 1^{st}, 2^{nd}, 5^{th}, 10^{th} and 15^{th} iterations, respectively. There are only minimal improvements in the TSNR after the 5^{th} iteration with a value about 1.3dB smaller than that of case starting with zeros as an initial image.

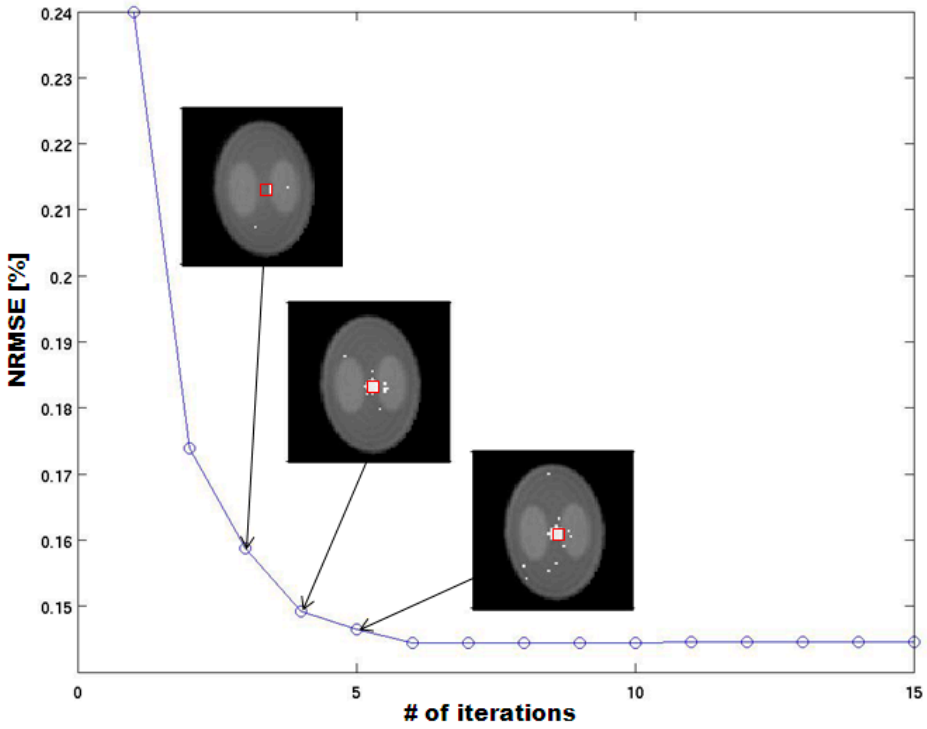

Figure 3-11 Simulation Result. Convergence of algorithm (normalized RMS error between each iteration) with corresponding activation map at 3rd, 4th, and 5th iterations, overlaid onto the anatomical image.

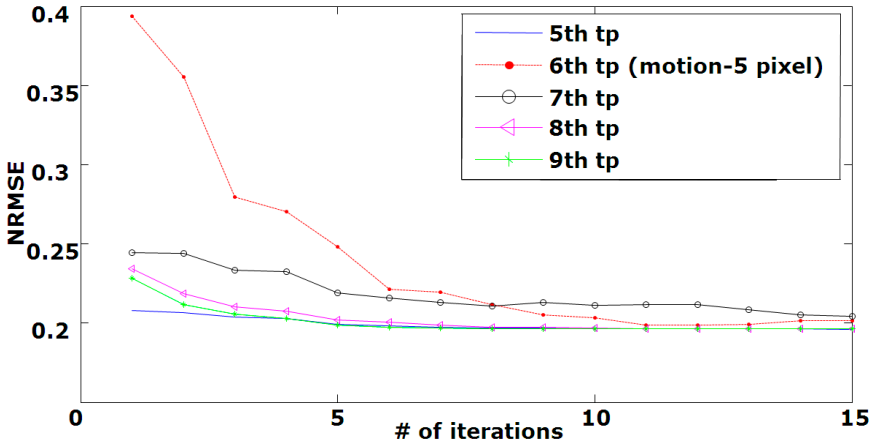

Figure 3-12 Impact of initialization method on motion-corrupted data. Convergence plot of images at 5th through 9th time point, when at 6th time point, the object was shifted 5 pixels to the right from the previous time point and moved back to the original location at 7th time point. Image was initialized with previous time point image. Algorithm converges even with motion, but object motion still has much impact on the convergence of reconstruction especially at the time point where the motion occurs and also at the following time point.

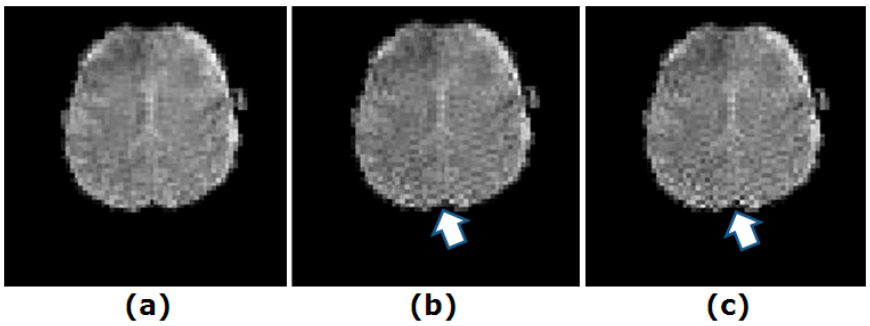

Figure 3-13 Images at (a) 5-th time point, (b) 40-th time point, and (c) 80-th time point, reconstructed using initialization from previous time point and using 5 number of iterations. Images that were reconstructed from initialization using the previous time point image seem to produce larger errors as at later time points.

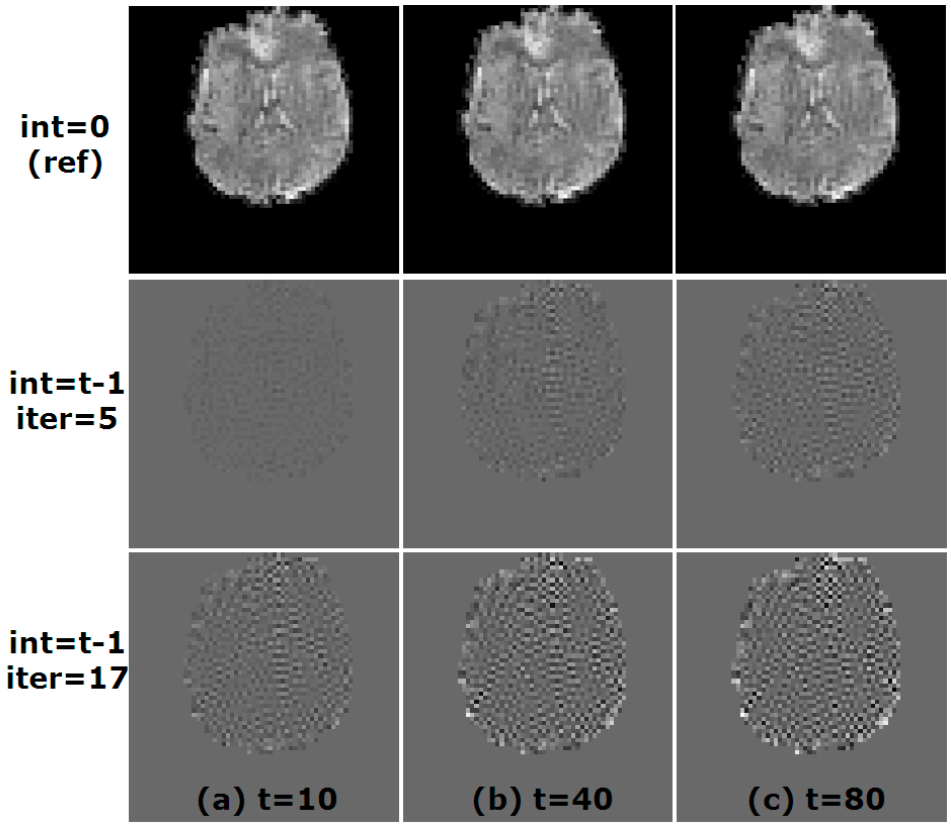

Figure 3-14 (top) Reference images and (middle, bottom) error maps at (a) 10, (b) 40 and (c) 80 time points. (top) Reference images were initialized with zeros and error maps were from images initialized with the previous time point images and stopped at (middle) 5th and (bottom) 17th iteration.

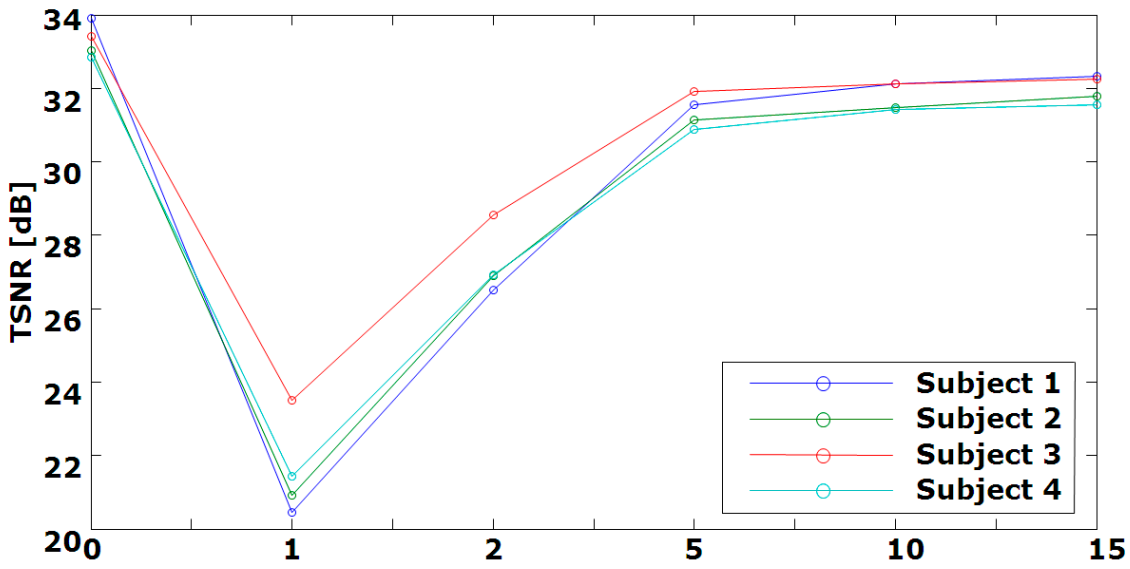

Figure 3-15 TSNR of human experiment. 0: starting with zeros as an initial estimate, 1~15: starting with previous time point as an initial estimate, where the algorithm stops at 1st, 2nd, 5th, 10th and 15th iterations. TSNR after 5th iteration is about 1.3dB smaller than that of starting with zeros.

3.3.4 Discussion

We tested initialization with a reconstructed image from the previous time point. Our simulation results have shown that the proposed initialization method has converged at around 5th iteration, achieving 3-fold acceleration (15 iterations reduced to 5 iterations) of iterative algorithm, and have shown to maintain reasonable localization and the number of brain activations. However, as we can see from the human experiment, image error tends to grow and TSNR has been reduced when using this initialization scheme. The activation maps for the human experiments have not been presented due to lack of consistent results amongst the subjects. The total number of activated pixels tends to decrease, but mostly to only a slight extent after 5th iteration.

We suspected from the simulation result that the motion could be a determining factor that hinders our initialization method from working, since error tends to grow from the previous time point, if not using enough number of iterations. However, our human results show that this is not always the case, possibly due to the suboptimal condition from using undersampled data, physiological noise that results in phase variations, as well as system instability. Further investigation of those effects is the scope of our future study.

3.3.5 Conclusions

Initializing with previous time point on time series fMRI data led us to achieve 3-fold acceleration in convergence rate. In simulation studies, the algorithm also seemed to be robust to motion, though the number of iterations required for convergence is increased. However, for *in-vivo* human experiment, the image domain error was added as we reconstruct images towards the end of time point. We also lost TSNR by 1.3dB by accelerating the reconstruction time by 3 times, possibly due to the suboptimal condition from using undersampled data and ill-conditioning of system matrix.

Temporal stability as well as image error are trade-offs vs. computation time. Though we focused on spiral undersampled data, we believe the conclusion of our initialization method can be transferred to reconstruction of image from fully-sampled data, or any other non-Cartesian data which requires iterative reconstruction algorithm.

CHAPTER 4. Development of a new reconstruction algorithm for parallel imaging: SENSE without acquiring a sensitivity map

In the previous sections, we focused on improving and analyzing current parallel image reconstruction algorithms, mostly for SENSE. Image reconstruction for SENSE is preceded by estimation process of calibration data, i.e., sensitivity map, and additional scan or careful selection of reference map and/or denoising process is required for the process. Sensitivity maps are known to be not only coil dependent but also object dependent [87], particularly at high magnetic fields, and thus, they are required to be calculated for each scan. There are substantial challenges to sensitivity map estimation in the presence of motion or physiological noise.. Moreover, the effects of measurement and estimation error can further degrade the sensitivity maps. Thus there still remains possibility for inaccuracies in the estimated sensitivity map which can produce errors in the reconstructed images.

We propose a joint estimation method that eliminates the need for the sensitivity map estimation process for every scan. Our hypothesis is that, there is a "global" low resolution, non-object dependent sensitivity pattern for each coil configuration which works, at least “roughly”, for any object. Then, we can use this global sensitivity map for

initial value to reconstruct image without additional calibration step for sensitivity map which could be achieved by using a joint estimation method. The proposed joint estimation method updates sensitivity map during the reconstruction process and has shown to be robust when a good global initial sensitivity map is obtained.

4.1 Joint Estimation of image and coil sensitivity map via iterative conjugate gradient algorithm for spiral MRI

4.1.1 Introduction

The performance of SENSitivity Encoding (SENSE) [7,22] highly depends on the sensitivity map estimation, since the sensitivity maps are a major component the system model in the parallel image reconstruction process. Sensitivity maps can be estimated either by self-calibrated approach or by reference scan such as using body coil.

However, whether using the prescanning method or self-calibrating approach, estimating sensitivity maps requires an additional process and there are various factors that can lead to inaccuracies in this sensitivity map estimations, such as image misregistration between body coil and surface coil, or between the reference scan and actual scan due to patient motion. Since the accuracy of sensitivity map has a direct bearing on the performance of SENSE, i.e., any inaccuracy in the sensitivity map produces errors in the reconstructed images, the estimation step [7,18,55,56,61,62,88,89] or post correction [50] needs to be carefully taken which could make SENSE even more complicated.

When the system matrix for SENSE becomes ill-conditioned, such as in the case of higher reduction factors, the effect of inaccuracy in the sensitivity map becomes more problematic. A number of attempts have been made for improving accuracy in the sensitivity map estimation using polynomial fitting [7] or thin-plate splines [88], followed by denoising process, and using wavelet denoising process [56,89], etc. However, we could also improve sensitivity map estimation by incorporating the estimation during the image reconstruction process. In this case, rather than relying upon a prior estimate of sensitivity map, we propose jointly estimate the image and the sensitivity map.

The concept of the joint estimation methods of image and sensitivity map have recently been proposed for Cartesian [90,91] and for spiral [92] trajectories, and have shown promising results. These methods use an iterative conjugate gradient (CG) algorithm using a penalized weighted least squares (PWLS) cost function and alternates between updating the polynomial coefficients of sensitivity map and the image. This method does not require regularization of sensitivity map, because the polynomial fitting inherently assumes sensitivity map to be smooth.

We propose using a novel sensitivity map estimation technique which not only controls smoothness but also noise via regularization. This method allows a pixel-by-pixel estimation of sensitivity map for each coil, thus allows more degrees of freedom for controlling regional smoothness through the roughness penalty term. We also propose adding a constraining term between the updating processes which then could be useful in suppressing the divergence of the artifact during the reconstruction process as well as in controlling the overall energy in the image for consistency in the data.

Our another aim is to eliminate the need for the sensitivity map acquisition for every

scan by using a global sensitivity map defined for each coil and then by applying a joint estimation technique which refines the sensitivity map for each subject and constantly updates the maps during the image reconstruction process. A global sensitivity map can be estimated from a homogeneous object with low resolution estimation. The proposed method uses a novel sensitivity map estimation technique that controls noise and smoothness via quadratic regularization in pixel-by-pixel approach, with an energy constraint between sensitivity map estimation and image reconstruction.

In the following sections, we will review joint estimation method using polynomial fitting [92] and present our joint estimation with a regularized sensitivity map approach. We first simulate various conditions where joint estimation can be preferred in practical situation. We also apply a global sensitivity map to our novel joint estimation method. The result of our joint estimation method will also be presented for simulation and human fMRI data and will be compared with the polynomial fitting approach [92] and a conventional non-joint estimation approach [22]. The results will be shown in terms of image quality and the error convergence.

4.1.2 Theory

Conventional non-Cartesian SENSE reconstructs unaliased image through iterative CG algorithm. Assuming 1D for simplicity and reduced acquisition for parallel imaging, we start from signal equation for MRI,

$$s_l(t) = \int c_l(r) f(r) e^{-i2\pi \vec{k}\cdot\vec{r}} dr \tag{4.1}$$

where r denotes the space coordinates, k denotes the k-space trajectory, $s_l(t)$ denotes the undersampled k-space data from l-th receiver coil, $c_l(t)$ denotes the sensitivity pattern of

l-th coil, and *f*(*r*) denotes the image to be reconstructed. Then we acquire the noisy k-space data:

$$y_l = s_l(t) + \varepsilon \tag{4.2}$$

which can also be written as

$$y_l \approx \sum c_l(r) f(r) e^{-i2\pi k \cdot r} + \varepsilon \tag{4.3}$$

where in matrix form,

$$\mathbf{y}_l = \mathbf{A}\,\mathrm{diag}\{\mathbf{c}_l\}\mathbf{f} + \boldsymbol{\varepsilon} \tag{4.4}$$

The conventional approach solves this equation iteratively by minimizing the following cost function,

$$\Psi(\mathbf{f}) = \sum_{l=1}^{L} \left\| \mathbf{y}_l - \mathbf{A}\,\mathrm{diag}\{\mathbf{c}_l\}\mathbf{f} \right\| + \beta_0 R_0(\mathbf{f}) \tag{4.5}$$

where $R_0(\mathbf{f})$ denotes the regularization term. This is usually of a quadratic term, $R_0(\mathbf{f}) = \frac{1}{2}\|\mathbf{C}\mathbf{f}\|^2$, where $\mathbf{C}$ is the matrix that takes differences among the neighboring pixels in the image. β_0 denotes the smoothness parameter for the regularization term.

However, joint estimation not only estimates the image through the abovementioned process, but also it estimates the sensitivity maps by minimizing,

$$\Psi(\mathbf{c}) = \sum_{l=1}^{L} \left\| \mathbf{y}_l - \mathbf{A}\,\mathrm{diag}\{\mathbf{f}\}\mathbf{c}_l \right\| + \beta R(\mathbf{c}_l) \tag{4.6}$$

where the last $\beta R(\mathbf{c}_l)$ term is omitted for the polynomial fitting approach, since the approach inherently assumes the sensitivity map to be smooth. In this polynomial fitting approach, we can model the sensitivity map as [90]:

$$s_l(r) = \sum_{i=0}^{N} \sum_{j=0}^{N} a_{l,i,j} x^i y^j \tag{4.7}$$

where $r = (x, y)$ is the spatial coordinate for the sensitivity map and $a_{l,i,j}$ is the coefficient of an N-th order of polynomial. Our regularized sensitivity map approach makes use of the last term of equation (4.6), $\beta R(\mathbf{c}_l)$, but with the β value, usually bigger than β_0 since in general, sensitivity maps are smoother than the image.

Both the two joint estimation processes, just like conventional approach, start with the initial value of sensitivity map, usually acquired from the body coil image (prescanning) or low resolution, sum-of-squares, geometric mean of each coil image (self-calibration). However, we can also start with a non-object dependent, global sensitivity map, acquired with a homogeneous object at low resolution which mostly contains information on coil sensitivity pattern for the coil configuration through which any additional acquiring process for coils sensitivity map could be excluded.

Joint estimation methods, either the polynomial fitting approach or our regularized approach, differ from the conventional approach in that they do update the system matrix by updating the sensitivity map. This is done by alternating the sensitivity map estimation process and image reconstruction process. We update the system matrix of image reconstruction process by updating the sensitivity map estimated from the last iteration step of the sensitivity map estimation algorithm. Between the image and sensitivity map estimation process, we rescale the image, which is the input of sensitivity map estimation process, by constraining the energy in order not for the scaling factor to affect the system matrix. This process is schematically shown in Figure 4-1.

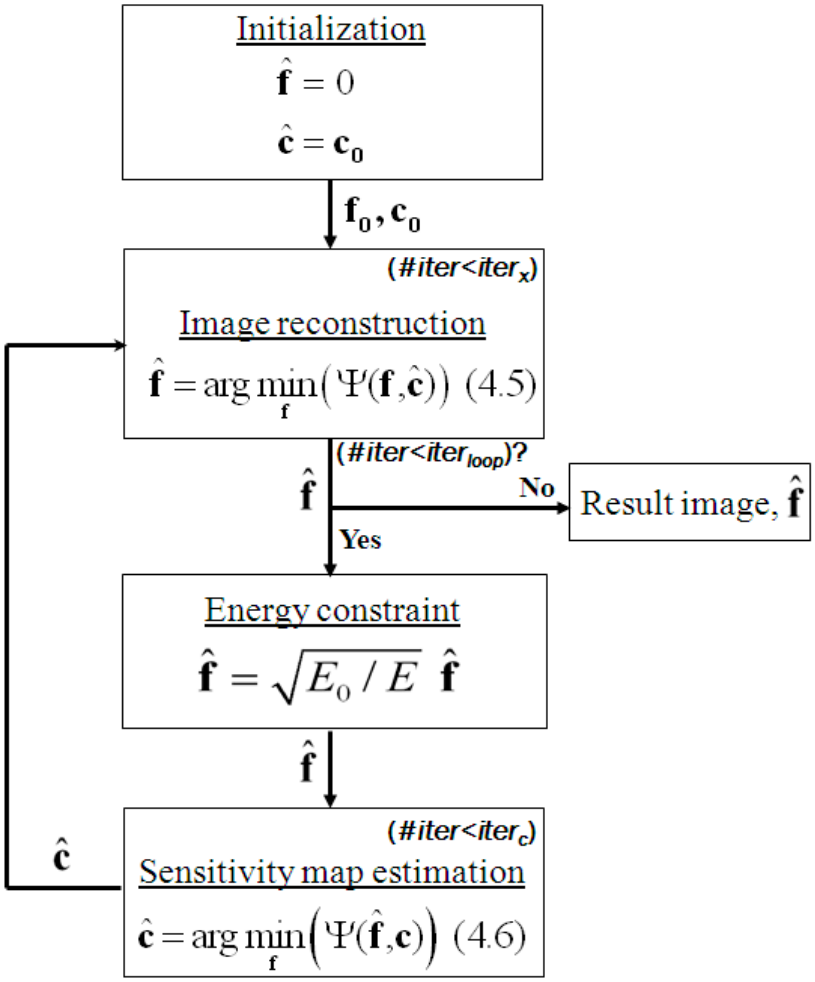

Figure 4-1 Joint estimation using quadratic regularization with an energy constraint.

For joint estimation using polynomial fitting approach, polynomial coefficients, $a_{l,i,j}$, are estimated instead of sensitivity map. In Figure 4-1, $iter_x$, and $iter_c$ denote the number of iteration of CG loop for image reconstruction, sensitivity map estimation, respectively, whereas $iter_{loop}$ denote entire loop of alternating between image and sensitivity map estimation process.

4.1.3 Experiments

We first test the performance of this joint estimation approach in various circumstances where the system matrix could become ill-conditioned. Our proposed method was compared with polynomial joint estimation using simulation data. Conditions include scanning at high reduction factor, high off-resonance frequencies and white Gaussian noise added to the initially estimated sensitivity map.

For simulation data, small amount of noise was added and sensitivity map that was used to generate the original measurement was used to reconstruct images, unless otherwise stated. Fieldmap was corrected using time-segmented approach [79], and the reduction factor was 2 except for the simulation experiment on the reduction factor and we used a two-shot undersampled spiral trajectory. One out of two-shots was used to reconstruct the image and the two-shot, fully-sampled image was used for the reference image for calculating NRMS errors in the image.

For joint estimation methods, sensitivity map was updated three times at every 7^{th} iteration. The reference image for calculating the NRMS errors was generated from the fully-sampled images.

4.1.4 Results

Figure 4-2 shows [71] the simulation result when additive white Gaussian noise (AWGN) is added to the initial sensitivity map. The top row shows reconstructed images from using (a) conventional, (b) joint estimation with regularized sensitivity and (c) joint estimation with polynomial fitting approach when the noise was added to the initial sensitivity map with an SNR of 10dB. Corresponding error maps are also shown at the bottom row. For joint regularized and joint polynomial approach, 1/4 of the error maps have been rescaled for better presentation. The plot in the bottom shows normalized root mean squared error convergence plot for SNR=10dB and SNR=20dB cases using the three methods above. Both joint regularized and joint polynomial fitting approaches converges and are comparable to each other, whereas conventional approach diverges and leads to corrupted images as shown in (a).

Figure 4-3 shows simulation result for the effect of a number of reduction factors on joint estimation. For this simulation, the data was generated by generating multi-shot spiral data, from 2-shots to 8-shots, for reduction factor from R=2 to R=8, respectively, and then images were reconstructed by using only one of the shots. Representative images when using a reduction factor R=6 with a (a) regularized and (b) polynomial fitting approach are shown in the top and corresponding errormaps are shown in the bottom of each Figure (a) and (b) where 1/4 portion of error map has been rescaled for better presentation. Figure 4-3 (c) shows NRMS error plot with respect to the reduction factor of 2 through 8 for using (dot) regularized and (circle) polynomial fitting approach.

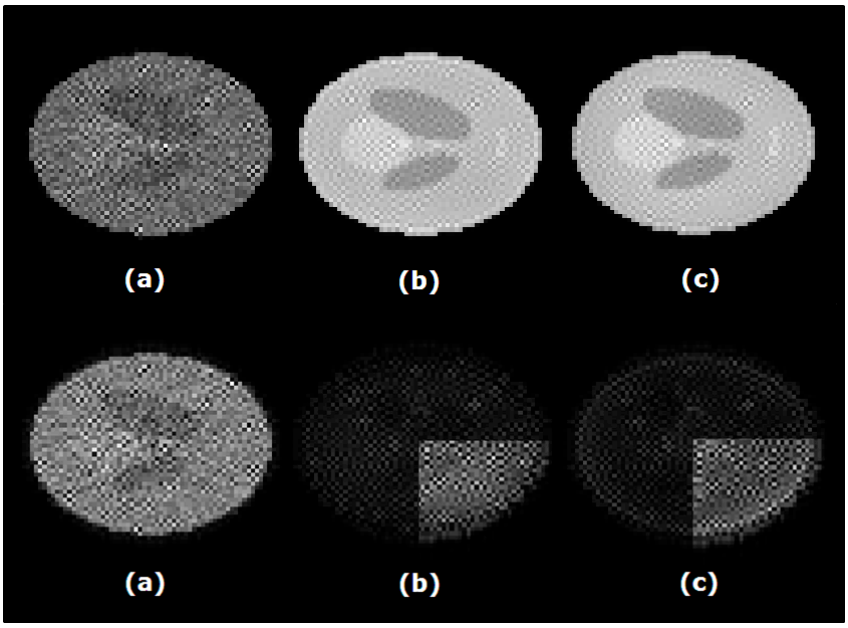

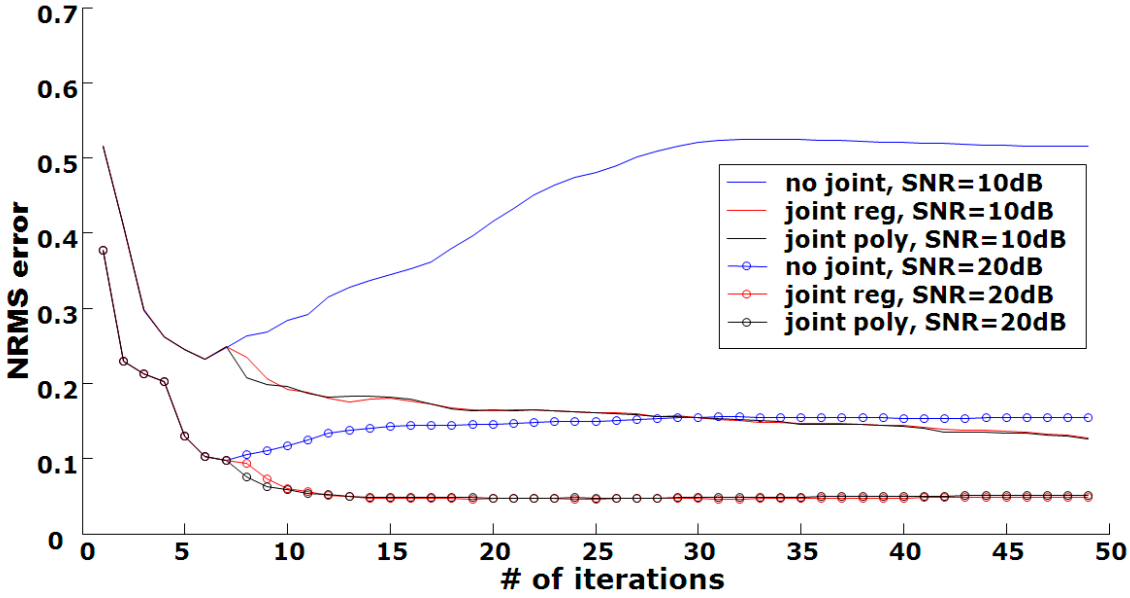

Figure 4-2 When WGN is added to initial sensitivity map (~10dB). (top) image reconstructed from using (a) conventional, (b) joint estimation with regularized sensitivity and (c) joint estimation with polynomial fitting approach, and its (middle) corresponding error maps for SNR=10dB in same gray scale. For joint regularized and joint polynomial approach, 1/4 of the error maps have been rescaled for better presentation. (bottom) NRMSE convergence plot for SNR=10dB and SNR=20dB. Both joint regularized and joint polynomial fitting approaches converges and are comparable to each other, whereas conventional approach diverges and leads to corrupted images as shown in (a)

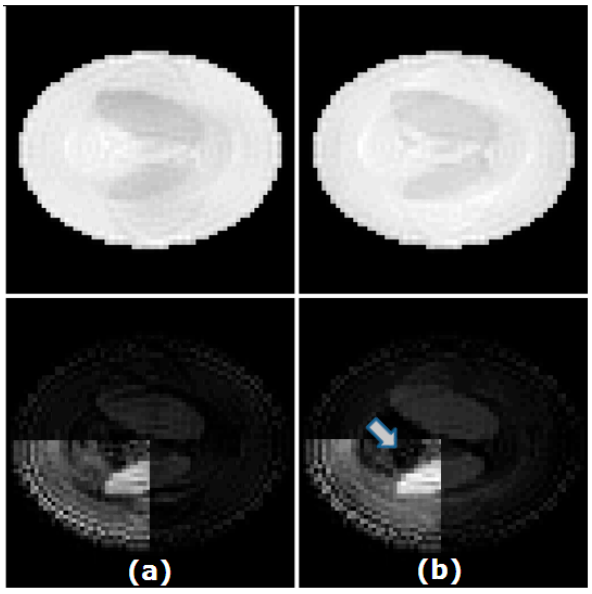

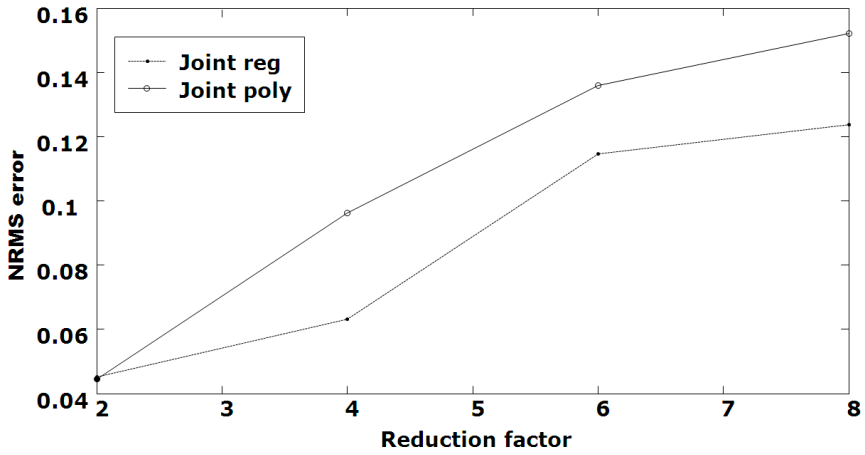

(c)

Figure 4-3 The effect of reduction factor, R=2,4,6,8 when using 8 number of coils. (a,b) Representative image when a reduction factor R=6 was used. (top) reconstructed SENSE images by (a) joint regularized and (b) joint polynomial approach, and (bottom) corresponding error maps. 1/4 portion of error map has been rescaled for better presentation. (c) NRMS error plot w.r.t. reduction factor 2 through 8 for using (red dot) joint regularized and (black circle) joint polynomial fitting approach.

Figure 4-4 and Figure 4-5 shows the effect of field inhomogeneity on two joint estimation methods. In Figure 4-4, simulation results are shown. The simulated fieldmap is shown on the left and the range was 287Hz. SENSE reconstructed images from joint estimation using (a) the regularized, (b) the polynomial fitting approach, and (c) the error convergence plot are also shown. Joint estimation using the regularized approach produced less error in the image in the presence of large field inhomogeneity.

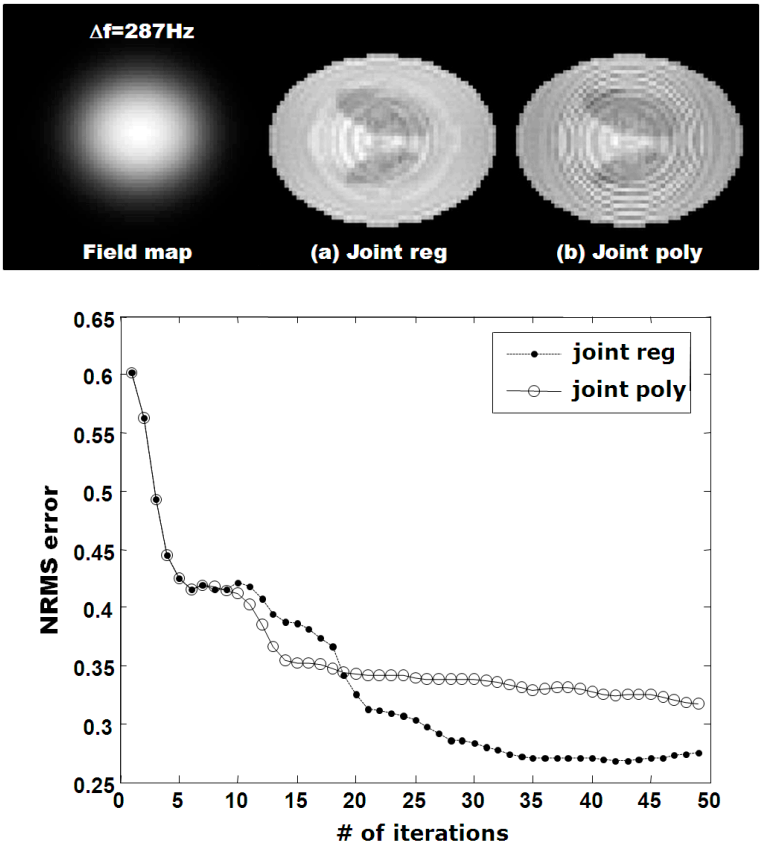

(c)

Figure 4-4 Effect of field map on two joint estimation methods. (left) Simulated fieldmap as well as (a,b) reconstructed images from joint estimation using (a) regularized sensitivity and (b) polynomial fitting approach, and (c) error convergence plot are shown. Joint estimation using regularized sensitivity approach produces less error in the image in the presence of large field inhomogeneity.

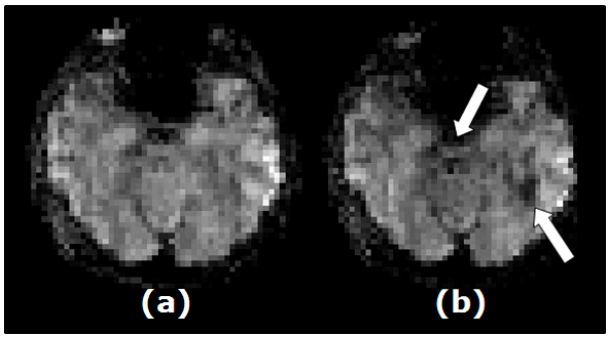

Figure 4-5 Reconstruction of *in-vivo* human data slices containing visual cortex, using joint estimation with (a) the regularized and (b) the polynomial fitting sensitivity map estimation approach. The polyfit approach experiences more artifact as shown in the white arrow.

Figure 4-5 shows an example from the *in-vivo* human data for the slice containing visual cortex. Joint estimation methods with the regularized approach and the polynomial fitting method are compared. The initial sensitivity map was estimated using a self-calibrated geometric mean approach. The joint estimation with polynomial fitting approach experiences more artifacts as shown in the white arrow.

We also test joint estimation with a global sensitivity map with in-vivo human data. For global sensitivity map, a homogeneous object with a wide coverage was scanned and the sensitivity map was then estimated from a self-calibrated approach using 2^{nd} order polynomial fitting method. Then, this global sensitivity map, shown in Figure 4-6, was used as an initial value for the joint estimation.

The human result images using the global sensitivity map are shown in Figure 4-7 for all 30 slices, where (a) shows result of the joint estimation using 3^{rd} order polynomial fitting approach and (b) shows that of the proposed regularized approach. The sensitivity

map was updated after every seventh iteration and the algorithm stopped after 28 iterations. Figure 4-8 (1st and 2nd row) also shows *in-vivo* human results using the global sensitivity map. The images from two different *in-vivo* human data using (top row) joint estimation with polynomial approach, (middle row) joint estimation with regularized sensitivity map approach, and (bottom row) conventional SENSE without joint estimation are shown. Three representative slices were chosen. The joint estimation with polynomial fitting approach seems to perform better with the slices where the object occupies a larger fraction of the field of view whereas regularized approach seems to perform better at inferior slices with a more irregular object with large field inhomogeneity.

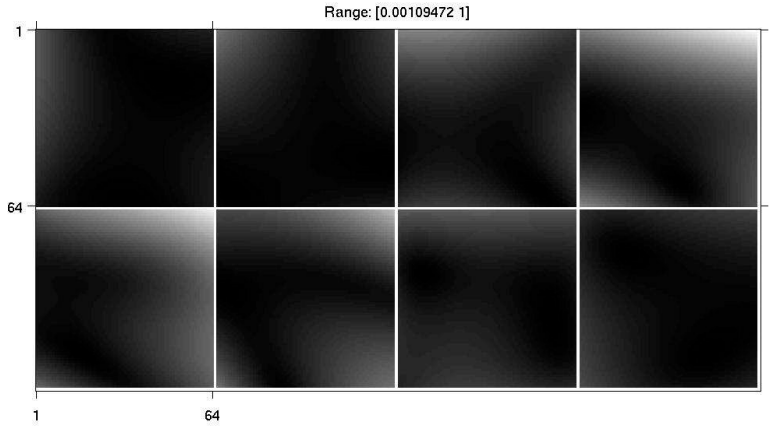

Figure 4-6 Initial sensitivity map from different subject at different slice. Using 2nd order polynomial fitting approach.

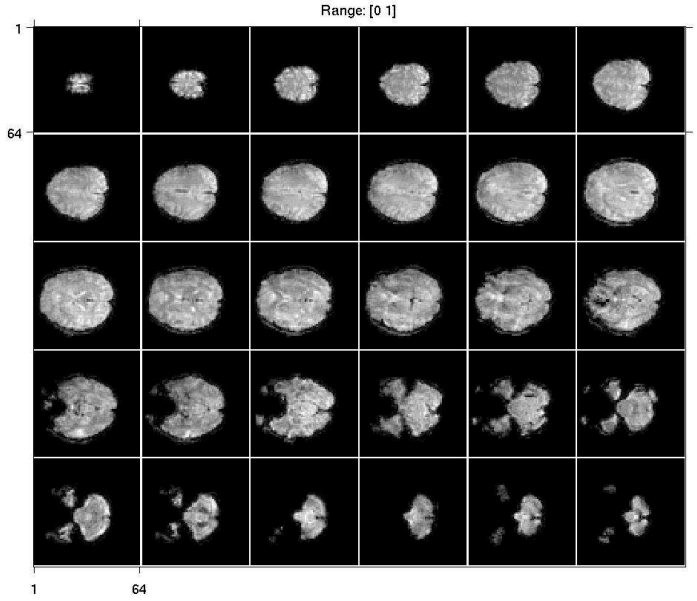

(a)

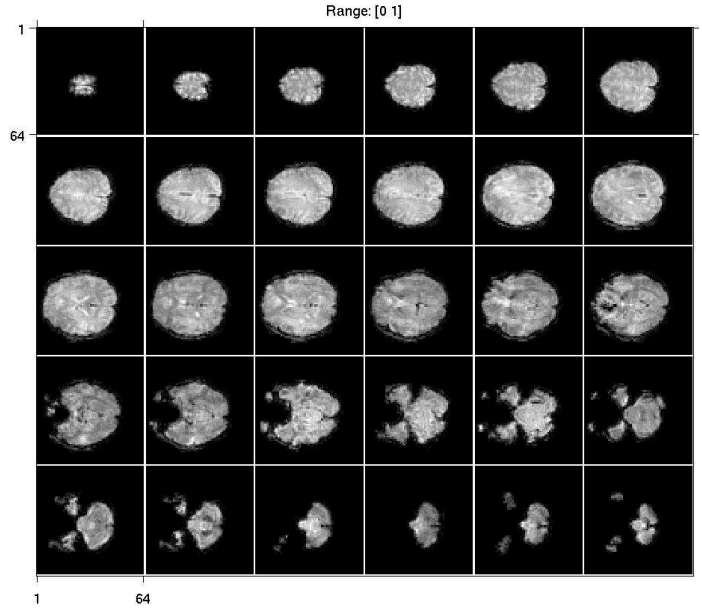

(b)

Figure 4-7 When a global sensitivity map from Figure 4-6 is used as an initial value for sensitivity map. 30 slices image from joint estimation method using (a) 3rd order polynomial fitting approach and (b) proposed regularization approach.

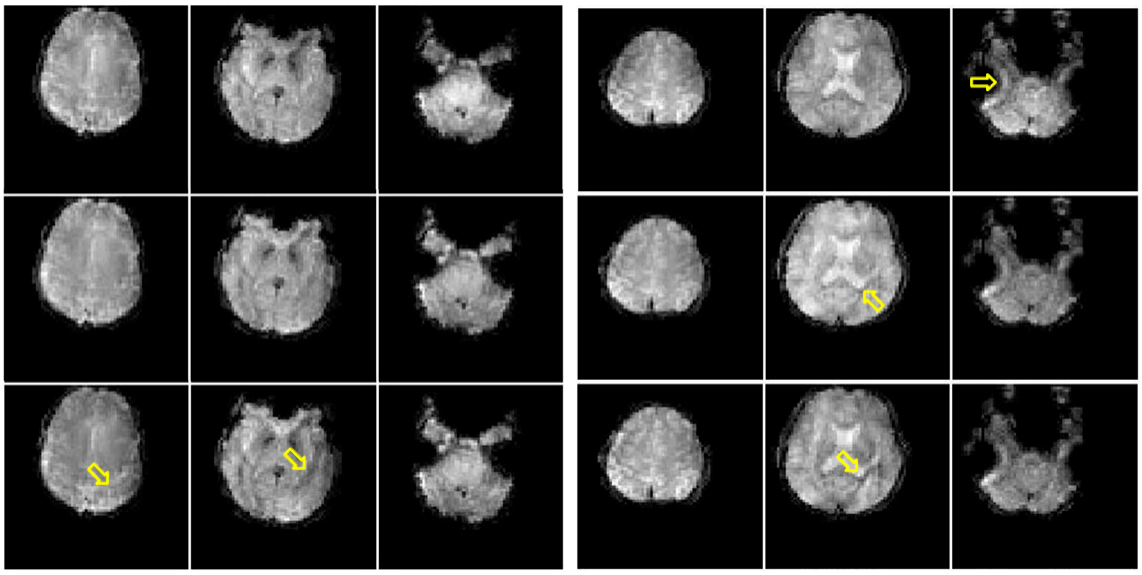

Figure 4-8 (1st row) Joint estimation with polynomial fitting, (2nd row) joint estimation with regularized sensitivity map, and (3rd row) conventional SENSE images of two different *in-vivo* human data using a global sensitivity map. Three representative slices were chosen. Joint estimation with polynomial fitting approach seems to perform better with larger object whereas regularized approach seems to perform better at inferior slices, agreeable to the simulation result.

4.1.5 Discussion and Conclusions

Simulation results using joint estimation methods have demonstrated that there are improvements in image quality for cases where the initial sensitivity maps are noisy or are corrupted by motion and misregistration. Using a regularized sensitivity map with the joint estimation method was shown to work better than polynomial fitting approach for higher reduction factors and in the presence of large magnetic field inhomogeneity. This latter point was also confirmed from *in-vivo* human data, for more inferior slices, for example, the slice containing the visual cortex area.

When implementing the regularized joint estimation method, care should be taken in tuning the regularization (smoothness) parameter as well as initialization since our experience has shown that this method is much more sensitive to the initialization than the polynomial fitting approach. The sensitivity to initialization is likely to due to large number of unknowns, relative to the polynomial approach, and the borderline conditioning of the reconstruction problem. Thus, while the regularized method produced better results in the aforementioned cases with simulations and *in-vivo* human data, if the regularization parameters are not correctly tuned, polynomial fitting process could be more robust in other various situations where the system could become more ill-conditioned.

While the regularized method is very sensitive to the initialization, we have found that a global sensitivity map (object independent) was sufficiently good initialization for good reconstruction quality. Using this approach, it is possible to implement SENSE reconstruction using joint estimation approach without the need to acquire a sensitivity map for each subject.

Our in vivo human experiment with initializing with a good low-resolution global sensitivity map has demonstrated the feasibility of this approach under practical conditions. The object dependent aspects of the sensitivity map are then estimated during the joint estimation process.

CHAPTER 5. Conclusions and Future work

We focused on improving and optimizing non-Cartesian parallel image reconstruction methods for time series functional magnetic resonance imaging (fMRI) to create truly effective solutions for current problems of interest, such as reducing image distortions from field inhomogeneity and improving spatial and temporal resolutions.

Among the parallel imaging methods, we focused on SENSitivity Encoding (SENSE) and GeneRalized Autocalibrating Partially Parallel Acquisitions (GRAPPA), the two most commonly used, appied to spiral k-space trajectories, with dynamic extensions, TGRAPPA and TSENSE, respectively.

Specifically, our research was aimed at improving or developing reconstruction algorithms, optimizing parallel imaging method for fMRI data and developing a new joint estimation method for image and sensitivity map.

In Chapter 2, we improved the reconstruction algorithm of non-Cartesian SENSE, optimized for time series functional data. To optimize the reconstruction process, we focused on improving sensitivity map estimation by investigating various self-calibrating sensitivity map estimation methods as well as analyzing the effect of spatial and temporal smoothing of sensitivity map through regularization.

In Section 2.1, we compared four self-calibrated sensitivity map estimation methods,

geometric mean, sum-of-squares, generalized mean with p=1, i.e., arithmetic mean, and harmonic mean approach. We demonstrated that the geometric mean and harmonic mean methods that produced a homogeneous profile of reference map, resulting in a high quality image reconstruction for SENSE for both simulation and human data. Thus, we propose using a geometric mean or harmonic mean approach over widely-accepted sum-of-squares approach. The process of acquiring reference map data and processing is very simple and this could be done in few seconds. Our future work will include obtaining quantitative criteria for measuring the flatness of reference map profiles and measuring the accuracy of SENSE reconstruction with in-vivo human images.

In Section 2.2, we investigated the effect of spatial and temporal smoothing on the sensitivity map and we found out that appropriate spatial smoothing reduces image domain error and increases the TSNR whereas, for temporal smoothing, the more temporal average we take, the greater the improvement on both performance criteria, though we limit this conclusion to fMRI data since the sliding window technique has been shown to be of limited benefit in cardiac imaging. In future studies, we will investigate how to choose smoothness parameter and number of moving averages to have a good estimate of sensitivity map.

In Section 2.3, we demonstrated that the regions of support (mask size) does have impact on the image quality and usually, a moderate mask size extending several pixels beyond the object produces the optimal image quality. We also found that using a soft mask with smoother mask edges, i.e., the Butterworth function, resulted in less the aliasing artifact.

In Chapter 3, we investigated several approaches for optimizing parallel imaging in

fMRI which includes finding an optimal updating method for calibration data for parallel imaging, such as sensitivity map or GRAPPA coefficients, analyzing acquisition schemes by comparing interleaved TSENSE with single shot undersampled SENSE, and investigating an initialization method in reconstruction process which could further speed up the reconstruction process for times series fMRI data.

In Section 3.1, we analyzed and compared three updating methods, static, dynamic, and moving average methods for updating parallel imaging calibration data, as applied to time series fMRI data acquired with a reduced spiral acquisition using TGRAPPA and TSENSE. Human experiments and phantom experiments, with and without intentional induced motion were conducted from which we determined that the best image quality is achieved by applying the dynamic update method of GRAPPA coefficients for TSENSE, whereas the largest number of activated pixels and best TSNR are achieved by applying the static sensitivity maps (no updating) for TSENSE. This conclusion was found to be statistically significant. The findings in this study may be useful for those who are planning to apply dynamic parallel imaging methods to fMRI using spiral imaging.

In Section 3.2, we compared single-shot spiral SENSE and two-shot spiral TSENSE in terms of overall fMRI performance, both without and with UNFOLD filtering. We demonstrated that before processing UNFOLD temporal filtering, the performance of single-shot SENSE excels that of TSENSE whereas they are comparable to each other after UNFOLD. However, for fMRI study, where the temporal resolution is an important factor, applying UNFOLD degrades the temporal resolution, thus might not be desirable for fMRI study. Therefore, we propose to use single-shot spiral, which does not necessary require UNFOLD temporal filtering, when applying parallel imaging in fMRI.

In Section 3.3, we investigated the initialization method using the previous time point on time series fMRI data. Using the image from the previous time point led us to achieve 3-fold acceleration in convergence rate for simulation studies. However, for in-vivo human data, we found a reduced temporal SNR by 1~2dB which is not desirable. This reduction in TSNR is possibly due to the suboptimal condition from using undersampled data and ill-conditioning of system matrix. For future study, we will investigate several other possible initializing methods, such as using low resolution for images from fully sampled data, with a motion tracking or correction algorithm which might give us more robust result for real-time human data. We envision that the improvement on initialization will give more practical solution for people who are trying to do real-time image reconstruction algorithm for non-Cartesian fMRI data.

In Chapter 4, we developed a joint estimation method of image and coil sensitivity map with a quadratic regularization on the estimation of sensitivity map which resulted in much more robust performance compared to non-joint estimation approach when the initial sensitivity map is not accurate. Another contribution using our proposed joint estimation method is that we can use a global, non-object dependent sensitivity pattern which is close enough to the actual sensitivity map to serve as a good initializer for the joint estimation method, thus eliminating the need to acquire the sensitivity map for every scan for every subject. This can add time and inconvenience to imaging studies. For future work, we can refine the global sensitivity map, by specifying the map for each slice or by using physics-based estimation, such as Biot-Savart method, for better global sensitivity map.

Our future research goals are to extend the current dynamic parallel imaging techniques we have developed to higher field and combine it with compressed sensing [93-95] approach. Increased SNR at higher field can effectively outweigh the SNR penalty inherent with parallel imaging, and the increased magnetic field susceptibility effects at higher field can be suppressed by using parallel imaging. Thus, it has become obvious that parallel imaging can become a powerful tool to provide effective solutions for several issues described in using higher field. Furthermore, compressed sensing and parallel imaging are complementary acceleration methods and both approaches can be combined to further improve robustness and acceleration.

References

1. Ogawa S., Lee T. M., Nayak A. S., Glynn P. Oxygenation-sensitive contrast in magnetic resonance image of rodent brain at high magnetic fields. Magnetic Resonance in Medicine 1990;14(1):68-78.
2. Barth M. Functional MRI, Edited by C.T.W. Moonen and P.A. Bandettini, Springer-Verlag, 1999, 575 pp. ISBN 3-540-64263-3. European journal of radiology 2000;36(1):58.
3. Shizhe Li, Bernard J. Dardzinski, Christopher M. Collins, Qing X. Yang, Michael B. Smith. Three-dimensional mapping of the static magnetic field inside the human head. Magnetic Resonance in Medicine 1996;36(5):705-714.
4. Weiger M., Pruessmann K. P., Osterbauer R., Bornert P., Boesiger P., Jezzard P. Sensitivity-encoded single-shot spiral imaging for reduced susceptibility artifacts in BOLD fMRI. Magnetic Resonance in Medicine 2002;48(5):860-866.
5. De Zwart J. A., Van Gelderen P., Golay X., Ikonomidou V. N., Duyn J. H. Accelerated parallel imaging for functional imaging of the human brain. Nmr in Biomedicine 2006;19(3):342-351.
6. Golay Xavier, De Zwart Jacco A., Ho Yi-Ching Lynn, Sitoh Yih-Yian. Parallel imaging techniques in functional MRI. Top Magn Reson Imaging 2004;15(4):255-265.
7. Pruessmann K. P., Weiger M., Scheidegger M. B., Boesiger P. SENSE: Sensitivity encoding for fast MRI. Magnetic Resonance in Medicine 1999;42(5):952-962.
8. Griswold M. A., Jakob P. M., Nittka M., Goldfarb J. W., Haase A. Partially parallel imaging with localized sensitivities (PILS). Magnetic Resonance in Medicine 2000;44(4):602-609.
9. Sodickson D. K., Manning W. J. Simultaneous acquisition of spatial harmonics (SMASH): Fast imaging with radiofrequency coil arrays. Magnetic Resonance in Medicine 1997;38(4):591-603.
10. Jakob P. M., Griswold M. A., Edelman R. R., Sodickson D. K. AUTO-SMASH: a self-calibrating technique for SMASH imaging. SiMultaneous Acquisition of Spatial Harmonics. Magma 1998;7(1):42-54.
11. Heidemann R. M., Griswold M. A., Haase A., Jakob P. M. VD-AUTO-SMASH imaging. Magnetic Resonance in Medicine 2001;45(6):1066-1074.
12. Griswold M. A., Jakob P. M., Heidemann R. M., Nittka M., Jellus V., Wang J. M., Kiefer B., Haase A. Generalized autocalibrating partially parallel acquisitions (GRAPPA). Magnetic Resonance in Medicine 2002;47(6):1202-1210.
13. Kyriakos W. E., Panych L. P., Kacher D. F., Westin C. F., Bao S. M., Mulkern R. V., Jolesz F. A. Sensitivity profiles from an array of coils for encoding and reconstruction in parallel (SPACE RIP). Magnetic Resonance in Medicine 2000;44(2):301-308.
14. Qian Y. X., Zhang Z. H., Stenger V. A., Wang Y. Self-calibrated spiral SENSE. Magnetic Resonance in Medicine 2004;52(3):688-692.
15. Mckenzie C. A., Yeh E. N., Ohliger M. A., Price M. D., Sodickson D. K. Self-calibrating parallel imaging with automatic coil sensitivity extraction. Magnetic Resonance in Medicine 2002;47(3):529-538.
16. Roemer P. B., Edelstein W. A., Hayes C. E., Souza S. P., Mueller O. M. The NMR phased array. Magnetic Resonance in Medicine 1990;16(2):192-225.
17. Bydder M., Larkman D. J., Hajnal J. V. Combination of signals from array coils using image-based estimation of coil sensitivity profiles. Magnetic Resonance in Medicine 2002;47(3):539-548.
18. Walsh D. O., Gmitro A. F., Marcellin M. W. Adaptive reconstruction of phased array MR imagery. Magnetic Resonance in Medicine 2000;43(5):682-690.
19. Sutton B.P., Fessler J.A., Noll D.C. Iterative MR image reconstruction using sensitivity and inhomogeneity field maps. In: Proceedings of the 9th Scientific Meeting of ISMRM, Glasgow 2001:771.
20. Heberlein K., Hu X. P. Auto-calibrated parallel spiral imaging. Magnetic Resonance in Medicine 2006;55(3):619-625.
21. Heidemann R. M., Griswold M. A., Seiberlich N., Kruger G., Kannengiesser S. A. R., Kiefer B., Wiggins G., Wald L. L., Jakob P. M. Direct parallel image reconstructions for spiral trajectories using GRAPPA. Magnetic Resonance in Medicine 2006;56(2):317-326.
22. Pruessmann K. P., Weiger M., Bornert P., Boesiger P. Advances in sensitivity encoding with arbitrary k-space trajectories. Magnetic Resonance in Medicine 2001;46(4):638-651.

23. Noll D. C., Meyer C. H., Pauly J. M., Nishimura D. G., Macovski A. A homogeneity correction method for magnetic resonance imaging with time-varying gradients. IEEE Transactions on Medical Imaging 1991;10(4):629-637.
24. Breuer F. A., Kellman P., Griswold M. A., Jakob P. M. Dynamic autocalibrated parallel imaging using temporal GRAPPA (TGRAPPA). Magnetic Resonance in Medicine 2005;53(4):981-985.
25. Kellman P., Epstein F. H., Mcveigh E. R. Adaptive sensitivity encoding incorporating temporal filtering (TSENSE). Magnetic Resonance in Medicine 2001;45(5):846-852.
26. Madore B., Glover G. H., Pelc N. J. Unaliasing by Fourier-encoding the overlaps using the temporal dimension (UNFOLD), applied to cardiac imaging and fMRI. Magnetic Resonance in Medicine 1999;42(5):813-828.
27. Kellman P., Sorger J. M., Epstein F. H., Mcveigh E. R. Low latency temporal filter design for real-time MRI using UNFOLD. Magnetic Resonance in Medicine 2000;44(6):933-939.
28. Worsley. Functional MRI: An Introduction to methods. eds Jezzard P, Matthews PM, Smith SM (Oxford Univ Press, Oxford) 2001.
29. Bandettini P. A., Jesmanowicz A., Wong E. C., Hyde J. S. Processing strategies for time-course data sets in functional MRI of the human brain. Magnetic Resonance in Medicine 1993;30(2):161-173.
30. Krüeger Gunnar, Glover Gary H. Physiological noise in oxygenation-sensitive magnetic resonance imaging. Magnetic Resonance in Medicine 2001;46(4):631-637.
31. Murphy K., Bodurka J., Bandettini P. A. How long to scan? The relationship between fMRI temporal signal to noise ratio and necessary scan duration. Neuroimage 2007;34(2):565-574.
32. Robson P. M., Grant A. K., Madhuranthakam A. J., Lattanzi R., Sodickson D. K., Mckenzie C. A. Comprehensive quantification of signal-to-noise ratio and g-factor for image-based and k-space-based parallel imaging reconstructions. Magnetic Resonance in Medicine 2008;60(4):895-907.
33. Breuer F. A., Kannengiesser S. A. R., Blaimer M., Seiberlich N., Jakob P. M., Griswold M. A. General formulation for quantitative g-factor calculation in GRAPPA reconstructions. Magnetic Resonance in Medicine 2009;62(3):739-746.
34. De Zwart J. A., Van Gelderen P., Kellman P., Duyn J. H. Reduction of gradient acoustic noise in MRI using SENSE-EPI. Neuroimage 2002;16(4):1151-1155.
35. Moeller S., Van De Moortele P. F., Goerke U., Adriany G., Ugurbil K. Application of parallel imaging to fMRI at 7 Tesla utilizing a high 1D reduction factor. Magnetic Resonance in Medicine 2006;56(1):118-129.
36. Adriany G., Van De Moortele P. F., Wiesinger F., Moeller S., Strupp J. P., Andersen P., Snyder C., Zhang X. L., Chen W., Pruessmann K. P., Boesiger P., Vaughan T., Ugurbil K. Transmit and receive transmission line arrays for 7 tesla parallel imaging. Magnetic Resonance in Medicine 2005;53(2):434-445.
37. Lutcke H., Merboldt K. D., Frahm J. The cost of parallel imaging in functional MRI of the human brain. Magnetic Resonance Imaging 2006;24(1):1-5.
38. Preibisch C., Pilatus U., Bunke R., Hoogenraad F., Zanella F., Lanfermann H. Functional MRI using sensitivity-encoded echo planar imaging (SENSE-EPI). Neuroimage 2003;19(2):412-421.
39. Little Mw, Papdaki A, Mcrobbie Dw. An investigation of GRAPPA in conjunction with fMRI of the occipital cortex at 3 T. In: Proceedings of the 12th Scientific Meeting of ISMRM, Kyoto 2004:1025.
40. Schmidt Cf, Degonda N, Henke K, Boesiger P. Application of SENSE to fMRI studies of higher cognitive functions. . In: Proceedings of the 11th Scientific Meeting of ISMRM, Toronto 2003:737.
41. De Zwart J. A., Van Gelderen P., Kellman P., Duyn J. H. Application of sensitivity-encoded echo-planar imaging for blood oxygen level-dependent functional brain imaging. Magnetic Resonance in Medicine 2002;48(6):1011-1020.
42. Morgan Ps, Kozel Fa, George Ms, Johnson Ka, Baylis Gc, Rorden C., Noll Douglas. Optimal SENSE factor for BOLD fMRI at 3T. In: Proceedings of the 12th Scientific Meeting of ISMRM, Kyoto 2004:1030.
43. Jerde Trenton A., Lewis Scott M., Goerke Ute, Gourtzelidis Pavlos, Tzagarakis Charidimos, Lynch Joshua, Moeller Steen, Moortele Pierre-Franc¸Ois Van De, Adriany Gregor, Trangle Jeran, Ug˘Urbil KaˆMil, Georgopoulos Apostolos P. Ultra-high field parallel imaging of the superior parietal lobule during mental maze solving. Exp Brain Res 2008;187:551–561.
44. Peeters R. R., Vandenbulcke M., Vandenberghe R., Hecke P. Van. Visualizing anterior temporal

activation during semantic processing with parallel imaging techniques. In: Proceedings of the 12th Scientific Meeting of ISMRM, Kyoto 2004:736.
45. Van De Moortele P, Adriany G, Moeller S. Whole brain fMRI in human at ultra-high field with parallel SENSE imaging. In: Proceedings of the 12th Scientific Meeting of ISMRM, Kyoto 2004:1027.
46. Boujraf Said, Summers Paul, Belahsen Faouzi, Prussmann Klaas, Kollias Spyros. Ultrafast bold fMRI using single-shot spin-echo echo planar imaging. J Med Phys 2009;34(1):37-42.
47. Norris D. G. High field human imaging. Journal of Magnetic Resonance Imaging 2003;18(5):519-529.
48. Ugurbil K., Adriany G., Andersen P., Chen W., Garwood M., Gruetter R., Henry P. G., Kim S. G., Lieu H., Tkac I., Vaughan T., Van De Moortele P. F., Yacoub E., Zhu X. H. Ultrahigh field magnetic resonance imaging and spectroscopy. Magnetic Resonance Imaging 2003;21(10):1263-1281.
49. Hu X. P., Norris D. G. Advances in high-field magnetic resonance imaging. Annual Review of Biomedical Engineering 2004;6:157-184.
50. Xu Dan, Ying Leslie, Liang Zhi-Pei. SENSE reconstruction with inaccurate sensitivity functions: effects and remedies. Conf Proc IEEE Eng Med Biol Soc 2004;2:1112-1115.
51. Lee R. F., Giaquinto R. O., Hardy C. J. Coupling and decoupling theory and its application to the MRI phased array. Magnetic Resonance in Medicine 2002;48(1):203-213.
52. De Zwart J. A., Ledden P. J., Kellman P., Van Gelderen P., Duyn J. H. Design of a SENSE-optimized high-sensitivity MRI receive coil for brain imaging. Magnetic Resonance in Medicine 2002;47(6):1218-1227.
53. Ohliger M. A., Sodickson D. K. An introduction to coil array design for parallel MRI. Nmr in Biomedicine 2006;19(3):300-315.
54. Mcdougall M. P., Wright S. M. 64-channel array coil for single echo acquisition magnetic resonance imaging. Magnetic Resonance in Medicine 2005;54(2):386-392.
55. Keeling S. L., Bammer R. Variational based coil sensitivity estimation. In: Proceedings of the 9th Scientific Meeting of ISMRM, Glasgow 2001:800.
56. Lin Fa-Hsuan, Wald Lawrence L., Chen Ying-Jui, Belliveau John W. Estimation of coil sensitivity map and correction of surface coil magnetic resonance images using wavelet decomposition. In: Proceedings of the 9th Scientific Meeting of ISMRM, Glasgow 2001:801.
57. Cao M, Stenger Va, Eddy W. Estimation of images and sensitivities for multi-coil MRI. In: Proceedings of the 13th Scientific Meeting of ISMRM, Miami 2005:2447.
58. Yang Y. H., Gu H., Zhan W., Xu S., Silbersweig D. A., Stern E. Simultaneous perfusion and BOLD imaging using reverse spiral scanning at 3T: Characterization of functional contrast and susceptibility artifacts. Magnetic Resonance in Medicine 2002;48(2):278-289.
59. Noll D. C. Rapid MR image acquisition in the presence of background gradients. 2002 IEEE International Symposium on Biomedical Imaging, Proceedings 2002:725-728.
60. Glover G. H., Law C. S. Spiral-in/out BOLD fMRI for increased SNR and reduced susceptibility artifacts. Magnetic Resonance in Medicine 2001;46(3):515-522.
61. Yeh E. N., Stuber M., Mckenzie C. A., Botnar R. M., Leiner T., Ohliger M. A., Grant A. K., Willig-Onwuachi J. D., Sodickson D. K. Inherently self-calibrating non-cartesian parallel imaging. Magnetic Resonance in Medicine 2005;54(1):1-8.
62. Kim Y. C., Noll D. C., Fessler J. A. Smoothing effect of sensitivity map on fMRI data using a novel regularized self-calibrated estimation method. In: Proceedings of the 16th Scientific Meeting of ISMRM, Toronto, 2008:p1267.
63. Jenkinson M., Bannister P., Brady M., Smith S. Improved optimization for the robust and accurate linear registration and motion correction of brain images. Neuroimage 2002;17(2):825-841.
64. Kim Y. C., Noll D. C., Fessler J. A. Selection of image support region and of an improved regularization for non-Cartesian SENSE. In: Proceedings of the 18th Scientific Meeting of ISMRM, Stockholm, 2010:p2881.
65. Sedarat H., Nishimura D. G. On the optimality of the gridding reconstruction algorithm. IEEE Transactions on Medical Imaging 2000;19(4):306-317.
66. Zwaga J. H., Wajer F. T. A.W., De Beer R. , Fuderer M. , Mehlkopf A. F. , Van Ormondt D. . Improved Kaiser-Besel window parameter selection for gridding. In: Proceedings of the 6th Scientific Meeting of ISMRM, Sydney 1998:669.

67. Plevritis S. K., Macovski A. Spectral extrapolation of spatially bounded images. IEEE Transactions on Medical Imaging 1995;14(3):487-497.
68. Shieh H. M., Byrne C. L. Image reconstruction from limited Fourier data. Journal of the Optical Society of America a-Optics Image Science and Vision 2006;23(11):2732-2736.
69. D'arcy J. A., Collins D. J., Rowland I. J., Padhani A. R., Leach M. O. Applications of sliding window reconstruction with cartesian sampling for dynamic contrast enhanced MRI. Nmr in Biomedicine 2002;15(2):174-183.
70. Kim Y. C., Noll D. C. Functional MRI Using Spiral GRAPPA Parallel Imaging. In: Proceedings of the 13th Scientific Meeting of ISMRM, South Beach, 2005:p1541.
71. Kim Y. C., Noll D. C. Parallel Imaging in Functional MRI: Comparison of Spiral SENSE and GRAPPA and of Calibration Update Schemes. In: Proceedings of the 14th Scientific Meeting of ISMRM, Seattle, 2006:p2817.
72. Noll D. C., Stenger V. A., Vazquez A. L., Peltier S. J. Spiral scanning in fMRI. Functional Mri 2000:149-160.
73. Hu X. P., Kim S. G. Reduction of signal fluctuation in functional MRI using navigator echoes. Magnetic Resonance in Medicine 1994;31(5):495-503.
74. Madore B. Using UNFOLD to remove artifacts in parallel imaging and in partial-Fourier imaging. Magnetic Resonance in Medicine 2002;48(3):493-501.
75. Madore B. UNFOLD-SENSE: A parallel MRI method with self-calibration and artifact suppression. Magnetic Resonance in Medicine 2004;52(2):310-320.
76. Blaimer Martin, Breuer Felix, Mueller Matthias, Heidemann Robin M., Griswold Mark A., Jakob Peter M. SMASH, SENSE, PILS, GRAPPA: how to choose the optimal method. Top Magn Reson Imaging 2004;15(4):223-236.
77. Preibisch C., Wallenhorst T., Heidemann R., Zanella F. E., Lanfermann H. Comparison of parallel acquisition techniques generalized autocalibrating partially parallel acquisitions (GRAPPA) and modified sensitivity encoding (mSENSE) in functional MRI (fMRI) at 3T. Journal of Magnetic Resonance Imaging 2008;27(3):590-598.
78. Glover G. H., Lai S. Self-navigated spiral fMRI: Interleaved versus single-shot. Magnetic Resonance in Medicine 1998;39(3):361-368.
79. Sutton B. P., Noll D. C., Fessler J. A. Fast, iterative image reconstruction for MRI in the presence of field inhomogeneities. IEEE Transactions on Medical Imaging 2003;22(2):178-188.
80. Shewchuk Jonathan. An Introduction to the Conjugate Gradient Method Without the Agonizing Pain: Carnegie Mellon University; 1994.
81. Gabr R. E., Aksit P., Bottomley P. A., Youssef A. B. M., Kadah Y. M. Deconvolution-interpolation gridding (DING): Accurate reconstruction for arbitrary k-space trajectories. Magnetic Resonance in Medicine 2006;56(6):1182-1191.
82. Clinthorne N. H., Pan T. S., Chiao P. C., Rogers W. L., Stamos J. A. Preconditioning methods for improved convergence-rates in iterative reconstructions. IEEE Transactions on Medical Imaging 1993;12(1):78-83.
83. Fessler J. A., Booth S. D. Conjugate-gradient preconditioning methods for shift-variant PET image reconstruction. IEEE Transactions on Image Processing 1999;8(5):688-699.
84. Sutton Bradley P. Physics Based Iterative Reconstruction for MRI: Compensating and Estimating Field Inhomogeneity and T2* Relaxation. PhD thesis University of Michigan, MI, 2003.
85. Eggers H., Boernert P., Boesiger P. Improved Initialization of the Iterative Reconstruction for Sensitivity-Encoded Non-Cartesian Imaging In: Proceedings of the 11th Scientific Meeting of ISMRM, Toronto 2003:15.
86. Qu P., Zhang B., Wang C., Shen G. X. Multi-Resolution Successive Iteration (MRSI) For Non-Cartesian SENSE Reconstruction. In: Proceedings of the 14th Scientific Meeting of ISMRM, Seattle 2006:9.
87. Milles Julien, Zhu Yue Min, Chen Nankuei, Panych Lawrence, Gimenez Gerard, Guttmann Charles R. G., Lemke Heinz U. Computation of transmitted and received B1 fields in magnetic resonance imaging. Computer assisted radiology and surgery 2003:1323.
88. Ballester M. A. G., Machida Y., Kassai Y., Hamamura Y., Sugimoto H. Robust estimation of coil sensitivities for rf subencoding acquisition techniques. In: Proceedings of the 9th Scientific Meeting of ISMRM, Glasgow 2001:799.
89. Liang Z. P., Ying L., Xu D., Yuan L. Parallel imaging: Some signal processing issues and solutions.

2004 2nd IEEE International symposium on biomedical imaging: Macro to nano, vols 1 and 2 2004:1204-1207.
90. Ying L., Sheng J. H., Liu B. Joint estimation of image and coil sensitivities in parallel MRI. 2006 3rd Ieee International Symposium on Biomedical Imaging: Macro to Nano, Vols 1-3 2006:17-20.
91. Ying L., Sheng J. H. Joint image reconstruction and sensitivity estimation in SENSE (JSENSE). Magnetic Resonance in Medicine 2007;57(6):1196-1202.
92. Sheng J. H., Ying L. L., Wiener E., Liu B. Joint estimation of image and coil sensitivities in parallel spiral MRI. 2007 4th Ieee International Symposium on Biomedical Imaging : Macro to Nano, Vols 1-3 2007:133-136.
93. Lustig M., Donoho D., Pauly J. M. Sparse MRI: The application of compressed sensing for rapid MR imaging. Magnetic Resonance in Medicine 2007;58(6):1182-1195.
94. Liang D., Liu B., Wang J. J., Ying L. Accelerating SENSE Using Compressed Sensing. Magnetic Resonance in Medicine 2009;62(6):1574-1584.
95. Lustig M., Pauly J. M. SPIRiT: Iterative Self-consistent Parallel Imaging Reconstruction From Arbitrary k-Space. Magnetic Resonance in Medicine;64(2):457-471.